Spectral Lags and Variability of Gamma-ray Bursts in the Swift Era

by Tilan N. Ukwatta

B.Sc. in Computer Science, January 2002, The University of Colombo, Sri Lanka

M.Phil. in Physics, May 2008, The George Washington University, USA

A Dissertation submitted to

The Faculty of
The Columbian College of Arts and Sciences
of The George Washington University
in partial fulfillment of the requirements for the degree of
Doctor of Philosophy

January 31, 2011

Dissertation directed by

Kalvir S. Dhuga

Associate Professor of Physics

The Columbian College of Arts and Sciences of The George Washington University certifies that Tilan Niranjan Ukwatta has passed the Final Examination for the degree of Doctor of Philosophy as of November 17, 2010. This is the final and approved form of the dissertation.

Spectral Lags and Variability of Gamma-ray Bursts in the Swift Era

Tilan Niranjan Ukwatta

Dissertation Research Committee:

Kalvir S. Dhuga, Associate Professor of Physics, Dissertation Director

Ali Eskandarian, Associate Professor of Physics, Committee Member

William J. Briscoe, Professor of Physics, Committee Member

Dedicated to Nilmini, the force behind me.

Acknowledgments

Completion of this thesis was possible due to valuable help from many people. Firstly, I would like to thank my thesis supervisor, Professor Kalvir S. Dhuga, for all of the advice, optimism, guidance and for the countless Sundays spent with me working on papers, proposals and on the thesis. I am also grateful for the freedom he has given me to pursue my ideas.

Secondly, I would like to thank my NASA supervisor, Dr. Neil Gehrels, for his continued support during my thesis work. Without his support and guidance this thesis and accompanied publications would not have been possible.

I would also like to thank Dr. Taka Sakamoto and Dr. Mike Stamatikos, who effectively became my associate supervisors for most of my projects, providing critical constructive comments that shaped the analysis.

I would also like to thank the members of GW Astro group: Professor William Parke, Professor Leonard Maximon, Professor Ali Eskandarian, Dr. David Morris, Dr. Glen MacLachlan, Professor Denis Cioffi, and Ashwin Panchmal for providing me with a platform to present and evaluate my ideas. Weekly discussions on various topics at the GW Astro group stimulated most of the analysis methods used in this thesis. A special thanks goes to Professor Leonard Maximon for carefully reading the thesis manuscript and correcting numerous errors in it.

I'd also like to thank the $Swift$ team, especially the BAT team, for building a magnificent instrument which reshaped our understanding of GRBs. I also thank Dr. Scott Barthelmy, Dr. Craig Markwardt, Dr. Jay Norris, and the late Dr. David Band for very useful discussions on the analysis methods used in this thesis. I would also like to thank the people who have collaborated with me on various projects contained in this thesis.

I am indebted to my former adviser the late Professor Barry Berman, who introduced me to research and helped me to acquire the necessary skills to be effective in research. I would also like to thank Professor Frank X. Lee for sending me a life altering email when many other universities have turned me down because of not having a 'proper' physics

background.

I would like to thank my parents and two sisters for encouraging and supporting me to pursue my childhood dream of becoming an astrophysicist. Finally, I would like to thank my wife Nilmini, who was the superhuman force behind me, encouraging me when I was down, taking care of me when I was sick, and provided unwavering support to complete this thesis.

Tilan N. Ukwatta

Abstract of Dissertation

Spectral Lags and Variability of Gamma-ray Bursts in the Swift Era

Gamma-ray bursts (GRBs) are thought to be the most concentrated and brightest explosions in the universe, making them observable to very great distances. Hence GRBs can be used to probe the early universe, including the re-ionization period as well as the intergalactic medium. GRBs may also be used to study the biggest mystery of our time: 'Dark Energy'. However, unlike Supernove 1a, GRBs as yet are not good standard candles. Hence, in order to use GRBs to connect luminosity and distance, we need GRB Luminosity Relations. Over the years people have proposed a number of GRB luminosity relations. Unfortunately, none of them are tight enough to be used individually to construct the GRB Hubble Diagram. However, by combining multiple GRB luminosity relations we can construct a GRB Hubble diagram that may be able to constrain cosmological parameters. Thus, it is important to study and improve existing GRB luminosity relations and perhaps discover new GRB luminosity relations. In addition to helping to improve our understanding of Dark Energy, these GRB luminosity relations are very useful to understand the underlying physics of GRBs.

One major limiting factor in GRB luminosity relation studies is the low statistics. Before the $Swift$ mission there were very few GRBs with measured redshifts. But now in the $Swift$ era we have more than 150 GRBs with measured redshifts. In this work we have utilized this high-quality data set to study two GRB luminosity relations.

In Part-I we extracted spectral lags and studied the lag-luminosity relation. The spectral lag is the time difference between the arrival of high-energy and low-energy photons. To quantify this lag we have developed an improved method based upon the cross correlation function. With this method we investigated the lag-luminosity relation over the entire Swift Burst Alert Telescope (BAT) energy range. Typically, a spectral lag is extracted in two arbitrary energy bands in the observer-frame. However, because of the redshift dependance of GRBs, the two energy bands can correspond to multiple energy bands in the source-frame. Thus, introducing a variable energy dependant factor into the lag-luminosity relation. We

avoid this difficulty by defining two energy bands in the GRB source-frame and projecting these two bands into the observer-frame and extracting lags between them. This work has led to a significant improvement in the robustness of the lag-luminosity relation.

In Part-II we studied the variability of GRBs using Fourier analysis and introduce a new GRB luminosity relation. We extract a maximum frequency at which there is still significant signal power and associate this threshold frequency with the isotropic luminosity of the burst. As a result of this study, we propose a potential correlation between isotropic peak luminosity and the extracted threshold frequency. In this investigation, we study in detail the potential observational biases in the frequency-luminosity relation.

In Part-III we investigate long-term correlations and variability in GRB prompt emission light curves using the Hurst rescaled range analysis technique. As far as we know this is the first time this technique has been applied to GRBs. Based on this analysis, we present evidence indicating that the prompt emission of GRB light curves show anti-persistence.

Contents

Chapter 1

Introduction

Gamma-ray bursts (GRBs) are the most luminous phenomena known in the universe. GRBs occur at apparently random positions in the sky, a few per day. They consist of flashes of gamma rays that last from seconds to hours, and may be followed by several days of X-ray, ultra violet, optical, infrared or radio afterglow. These afterglows in turn enable the measurement of red-shifts and the identification of host galaxies. Thanks to the afterglow detections, it is now known that most GRBs are at cosmological distances of the order of billions of light years, similar to those of the most distant galaxies and quasars. Even at these distances they appear so bright that their energy output is of the order of $10^{47} - 10^{55}$erg/s (assuming isotropic emission), larger than any other type of luminous source [1]. It is comparable to burning up the entire mass-energy of the sun in a few tens of seconds, or to emit over that same period of time as much energy as our entire Milky Way does in a hundred years.

In the last two decades, due to space based instruments such as the Burst and Transient Source Experiment (BATSE) on the Compton Gamma Ray Observatory, BeppoSAX, HETE-2, *Swift* and *Fermi*, considerable progress has been made in the GRB studies. However, we are far from understanding the whole story behind GRBs. In general the goal of GRB studies is to understand the nature of GRB progenitors, their central engine, energy dissipation mechanisms, radiation mechanism, and their environments. Since GRBs can be seen from very far away they have the potential to be useful for cosmological studies as well.

After the initial serendipitous discovery in late 60's until late 90's GRBs were observed

---

[1]It has been found that merging super-massive black-holes produce more energy, but the energy released is dominated by and carried by gravitational waves, which at present are not easily detectable.

mostly in gamma-rays[2]. This initial gamma-ray emission time profile or the light curve tells us a lot about the GRBs. For example, its rapid variability indicates that it is a compact source. More information about the central engine of GRBs is embedded in its prompt emission gamma-ray light curve. We have analyzed the prompt emission of $Swift$ GRB light curves using a variety of techniques to decode some of this hidden information.

Launched in November 2004, the $Swift$ satellite opened a new era in GRB studies. Due to $Swift$'s unprecedented quick slewing capability, rapid followup observation became routine and it enabled redshift measurement of a relatively large number of GRBs. This large GRB sample with known redshifts opened up a new possibility to correct various observed parameters for cosmological effects and to perform meaningful statistical studies on intrinsic GRB properties.

During this thesis work, we have analyzed a sample of 451 GRBs which triggered $Swift$ BAT (Burst Alert Telescope) from 2004 December 19 to 2009 December 31. Out of these 451 GRBs, there are 151 GRBs with known redshift (spectroscopic or otherwise). We have extracted spectral variation parameters such as spectral lags and various variability indicators and corrected for cosmological effects.

- In the second chapter, we will discuss various observations of GRBs. We discuss briefly observational properties of GRB prompt emission and its afterglows, GRB classifications, and properties of their host galaxies. In the second chapter we also introduce the GRB Hubble diagram and GRB luminosity relations.

- In the third chapter, we present a discussion about possible physical interpretations of GRBs, namely, energy dissipation mechanisms, interaction with the interstellar medium, emission mechanisms, and GRB progenitor models.

- In the fourth chapter, we describe the $Swift$ satellite, including its instruments, observation strategy and data reduction.

- The fifth chapter describes the methods for extracting spectral lags and illustrates the cross correlation function (CCF) method with a case study. We also investigate the lag-luminosity relation both in the observer-frame and in the source-frame in this chapter.

---

[2]X-ray observations of prompt GRBs have been accomplished in 1970s for very few cases.

- In the sixth chapter, we extract the Fourier power spectra of GRBs and introduce a potentially new GRB luminosity relation. In this chapter we discuss in detail potential observational biases that effect the relation.

- In chapter seven, we investigate long term correlations in GRB prompt emission light curve via Hurst rescaled range analysis. In this chapter, we present evidence indicating that GRBs are anti-persistent during the prompt emission phase.

- In chapter eight, we discuss implications of analysis in terms of understanding the underlying physics of GRBs.

- Finally, in chapter nine, we summarize our results and conclusions.

Chapter 2

GRB Observations

2.1   Historical Background

The first gamma-ray burst was detected on July, 2nd of 1967 by the US Vela military satellites, which were built to monitor nuclear explosions. When these gamma-ray flashes were first detected it was found that they did not come from the direction of the earth. GRB 670702[1], the first detected GRB, showed two peaks (see Figure 2.1) in burst activity over a period of seconds. The first peak lasted for about an eighth of a second and the second one lasted for about four seconds. This discovery, however, was not published until 1973 (Klebesadel et al., 1973).
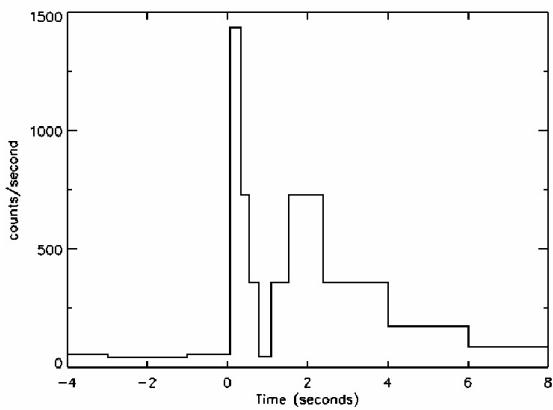
Figure 2.1 The light curve of GRB 670702.

---

[1]GRBs are designated by the date of their detection. For example, GRB 670702 is the burst that has been detected on July 02, 1967.

Vela satellites detected about 70 GRBs over about 10 years. During the period 1973 to 1991 other space based instruments also contributed to increase the GRB sample size. Even with this limited sample, GRB showed an isotropic distribution in the sky. With these early instruments it was not possible to localize GRBs in the sky to do effective followup observations.

In 1991 NASA launched the Compton Gamma-Ray Observatory (CGRO). Onboard CGRO there was an instrument called BATSE (Burst And Transient Source Experiment) which was specially designed to detect GRBs. BATSE detected about 2700 GRBs and confirmed that the sky distribution of GRBs is completely isotropic. It also showed by the deficit of faint bursts that GRBs are not distributed homogeneously in the radial direction. In addition, BATSE confirmed the main properties of GRBs such as duration, lack of standard light curve shape, high temporal variability, absence of periodicities, existence of two populations, and non-thermal energy spectra with a well–defined peak energy. However, BATSE could not answer the question, How far away were these GRBs?

The answer to the question of GRB distance came in 1997 thanks to the Italian-Dutch mission BeppoSAX. Launched in 1996, BeppoSAX had the capability to detect and localize GRBs and perform deep X-ray observations within hours after the burst. This made it possible to detect the first X-ray afterglow for GRB 970228 (Costa et al., 1997). Also for the same burst the first optical afterglow detection was made (van Paradijs et al., 1997). The first radio afterglow was detected for another burst (GRB 970508) that happened during the same year (Frail et al., 1997). GRB 970508 had a particularly bright optical afterglow, which enabled the measurement of its spectrum. The spectrum showed a few absorption lines. Using them, for the first time, the redshift of a GRB was measured with a value of about $z = 0.8$. After about three decades of GRB studies the distance question was answered. Subsequently, many redshift measurements were made and these measurements confirmed that most GRBs are at cosmological distances. The discovery of afterglows across the electromagnetic spectrum from optical to radio revolutionized the GRB research. Quick and precise localization of bursts led to measurement of redshifts either using burst optical afterglows or sometimes using the associated host galaxies. This firmly established that most GRBs are at cosmological distances and are the largest electromagnetic explosions since the Big-Bang.

2.2 GRB Prompt Emission

2.2.1 GRB Light Curves

Prompt gamma-ray emission of GRBs have rapidly varying emissions in their light curves. They also vary drastically from one burst to another as can be seen in Figure 2.2. Figure 2.2 shows a few GRB light curves detected by the $Swift$ satellite and illustrates their diversity in shape and duration. Some GRBs show a single peak which is characterized by a Fast Rise and Exponential Decay (FRED) pulse profile (e.g. GRB 051111 in Figure 2.2). Some other GRBs show multi-peak overlapping structures that are difficult to describe by simple functions. A few GRBs show precursors (e.g. GRB 061121 in Figure 2.2) which precede the main GRB emission. GRB duration can also vary from a few milliseconds to several thousand seconds.

2.2.2 GRB Energy Spectrum

The observed energy spectrum of GRBs is non-thermal. Figure 2.3 shows a schematic diagram of a canonical GRB spectrum. It is composed of two components: 1) A Band Spectral Component (Band et al., 1993) and 2) A Hard Power-law component[2]. In general, the Band function gives a good fit for the low-energy part of the spectrum, so it is customary to use the Band function to fit GRB spectra (Kaneko et al., 2006). The Band function is an empirical spectral function described as follows (Band et al., 1993):

$$
dN/dE = \begin{cases} A(\frac{E}{100\,\text{kev}})^{\alpha}\, e^{-(2+\alpha)E/E_{\text{peak}}},\ E \leq \left(\frac{\alpha-\beta}{2+\alpha}\right)E_{\text{peak}} \\ A(\frac{E}{100\,\text{kev}})^{\beta}\, [\frac{(\alpha-\beta)E_{\text{peak}}}{(2+\alpha)100\,\text{keV}}]^{\alpha-\beta}\, e^{(\beta-\alpha)},\ \text{otherwise} \end{cases} \tag{2.1}
$$

There are four parameters in the Band function, which gives the amplitude (A), the low-energy spectral index (α), the high-energy spectral index (β) and the peak of the νF_ν spectrum, E_{peak}. Note that there is no particular theoretical model that predicts the spectral shape given by the Band function.

The Band function is very good at describing BATSE burst spectra. However, it is difficult to fit $Swift$ burst spectra with the Band function. The reason is that the energy range of $Swift$ BAT is so narrow that in most of the cases it is difficult to sufficiently constrain the E_{peak} (Sakamoto et al., 2009). Hence in order to get Band spectral fit parameters for

---

[2]Note that this spectral component has been seen only by the $Fermi$ satellite thus far.
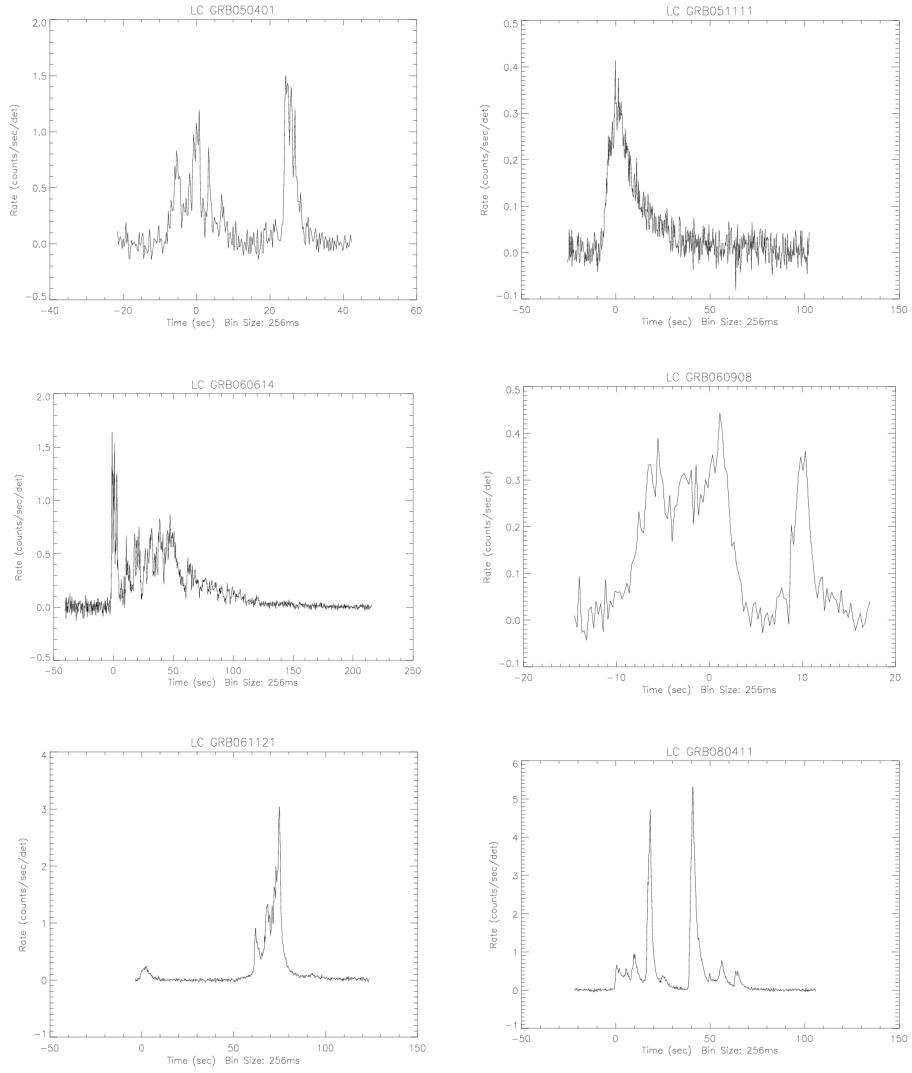
Figure 2.2 GRB light curves show a wide verity of shapes and durations.
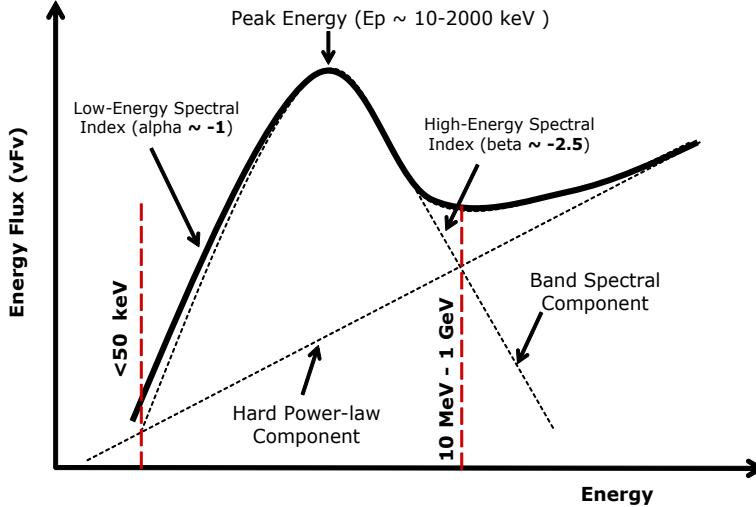
Figure 2.3 Canonical GRB Spectrum. GRB spectrum consist of two components: 1) Band Spectral Component and 2) Hard Power-law component.

some of the $Swift$ detected bursts one has to combine data from other instruments such as Suzaku, Konus Wind and $Fermi$ GBM (Krimm et al., 2009b). This can only be done when a particular burst is observed by two or more instruments simultaneously.

The second spectral component, the hard power-law component, has been seen only for a few GRBs that were detected by $Fermi$ (Granot et al., 2010). However, these GRBs are particularly bright in $Fermi$'s LAT (Large Area Telescope), indicating that this high energy spectral component is probably more common but is not bright enough for clear significant detection (Granot et al., 2010).

2.2.3 Types of GRBs and Possible Prognitors

Based on BATSE observations, GRBs are divided into two classes based on their distribution as shown in Fig 2.4 (Kouveliotou et al., 1993). One type is called long GRBs, which typically have initial durations of T90 > 2 s, and the other type is called short GRBs, which have durations of T90 < 2 s (where T90 is the duration in which 90 % of the fluence[3] is detected). Figure 2.5 shows the T90 distribution of 451 $Swift$ detected GRBs. Unlike for the BATSE GRB sample, $Swift$ detected GRBs do not show two prominent peaks. The detection of fewer short bursts by $Swift$ is due to its triggering mechanism, which is less sensitive to

---

[3]The fluence is the flux received from the GRB integrated over the duration of the burst.

short duration bursts.

The exact nature of the GRB progenitors is unknown, although some models suggests that long GRBs, which on average have softer gamma ray spectra (i.e. higher flux at low energies), come from the deaths of massive, rapidly rotating stars (Woosley and Heger, 2006; Woosley and Bloom, 2006) and short GRBs result from the merger of compact objects such as neutron stars or black holes (Eichler et al., 1989; Narayan et al., 1992).

The association of long bursts to the collapse of massive stars and short bursts to the merger of compact objects, is not a robust classification. There are instances in which bursts show overlapping characteristics (Gehrels et al., 2006). Hence, duration and hardness are not necessarily reliable indicators of the physical nature of GRBs. In order to determine the physical origin of a given GRB, one is forced to use multiple observational criteria (Donaghy et al., 2006). This prompted a number of authors to classify bursts that are consistent with massive-star origin as Type II bursts and those consistent with the merger of compact objects as Type I bursts (Zhang et al., 2009). However, unlike the short/long classification scheme, currently it is very difficult to do a Type I/II classification based only on GRB prompt emission data.
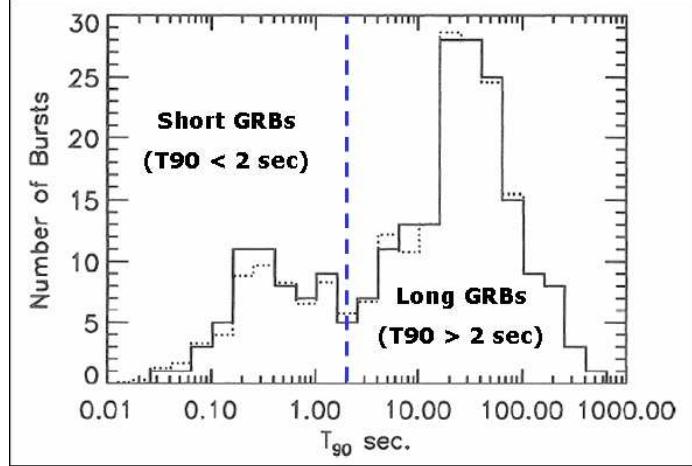
Figure 2.4 The T90 duration distribution of 222 bursts observed by BATSE (The Burst And Transient Source Experiment) (Kouveliotou et al., 1993).

In general, the GRB community uses long/short classification as a 'working classification scheme' due to its straightforward definition based on the prompt light curve duration.
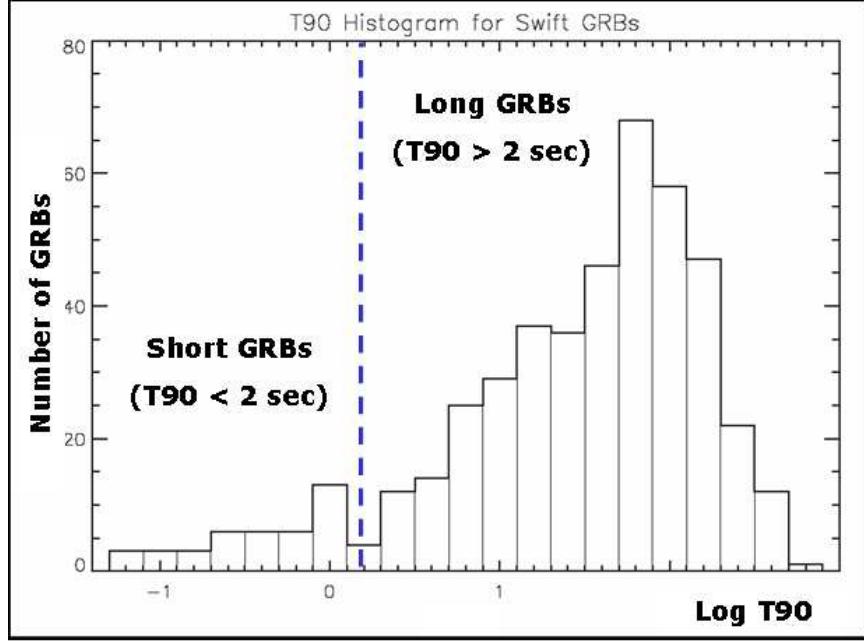
Figure 2.5 The T90 duration distribution of 451 bursts observed by $Swift$.

2.2.4 Long Gamma Ray Bursts

Long gamma ray bursts are the easiest to detect and have been studied extensively. Typically bursts lasting more than 2 seconds fall into this category[4]. Long gamma ray bursts are generally associated with galaxies that have a high rate of star formation and probably arise from the collapsing core of massive stars, which produce highly relativistic jets (collapsar model; see chapter 3 for more details). There are speculations that progenitors of these stars might relate to early Population III[5] stars (i.e. with very low metallicity).

It has been observed that some long GRBs accompany supernovae (Woosley and Bloom, 2006). The inferred all-sky supernova rate is $\sim 6\ s^{-1}$ (Madau et al., 1998) and the universal GRB rate is $\sim 0.02\ \mathrm{s}^{-1}$. Hence, supernovae are roughly 300 times more common than GRBs, implying that GRB progenitors represent a subset of all supernova progenitors (Woosley and Bloom, 2006). This of course does not take into account possible jet beaming effects in GRBs (Frail and al, 2001).

Due to the very high energy output of GRBs; a few orders of magnitude higher than standard candles, supernovae type 1a, a number of studies have explored the possibility of

---

[4]There are short burst with extended emission, which complicates this classification.

[5]The first generation of stars

using long GRBs as cosmological probes. We will discuss this topic further in subsequent sections.

2.2.5 Short Gamma Ray Bursts

Short GRBs tend to emit a larger fraction of their energy as high energy photons (energies above ~ 100 keV) i.e., they have harder spectra than long GRBs. The detection of afterglows from short GRBs in 2005 revolutionized our understanding of these short duration bursts. These studies have shown that most of the short GRBs are cosmological i.e., the same as the long GRBs, and can occur in star forming regions as well as in elliptical galaxies, and unlike long bursts are not associated with supernovae; they also have a wide isotropic equivalent energy ranging from $\sim 10^{48} - 10^{52}$ erg.

In stark contrast to long bursts, the evidence to date on short bursts is that they originate typically from regions which have a low star-formation rate. This supports the interpretation that short bursts are associated with an old stellar population and may arise from mergers of compact binaries such as double neutron stars (NS-NS) or a neutron star and back hole binary (NS-BH).

There have also been suggestions that some fraction of the short GRBs can be exploding primordial black holes (PBH) in the solar neighborhood. We still don't have any concrete evidence to support this suggestion, but some studies have put an upper limit to the abundance of this type of events (Cline et al., 2007). Ukwatta et al. (2009b) have proposed using the spectral lag as another way of detecting PBH evaporation events.

2.3 GRB Afterglows

2.3.1 X-ray Afterglows and the Canonical GRB Light Curve

In Figure 2.6, we show a canonical GRB light curve showing major features of the prompt gamma-ray light curves and X-ray afterglow light curves. It should be noted that not every burst exhibits all of these features. In the case of long GRBs, the prompt hard x-ray (soft gamma-ray) emission smoothly changes into a decaying afterglow. It is found that this is also true for some fraction of short GRBs (Gehrels et al., 2005; Fox et al., 2005).

The X-ray afterglow starts with a steep-decay phase with a decay slope of ~ 3. The early steep-decay phase is normally followed by a shallow-decay phase that begins within

11

the first hour. The shallow phase can last for up to a day, and, although faint, is a significant fraction of the total energy. Both of these phases were discovered by $Swift$ due to its fast slewing capability. A steep-to-shallow transition (steep-decay phase to shallow-decay phase in Figure 2.6) in the GRB light curve suggests that prompt emission and the afterglow are distinct emission components.
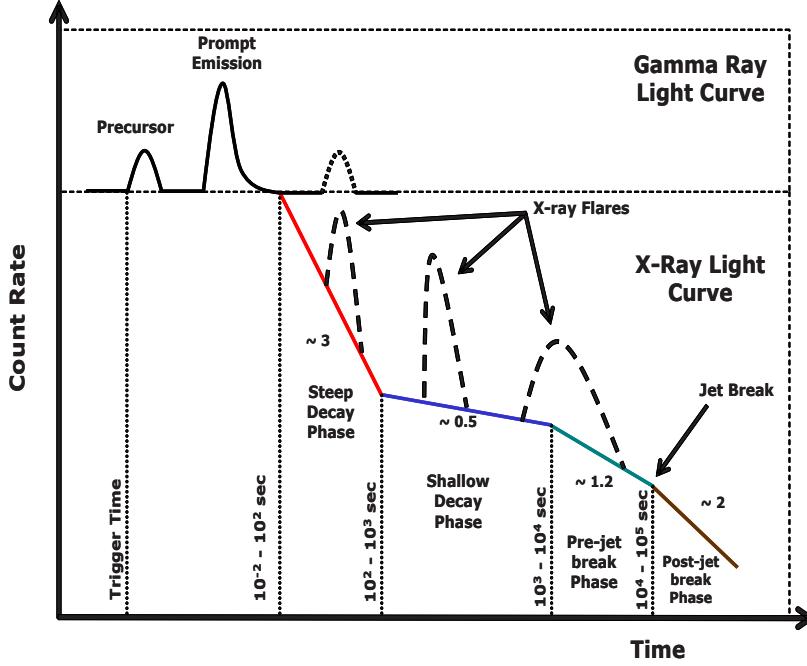
Figure 2.6 Canonical GRB light curve. The prompt phase is often followed by a steep decay phase (typical index of 3) which can then break to a shallower decline (shallow-decay phase), a standard afterglow phase (pre-jet break phase), and possibly, a jet break and post-jet break phase. Sometimes an X-ray flare is seen.

After the shallow-decay phase the light curve is divided into two phases (pre-jet-break phase and post-jet-break phase) if there is a jet break. Jet breaks are thought to happen due to the beaming of the emission from GRBs. These jet breaks are achromatic. That means jet break should be observed in all wavelengths (x-ray, optical and radio). Possible jet breaks have been measured in some earlier bursts, but $Swift$ afterglow measurements provide little evidence for achromatic jet breaks (Willingale et al., 2007; Sato et al., 2007).

Swift has found another interesting flaring behavior in the X-ray light curve lasting long after the prompt phase, in some cases several hours after the burst. X-ray flares can occur anywhere in the X-ray afterglow light curve. The most extreme examples include flares with integrated power comparable to that of the initial burst (Burrows et al., 2005b).

12

A few examples of actual X-ray afterglow light-curve profiles are shown in Figure 2.7.
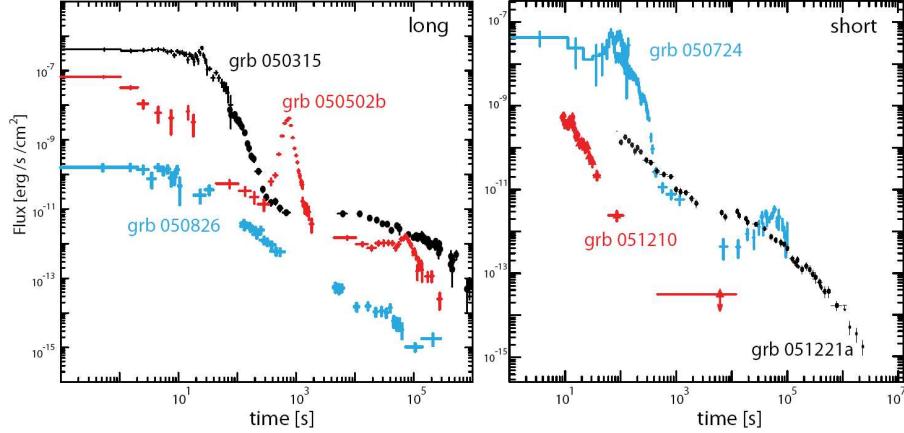
Figure 2.7 Example GRBs X-ray afterglow light curves for both long and short bursts from Gehrels et al. (2009) with steep-to-shallow transition (GRB 050315, GRB 050724), large x-ray flare (GRB 050502B, GRB 050724), fast declining (GRB 051210) and more gradually declining afterglow(GRB 051221A, GRB050826).

2.3.2 Optical Afterglow

Detection of optical afterglows of GRBs are less frequent compared to X-ray afterglows (Roming et al., 2009). Typically optical afterglows are seen in $\sim 50\%$ of GRBs. GRBs with no visible optical afterglow are called Dark GRBs. These dark bursts have relatively bright X-ray afterglows, but no observable optical afterglows.

2.3.3 Radio Afterglow

Radio afterglow observations of GRBs have provided further direct and indirect evidence of the relativistic expansion of the GRB blastwave through radio scintillation studies and Very Long Baseline Interferometry (VLBI) observations (Frail et al., 2003). Radio afterglow observations are also invaluable in accurately estimating blastwave kinetic energies. Radio afterglow observations also provide an important check on the claims of achromatic jet break detections.

2.3.4   X-ray Flashes (XRFs)

X-ray flashes (XRFs) and X-ray Rich gamma-ray bursts (XRRs) represents two new classes of soft GRBs, which emit the bulk of their radiation in the X-ray region (< 10 keV) of the spectrum (Sakamoto et al., 2005). Other than the softness of their spectrum, XRFs and XRRs show generally the same basic properties as the classical GRBs with some subtle differences (Sakamoto et al., 2008b).

2.4   GRB Redshift Distribution

Optical afterglows allowed us to carry out spectroscopic analysis, from which distances can be determined. Figure 2.8 shows the redshift distribution of a sample of 115 $Swift$ long bursts where the redshifts were measured by observing the spectrum of the optical afterglow. Redshifts of short GRBs are normally measured from the spectrum of their host galaxies. So far no spectroscopic redshift measurement of a short burst have been done using optical afterglow. Short GRBs that have redshift measurements have redshifts which concentrate around $z = 0.2$, although some may possibly lie as far as $z = 2$. The redshifts for short bursts are smaller on average by a factor of ~ 4 than those of long bursts.
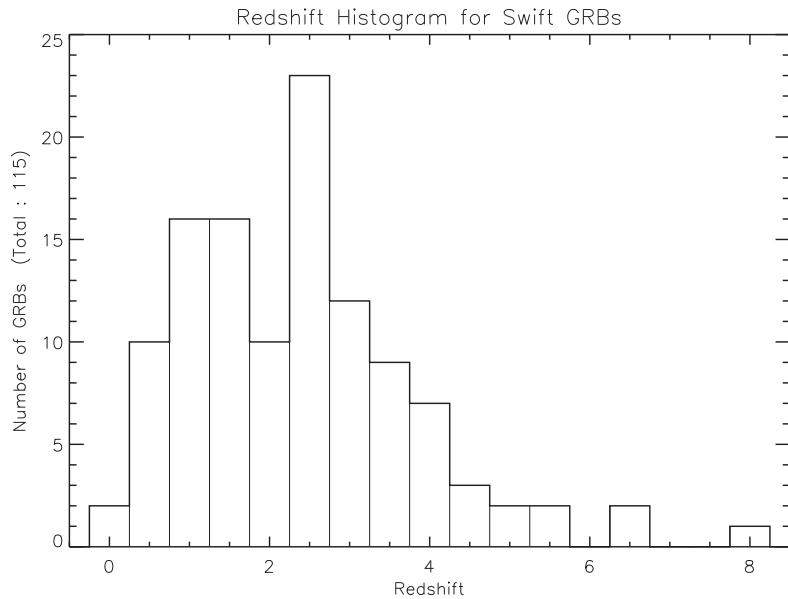
Figure 2.8 Redshift (z) distribution of 115 (spectroscopically confirmed) Swift detected long GRBs.

2.5 GRB Hosts

The issue of progenitors of both long and short GRBs is not yet settled. We can make some inferences about GRB progenitors by studying their Host galaxies. In the following two section we will discuss properties of host galaxies of both long and short bursts.

2.5.1 Host Galaxies of Long GRBs

After the discovery of long wavelength counterparts, more precise position information made it possible to study the host galaxies of GRBs. Careful afterglow and host galaxy observations have shown that long GRBs lie in star forming galaxies (Bloom et al., 1998; Djorgovski et al., 1998; Fruchter et al., 1999; Bloom et al., 2002; Conselice et al., 2005; Fruchter et al., 2006; Wainwright et al., 2007). We summarize below results from the host galaxy studies of long bursts (Gehrels et al., 2009).

- Long GRB host galaxies are sub-L^* (median $L \sim 0.1L^*$) with high star formation rates. Here L^* is the luminosity of Milky way.

- There is some evidence to indicate that long GRB projenitors prefer low-metalicity environment in galaxies.

- Long burst locations are strongly correlated with rest-frame ultraviolet light (young massive stars) of their host galaxies.
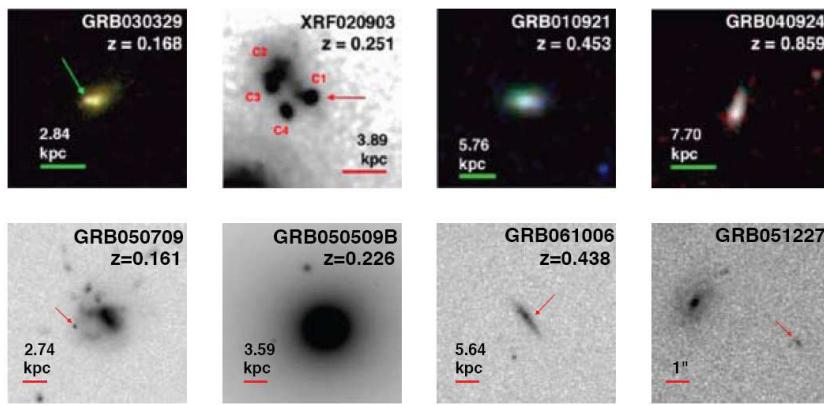
Figure 2.9 Host galaxies of long duration (top row) and short duration (bottom row) GRBs (Gehrels et al., 2009).

2.5.2 Host Galaxies of Short GRBs

After the detection of afterglows from short GRBs in 2005, considerable progress has been made. Berger (2010) has summarized current results of the short burst host galaxy studies as follows.

- Few short GRBs are associated with elliptical galaxies while the majority of short GRBs occur in star forming galaxies.

- The star forming hosts of short GRBs are distinct from those of long GRBs. Short burst hosts have lower star formation rates, and higher luminosities and metallicities compared to long burst hosts.

- The physical offsets of short bursts relative to their host galaxy centers are significantly larger compared with long GRBs. The observed offset distribution is consistent with that predicted using NS-NS models.

- Short bursts trace under-luminous locations within their hosts. Unlike long bursts they appear to be more closely correlated with the rest-frame optical light (old stars) than the ultraviolet light (young massive stars).

These results indicate that short bursts occur in old stellar populations which have wide age distributions. They also track stellar mass rather than the star formation activity. These results are consistent with what one would expect from NS-NS or NS-BH mergers. However, it is also worth noting that these results were obtained using relatively small sample sizes compared with long bursts. Figure 2.9 shows few representative examples of host galaxies of both long and short bursts.

2.6 High Redshift GRBs and Cosmology

2.6.1 GRB as High Redshift Probes

The universe and our Galaxy are optically thin to low-energy gamma-rays. Hence, GRBs give us a unique cosmological population that can be observed practically uniformly in the sky up to very high redshifts. Most of the observed GRBs have redshifts greater than one (see Figure 2.8). Until recently, GRBs held the record for the farthest away spectroscopically confirmed object ever seen, with a redshift of $\sim$8.27 for GRB 090423 (Tanvir et al., 2009;

Salvaterra et al., 2009). However, the current record holder is a galaxy at a redshift of 8.6 that has been discovered recently (Lehnert et al., 2010).

High-z GRBs also have the potential to trace the star formation rate and metallicity histories of the universe (Lamb and Reichart, 2000). GRBs are 100-1000 times brighter at early times than are high red-shift quasars. Moreover, GRBs are expected to occur out to $z > 10$, whereas the distribution of quasars drops significantly beyond z=3. Another benefit of GRBs is that due to the relatively clean neighborhoods of GRB progenitors, GRB afterglows have simple power-law spectra with no emission lines. Thus GRBs are clean probes of the intergalactic medium (IGM), whereas quasars are contaminated by continuous material emission from the central engine to the quasar's neighborhood. High-z GRB studies will enable us to probe the IGM less than 1 Gyr after the Big Bang. In this respect GRBs provide a unique method to study the early universe.

Another intriguing aspect of GRBs is the potential connection to population III stars. These very early stars have not been detected thus far. One of the expected properties of these stars is low metalicity. Moreover, their distribution is expected to peak at high-z. Detection of a GRB from the collapse of a massive population III star would provide evidence for the existence of such stars.

In addition, high-z GRBs offer the potential to probe the early universe into the epoch of re-ionization. In Big Bang cosmology, re-ionization is the process that reionized the matter in the universe after the dark ages. Re-ionization occurred once objects started to form in the early universe. As these objects formed and radiated energy (initiating the ionization of neutral hydrogen), the universe went from having ordinary matter largely neutral to being largely an ionized plasma, at a redshift $6 < z < 20$. This corresponds to about 150 million to one billion years after the Big Bang (Lamb and Reichart, 2000).

2.6.2 GRB Hubble Diagram

Observational cosmology is another field where potentially GRBs can play a major role in determining the geometry of the Universe. There have been some attempts to use GRBs to set new constraints on cosmological parameters Ω_M and Ω_Λ (Schaefer, 2007). Here Ω_M and Ω_Λ are the present density parameters of the matter and Dark Energy (DE) components of the Universe respectively.

Measurement of the Hubble diagram of Type 1a supernovae revolutionized the field of

cosmology by revealing that the expansion of the Universe is accelerating (Riess et al., 1998; Perlmutter et al., 1999). This acceleration is caused by the presence of a hitherto unknown component of the Universe called Dark Energy.

The Hubble diagram is a plot showing the distance moduli (measure of distance) as a function of redshift as shown in Figure 2.10. The slope of the plot gives us information about the expansion history of our Universe by constraining the behavior of cosmological parameters (Ω_M and Ω_Λ).

The simplest model for the behavior of dark energy is that it is a constant and does not change with time. Generally the dark energy is parameterized with the equation of state $p = w\rho c^2$, where p is the pressure, ρ is the density and c is the speed of light. Here w is a dimensionless constant that may change with time. In concordance the cosmological model, $w = -1$ at all times. However, other models have been proposed, such as 'Weyl Gravity' (Mannheim, 2006), 'Chaplygin Gas' (Kamenshchik et al., 2001) and Riess cosmology where $w = -1.31 \pm 1.48z$ (Riess et al., 2004). Predictions from these models cannot be easily distinguished by looking at lower redshifts of the Hubble diagram. However, at higher redshifts these models are easily distinguishable (see Figure 2.10). Hence, potentially accurate GRB Hubble diagrams extending to redshifts of ~ 8 can easily constrain these models.

Early attempts to employ GRBs as a cosmological tool, i.e., as a standard candle to get distances, relied on the use of the isotropic equivalent energy (E_{iso}). However, this soon ran into problems. The quantities involved in the expression for E_{iso} (i.e., the burst bolometric fluence, the red-shift and the distance) are in principle all measurable. Unfortunately, it turns out that a compilation of E_{iso} for a sample of bursts spans several orders of magnitude (presumably due to the beaming of the jet), practically negating its value as a standard candle, unless further distinguishing characteristics of GRBs can be found[6]. However, the discovery of Cepheid like relations between observationally measurable parameters and GRB energetics kept the GRBs alive in the study of cosmological parameters. These relations are called GRB Luminosity Relations.

---

[6]As a comparison we note that Type 1a supernovae have a RMS scatter of only ~ 0.0075 decades.
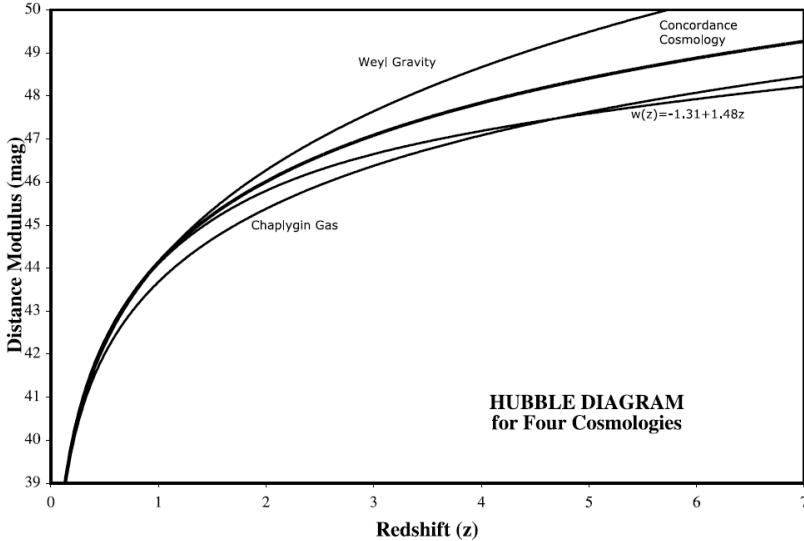
Figure 2.10 Hubble Duagram for a reporesentative set of cosmological models (Schaefer, 2007). Here the distance modulus (μ) is defined as $\mu = 5 \log d_L - 5$, where d_L is the luminosity distance.

2.6.3 GRB Luminosity Relations

The GRB luminosity relation is a relation between some observationally measurable timing or spectral parameter of GRBs and their energy or luminosity. Based on BATSE GRB data, a number of such relations between various observables have been found (see Appendix A). For example, using bursts with known red-shifts, Amati et al. (2002) discovered a simple relation that indicates a direct proportionality between the peak energy (E_{peak}) and the square root of the isotropic-equivalent energy (E_{iso}). Yonetoku et al. (2004) discovered a very similar relation involving peak energy and the isotropic luminosity at the source frame of the GRB. Recent work (Butler et al., 2007) however casts doubt on the validity of these relations.

In addition, two very intriguing relationships involving prompt emission timing proper-ties of GRBs have been found. The first one is the lag-luminosity relation (Norris et al., 2000) and the second one is the variability-luminosity relation (Fenimore and Ramirez-Ruiz, 2000).

Lag-Luminosity Relation

The spectral lag is the difference in time of arrival of high-energy pulses versus low-energy pulses. The observed spectral lag is a common feature in GRBs (Cheng et al., 1995; Norris et al., 1996; Band, 1997). Based on six GRBs with known redshifts, Norris et al. (2000) found an anti-correlation between the spectral lag and the isotropic peak luminosity which is shown in Figure 2.11. Further evidence for this correlation was provided by Norris (2002), Gehrels et al. (2006), Schaefer (2007), Stamatikos (2008) and Hakkila et al. (2008). In this work, we will study this relation in detail and extend it to the GRB source-frame.
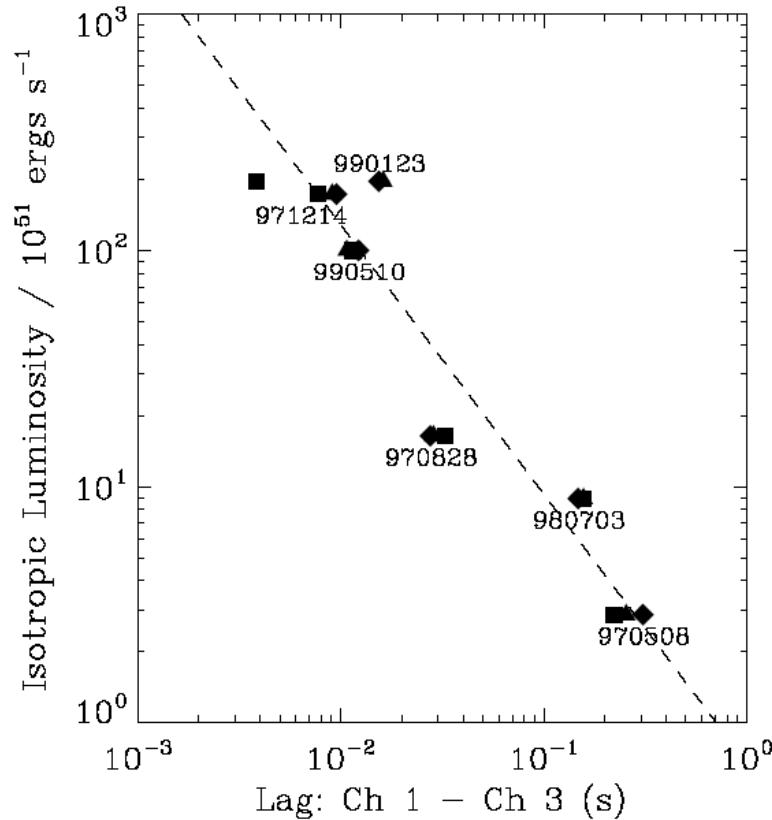
Figure 2.11 Lag–Luminosity relation discovery plot from (Norris et al., 2000). The spectral lag (τ) is measured between two BATSE energy channels $25 - 50$ keV and $100 - 300$ keV. The dashed line is the power-law fit yielding $L_{53} \approx 1.3 \times (\tau/0.01s)^{-1.14}$.

Variability-Luminosity Relation

The time variability in GRBs is crucial to our understanding of the characteristic size associated with GRBs. In 2000, Fenimore and Ramirez-Ruiz first proposed a correlation between variability of GRBs and peak isotropic luminosity (Fenimore and Ramirez-Ruiz, 2000) (see Figure 2.12 and Figure 2.13 in a more recent study with $Swift$ bursts). Since then a number of authors have provided further support for this correlation (Reichart et al., 2001; Guidorzi, 2005; Guidorzi et al., 2005, 2006; Li and Paczyński, 2006; Rizzuto et al., 2007). In these works, the variability is obtained by subtracting a smoothed light curve from the original data (a process referred as de-trending). Several smoothing techniques are employed to de-trend the light curve. The existence of the variability-luminosity correlation suggests that the prompt emission light curve is embedded with temporal information related to the microphysics of GRBs. However, the lack of a universally accepted definition for variability is a major shortcoming and poses problems in comparing and evaluating the results of previous studies. In this work, we will investigate an alternative variability measure based on Fourier power spectra and propose a potentially new correlation between frequency and luminosity of GRBs.
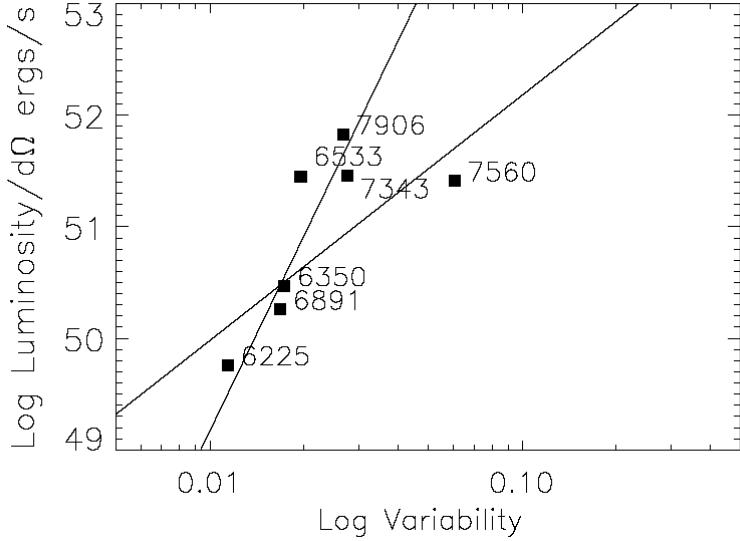
Figure 2.12 Variability-Luminosity discovery plot from (Fenimore and Ramirez-Ruiz, 2000). The six BATSE bursts with known redshifts are labelled by the BATSE trigger numbers. The two solid lines bound the region that contains the average of the distribution.
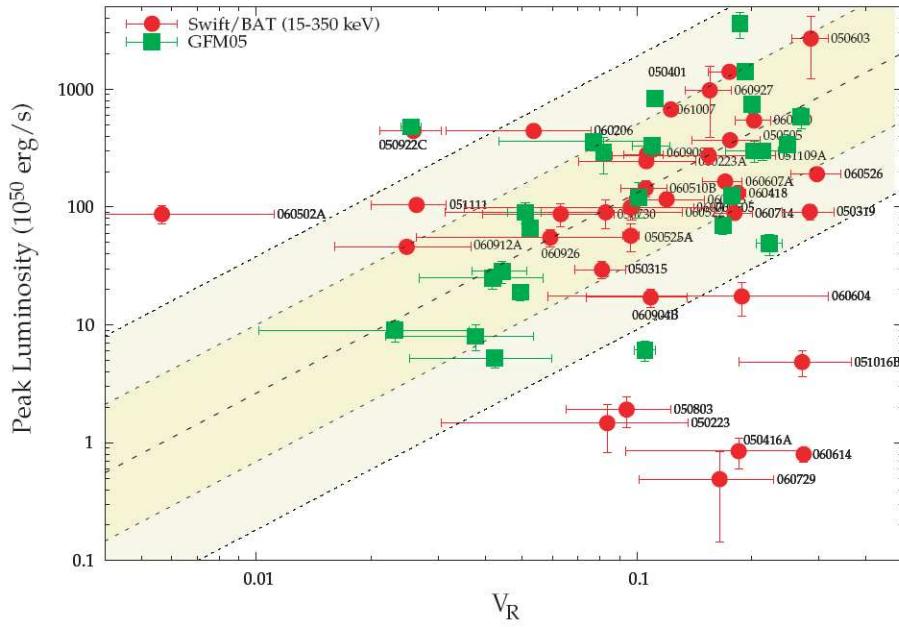
Figure 2.13 More recent Variability-Luminosity plot from (Rizzuto et al., 2007). Here V_R is the variability definition introduced by Reichart et al. (2001). Red circles shows a sample of 36 $Swift$ bursts. For comparison a sample of 25 GRBs from Guidorzi et al. (2005) (GFM05) is shown in green squares. The shaded areas show the 1σ and 2σ regions around the best-fitting power law obtained by Guidorzi et al. (2006) with a slope of 1.7.

Chapter 3

GRB Theory

3.1 Introduction

In the early 1990's there were more than 100 potential models to describe the phenomenon of GRBs. However, more constraining observations over the years have resulted in the development of a 'standard model' to describe the main properties of GRBs with well understood physics.

3.2 The Standard Model for GRBs

3.2.1 The Basic Fireball Model

The basic properties that we can measure for a GRB are its duration, observed flux, redshift or the distance, and timing variability. It has been found that GRB light curves show millisecond variability (Schaefer and Walker, 1999; Walker et al., 2000). Combining fast millisecond variations with the fact that GRBs are cosmological, these measurements imply that at the source, GRBs must have energies of the order of $10^{51}-10^{55}$ erg assuming isotropic emission concentrated into a region of a few thousand kilometers. This huge energy released in a very small volume is thought to lead to the formation of a fireball consisting of electrons, positrons, and gamma-ray photons.

The release of a huge amount of energy in a small volume in a small time will result in an environment extremely opaque to pair creation. The spectrum of this type of plasma

is expected to be thermal. However, GRBs show non-thermal spectra[1], which means that there is a low density of photons at the source. This problem is known as the compactness problem. We can overcome this problem by assuming that the fireball expands relativistically. The highly relativistic expansion of the fireball will blue shift photons at the observer frame and it will also make time scales look shortened at the observer frame. If the Bulk Lorentz factor[2] of the relativistic outflow is given by Γ then these effects can be summarized as follows.

- The observed photons get softer by a factor of Γ at the co-moving frame.

- The emitting region get increased by a factor of Γ^2 at the co-moving frame.

- Due to the relativistic beaming, the relative angle at which the photons interact is less than Γ^{-1}. This will result in a reduction of the effective cross section for pair production given that Γ is large ($\Gamma \sim 100$).

These three effects due to relativistic expansion reduce the optical depth for pair creation below unity.

The most fundamental property of the fireball is its initial energy E_0. In the fireball there are M_0 baryons (electrons have negligible mass) with mean energy per baryon, $\eta = E_0/M_0 c^2$. M_0 is also called the baryon loading of the fireball. Note that for a relativistic fireball $M_0 \ll E_0/c^2$. Initially, the fireball has a radius of $R_{\rm in}$ and a bulk Lorentz factor of about one. However, the individual particles in the fireball have random isotropic velocities with a mean Lorentz factor $\gamma \sim \eta$. Since the initial optical depth of the fireball is extremely high, the only way to dissipate the highly super-Eddington luminosity and the internal energy is to accelerate baryons radially as a bulk motion. In other words, the internal energy of the fireball is converted into bulk kinetic energy of the baryons. A phase of acceleration is initiated with this expansion. The expansion is adiabatic and is described by the equation $T'V'^{\gamma_a - 1} = $ constant, where T' and V' are the rest-frame temperature and the volume of the emitting region. In this case the adiabatic index, γ_a is equal to 4/3. This will result in $T'V'^{1/3} = $ constant. However, $V' \propto R^3$ where R is the radius of the fireball. So in the initial stage $T' \propto R^{-1}$. The total internal and kinetic energy of the fireball in the

---

[1]Recently with *Fermi* gamma-ray telescope, there has been some evidence showing an additional thermal component in the GRB spectra (Guiriec et al., 2010)

[2]The Lorentz factor, γ, is given by $\gamma = \frac{1}{\sqrt{1-\beta^2}}$ where $\beta = \frac{v}{c}$.

observer-frame is given by $E_0 = \Gamma M_0(kT'/m_p + c^2)$. Here m_p is the mass of the proton. For ultra-high temperatures where the particles are relativistic, the first term is dominant and the equation reduces to $E_0 \propto \Gamma T'$. However, the total energy of the fireball is constant; hence $T' \propto \Gamma^{-1}$ giving rise to $\Gamma \propto R$. Hence, the bulk Lorentz factor of the expanding gas increases linearly with R until $R = R_{\mathrm{sat}}$ where $R_{\mathrm{sat}} \propto \Gamma_{\mathrm{max}} R_{\mathrm{in}}$, with $\Gamma_{\mathrm{max}} \sim \eta \sim E_0/M_0c^2$, and $R_{\mathrm{sat}} = \eta R_{\mathrm{in}}$. During this initial phase of the fireball expansion the thermal energy of the fireball is adiabatically transformed into the bulk motion energy of the baryons. After $R = R_{\mathrm{sat}}$ the fireball expands with constant $\Gamma = \Gamma_{\mathrm{max}}$. After reaching the maximum bulk Lorentz factor, R is large enough that the interaction with the surrounding medium starts to decelerate the ejecta at $R = R_d$. Generally, $R_{\mathrm{in}} < R_{\mathrm{sat}} < R_d$. During the expansion of the fireball all the matter moved with $v \approx c$. Hence, all the matter in the fireball piles up in a shell with a thickness, $\delta R \propto R\Gamma^{-2}$ (Meszaros et al., 1993).

3.2.2 The Fireball Shock Model

The initial fireball model had problems explaining the observed non-thermal GRB spectra and their time scales. To overcome these problems Rees and Meszaros proposed a new version of the basic fireball model called the 'fireball shock model' (Rees and Meszaros, 1992; Meszaros and Rees, 1993). The fireball shock model invokes relativistic shocks to generate the non-thermal radiation observed in GRBs. According to the model there are two types of shocks: 'external shocks', which represent the shock of the fireball on the external surrounding medium of the source. The external shock description anticipated the multi-wavelength afterglow detection. External shocks also generate a secondary shock that travels towards the source called reverse shock. The second type of shock is called the 'internal shock'; this occurs inside the fast moving fireball due to time-varying outflow from the central engine. These time-varying outflows create shells with various Lorentz factors. The collision of fast moving later ejected shells with slow early ejected shells generate internal shocks. A schematic diagram of the fireball shock model is shown in Figure 3.1.

The acceleration phase of the fireball ends when $\Gamma = \Gamma_{\mathrm{max}}$ and $R = R_{\mathrm{sat}}$. Then a coasting phase begins with the ejecta moving at Γ_{max}. The pair recombination starts at radii below R_{sat} and continues through the coasting phase, bringing down the optical depth of the fireball. The radius at which the optical depth (τ_{ph}) of the fireball reaches unity is called the photospheric radius (R_{ph}). Beyond R_{ph} the radiation from the fireball can escape.
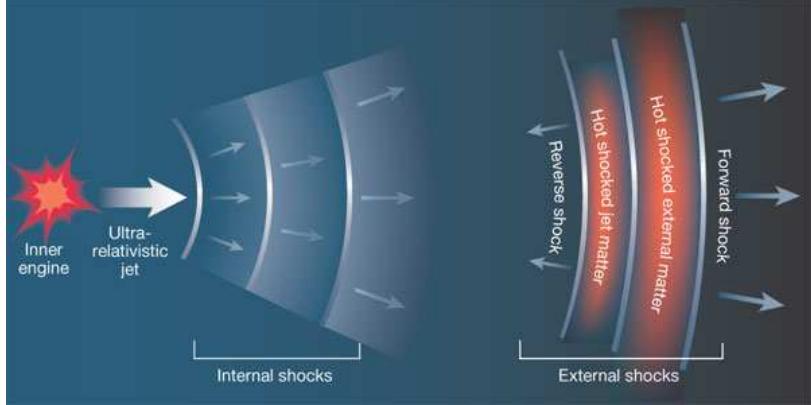
Figure 3.1 Schematic diagram of the Fireball Shock Model.

However, the emitting radiation will reach the observer only if the velocity vector of the radiating matter makes an angle smaller than Γ^{-1} with the line-of-sight of the observer. The fireball shock model is based on the assumption that internal shocks will occur when the optical depth of the fireball falls below unity beyond the R_{ph}. These shocks will convert bulk kinetic energy of the out-flowing material into internal energy of non-thermal particles and radiation. These internal shocks are responsible for the prompt gamma-ray radiation. The external shock occurs after the internal shocks when the fireball ejecta collides with the external medium. According to the model, external shocks are responsible for the afterglow emission with energies ranging from gamma-rays to radio. The shocked particles radiate through synchrotron and/or inverse Compton processes.

The fireball shock model does not depend on how the initial energy, E_0, was produced. It describes only what happens after that. Possible sources of the initial energy can be either collapse of a massive star or coalescence of compact objects. We discuss more about these GRB progenitor models in section 3.3.

3.2.3 GRB Emission Models (Radiation Mechanisms)

Presumably, GRBs involve accelerated relativistic electrons and relatively strong magnetic fields. Hence, synchrotron emission mechanisms may play a major role in both GRB prompt emission and its afterglow. Here we discuss typical characteristics of synchrotron emission.

The synchrotron emission is characterized by three parameters: (1) The Lorentz factor of the relativistic electrons (γ_e), (2) the strength of the magnetic field (B) and (3) the

26

bulk Lorentz factor of the emitting material (Γ). Using these parameters, the characteristic synchrotron frequency ν_{syn} in the observer frame is given by the following equation.

$$\nu_{\mathrm{syn}}(\gamma_{e,\mathrm{obs}}) = \frac{q_e B}{2\pi m_e c}\gamma_e^2 \Gamma \tag{3.1}$$

Here, q_e and m_e are the charge and the mass of the electron. The power emitted by a single electron in the co-moving frame of the emitting material is given by (Melia, 2009)

$$P'_{\mathrm{syn}} = \frac{4}{3}\sigma_T c U_B \gamma_e^2, \tag{3.2}$$

where U_B is the magnetic energy density given by $B^2/8\pi$, and σ_T is the Thompson cross-section. Here we assumed that the electron does not lose a significant fraction of its energy due to radiation.

The power emitted by a single electron in the observer frame is $P_{\mathrm{syn}} = \Gamma^2 P'_{\mathrm{syn}}$. The cooling time of a electron in the co-moving frame of the emitting material is given by,

$$t' = \gamma_e m_e c^2 / P'_{\mathrm{syn}}. \tag{3.3}$$

The cooling time of a electron in the observer frame is $t \sim \Gamma^{-1}t'$. Hence, the observed synchrotron cooling time can be expressed as

$$t_{\mathrm{syn}}(\gamma_e) = \frac{1}{\Gamma}\frac{3m_e c}{4\sigma_T U_B \gamma_e} \propto \gamma_e^{-1}\Gamma^{-1}. \tag{3.4}$$

This cooling time can also be written in terms of the electron frequency in the observer frame as follows.

$$t_{\mathrm{syn}}(\nu) = \frac{3}{\sigma_T}\sqrt{\frac{2\pi m_e c q_e}{B^3 \Gamma}}\,\nu^{-1/2} \sim \Gamma^{-1/2}\nu^{-1/2} \tag{3.5}$$

Here t_{syn} gives a lower limit to the variability timescale of GRBs. That means that a single pulse in a GRB cannot be shorter than t_{syn}. However, this is not a strong constraint as t_{syn} is much smaller than pulse durations in GRBs (Piran, 2005).

In order to calculate the synchrotron spectrum radiated by a population of electrons we need know the electron energy distribution. Let's assume that the energies γ_e of the electrons follow a power-law distribution with an index of p above a certain minimal Lorentz factor γ_m. That is $N(\gamma_e)d\gamma_e \propto \gamma_e^{-p}d\gamma_e$ for $\gamma_e > \gamma_m$. This is a fair assumption considering

the fact the one would expect a similar distribution from shock accelerated particles (Sari et al., 1998). Note that $\langle \gamma_e \rangle \propto \gamma_m$ and $p > 2$ in order to keep the energy of the electrons finite.

Most of the electrons in the population can be considered to have an energy close to $\gamma_m m_e c^2$. Hence, γ_m represents a *typical electron Lorentz factor* in the population and $\nu_m = \nu_{\mathrm{syn}}(\gamma_m)$ gives the corresponding *typical, synchrotron frequency.*

For simplicity, lets assume electrons are accelerated behind a shock propagating through a uniform, cold medium with particle density n. The Lorentz factor of the shock fluid is given by Γ. The particle density and the energy density of the material behind the shock are given by $4\Gamma n$ and $4\Gamma^2 n m_p c^2$ respectively (Blandford and McKee, 1976). If we assume that a constant fraction ε_e of the shock energy goes in to electrons, then γ_m is given by the following equation (Sari et al., 1998).

$$\gamma_m = \varepsilon_e \frac{(p-2)m_p}{(p-1)m_e}\Gamma \qquad (3.6)$$

If we further assume that the magnetic energy density behind the shock is a constant fraction ε_B of the shock energy (Sari et al., 1998) then the value of the magnetic field in the fluid frame is

$$B = (32\pi m_p \varepsilon_B n)^{\frac{1}{2}}\Gamma c. \qquad (3.7)$$

If $\gamma_e < \gamma_c$ then electrons do not lose a significant amount of energy through radiation. Here γ_c is the *critical Lorentz factor* obtained from $P(\gamma_c)t = \Gamma\gamma_c m_e c^2$. Hence, we get

$$\gamma_c = \frac{6\pi m_e c}{\sigma_T \Gamma B^2 t}. \qquad (3.8)$$

The time t is measured in the observer frame and it provides the time that an electron takes to cool from the initial Lorentz factor $\gamma_e > \gamma_c$ down to γ_c. During the electron cooling process, the frequency of the synchrotron emission varies as γ_e^2 (see Equation 3.1) and electron energy varies as γ_e ($\sim \gamma_e m c^2$). The spectral power, $P_\nu \sim P(\gamma_e)/\nu(\gamma_e)$ varies as $\nu^{-1/2}$ over the frequency range $\nu_c < \nu < \nu(\gamma_e)$, where ν_c is *the critical frequency* defined by $\nu_c = \nu(\gamma_c)$.

The net spectrum emitted by a such an electron consists of three segments (Sari et al., 1998). The flux, F_ν, in the low-energy part corresponding to $\nu < \nu_c$ varies as $F_\nu \propto \nu^{1/3}$.

On the other hand, very high energy electrons emit all their energy at their synchrotron frequency and cool rapidly. The number of electrons with Lorentz factor γ is proportional to $\gamma^{(1-p)}$ ($N \propto N(\gamma)d\gamma \propto \gamma^{-p}d\gamma$) and their energy is proportional to $\gamma^{(2-p)}$ ($E \propto N(\gamma)\gamma d\gamma \propto \gamma^{-p}\gamma d\gamma$). The electrons emit their energy in a frequency, $\nu_{\mathrm{syn}(\gamma)} \propto \gamma^2$. Hence, $F_\nu \propto \gamma^{-2} \propto \nu^{-p/2}$. The high energy part of the spectrum will have a power-law dependance, enabling us to extract directly the electron power-law distribution.

The intermediate energy or frequency region of the spectrum depends on how fast the cooling of the electron distribution occurs. If the $\gamma_m > \gamma_c$ then a large number of the electrons cool down rapidly emitting energy quickly. This scenario is called *fast cooling* (Sari et al., 1998). However, if $\gamma_c > \gamma_m$ then only a small fraction of electrons with $\gamma_e > \gamma_c$ can cool and most of the electrons with $\gamma_e \sim \gamma_m$ do not cool within time t. This second scenario is called *slow cooling*.

The electron distribution emits maximally at ν_c and the maximum power per frequency is given by

$$P_{\nu,\mathrm{max}} = \frac{P(\gamma_c)}{\nu(\gamma_c)} = \frac{m_e c^2 \sigma_T}{3 q_e} \Gamma B. \tag{3.9}$$

In order to obtain the final observable synchrotron spectrum from a distribution of electrons we need to integrate individual electron spectra over the γ_e. In the case of fast cooling scenario the flux at the observer frame, F_ν is given as follows.

$$F_\nu = \begin{cases} (\nu/\nu_c)^{1/3} F_{\nu,\mathrm{max}} & \text{for } \nu_c > \nu \\ (\nu/\nu_c)^{-1/2} F_{\nu,\mathrm{max}} & \text{for } \nu_m > \nu > \nu_c \\ (\nu_m/\nu_c)^{-1/2}(\nu/\nu_m)^{-p/2} F_{\nu,\mathrm{max}} & \text{for } \nu > \nu_m \end{cases} \tag{3.10}$$

Here $\nu_m = \nu(\gamma_m)$ and $F_{\nu,\mathrm{max}} = N_e(P_{\nu,\mathrm{max}}/4\pi D_L^2)$. D_L is the luminosity distance to the source. In the case of the slow cooling scenario the observed flux is given by (Sari et al., 1998):

$$F_\nu = \begin{cases} (\nu/\nu_m)^{1/3} F_{\nu,\mathrm{max}} & \text{for } \nu_c > \nu \\ (\nu/\nu_m)^{-(p-1)/2} F_{\nu,\mathrm{max}} & \text{for } \nu_c > \nu > \nu_m \\ (\nu_c/\nu_m)^{-(p-1)/2}(\nu/\nu_c)^{-p/2} F_{\nu,\mathrm{max}} & \text{for } \nu > \nu_c \end{cases} \tag{3.11}$$

The Figure 3.2 shows the observed synchrotron spectrum for the two scenarios.
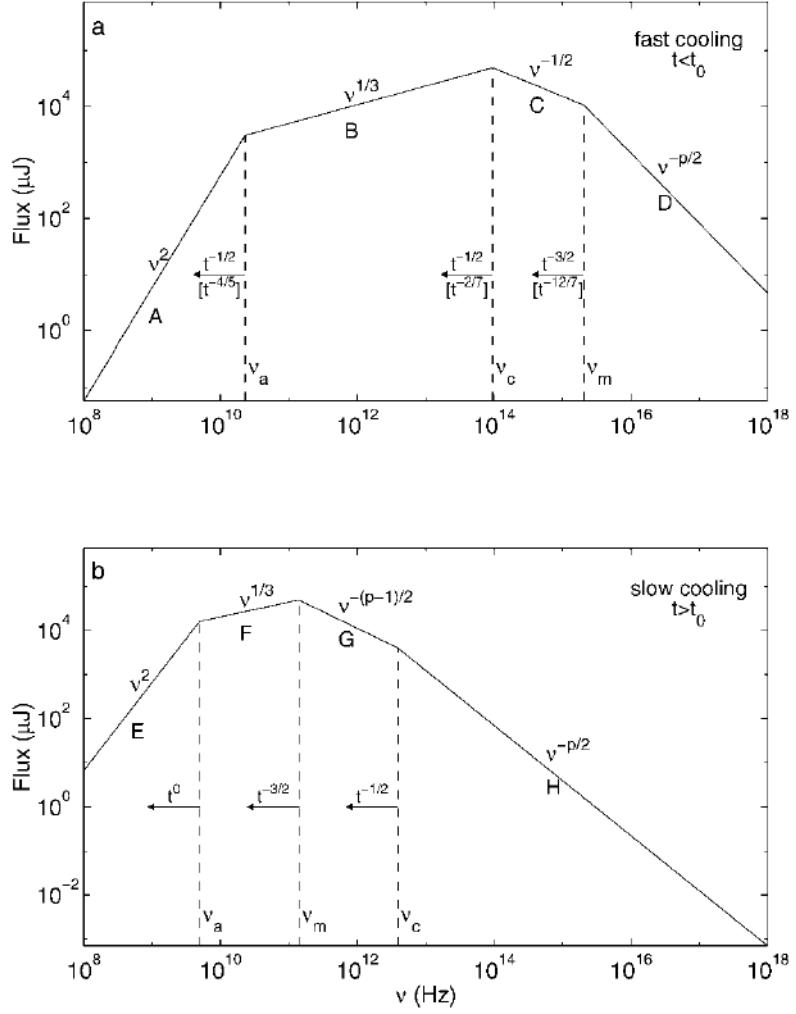
Figure 3.2 Spectrum of synchrotron emission from electrons accelerated in a relativistic shock in two cases (Sari et al., 1998). (1) Fast cooling: This is the condition one would expect during the early prompt phase. The spectrum composed of four segments identified as A, B, C, and D. Segment C corresponds to the hard X-ray region. The frequencies, ν_m, ν_c, and ν_a, decrease with time as indicated with arrows. The time dependance or scaling above the arrow corresponds to an adiabatic evolution, and the scaling in square brackets corresponds to a fully radiative evolution. (2) Slow cooling: This is the situation at later times and the evolution is always adiabatic. The four segments of the spectrum are labelled as E, F, G, and H. In both cases self-absorption is important below ν_a. At $t = t_o$, the spectrum changes from fast cooling to slow cooling.

30

The fast cooling is expected to take place during the GRB prompt phase. The initial relativistic shock cools down quickly, converting the kinetic energy of the electrons into radiation efficiently. The transition from fast cooling to slow cooling is expected to happen during the late prompt phase of the GRB or early afterglow phase.

Synchrotron self-absorption becomes important at low frequencies (in the radio range) of the spectrum. The self-absorption causes a steep cut-off of the low-energy spectrum (below the *synchrotron self-absorption frequency*, ν_a) which goes as $\nu^{5/2}$ or ν^2 (see Figure 3.2). The synchrotron self-absorption is not important during the GRB prompt phase; however, it is observed regularly during the afterglow phase (in radio wavelengths).

The synchrotron emission mechanism is fairly successful at explaining GRB afterglow properties. However, the properties of the prompt emission cannot be explained entirely by the synchrotron emission mechanism. There are two issues that are not satisfactorily explained. The first one is that a significant fraction of GRB prompt emission spectra are harder than $F_\nu \propto \nu^{-1/2}$, which is the typical spectrum expected from the synchrotron emission in the standard internal shock model. The second issue is that the efficiency of converting the wind kinetic energy into hard X-ray radiation is not high enough to power a GRB. Many alternative mechanisms such as synchrotron self-Compton have been proposed, but the radiation mechanism of the prompt emission of GRBs still remains as an open question.

3.3   GRB Progenitor Models

The central engine that produces the initial energy, E_0, is hidden from direct observation. However, the observed temporal structure is thought to reflect the central engine activity. The central engine must satisfy the following general features:

- Capable of producing an extremely relativistic energy flow containing $\approx 10^{51} - 10^{55}$ erg.

- Highly variable flow resulting in highly variable light curves.

- Activity can last from a fraction of a second to a few hours.

- Possibility of late time activity that may cause X-ray flares.

- Relatively rare event as suggested by observed GRB rates.

There are three ways to produce lots of energy in nature: nuclear, gravitational, and rotational. The nuclear energy does not have enough efficiency to power a GRB. For example, the proton-proton chain that is responsible for energy production in stars has an efficiency of about 0.0067. The gravitational potential energy released during a collapse of a massive star or during the merger of two stars has enough energy to power a GRB. The rotational energy from a black hole also may be enough to power a GRB. It is also possible that both of these last two mechanisms play a role in GRB energy release.
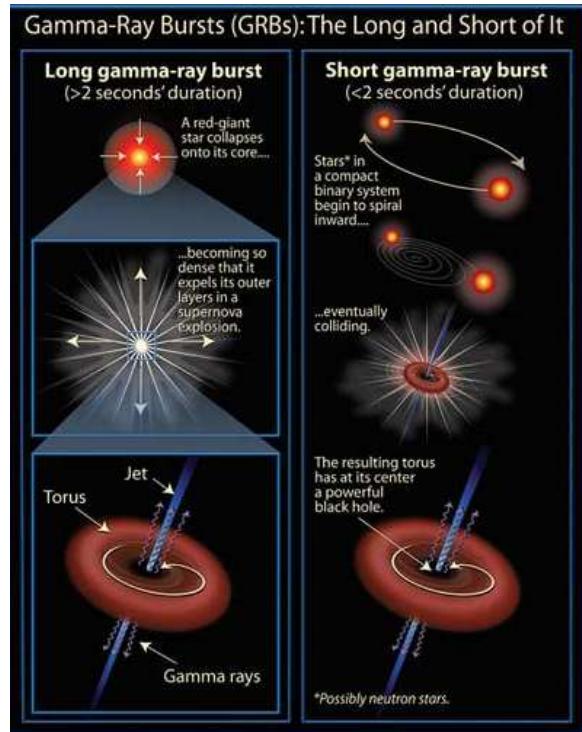
Figure 3.3 Schematic scenarios for plausible progenitors of long and short GRB. The exact nature of the GRB progenitors is unknown, although it is possible that long GRBs come from the collapse of massive, rapidly rotating stars and short GRBs result from the merger of compact objects.

It is generally accepted that at least two main classes of progenitors are responsible for GRBs as illustrated in Figure 3.3. Long GRBs are believed to occur from the collapse of massive stars (Woosley and Heger, 2006; Woosley and Bloom, 2006). These progenitors can be a single Wolf-Rayet (WR) star or a system of two WRs. The coalescence of two compact objects such as two neutron stars or a black hole and a neutron star is thought to be the progenitor of short GRBs (Eichler et al., 1989; Narayan et al., 1992). In both

these scenarios, the progenitors will create a fast accreting black hole with a transient torus disk. In the first case (long GRBs) the disk might have several solar masses worth of material. However, in the second case (short GRB) the disk may be less massive (a few $\times 10^{-1} M_\odot$). Two large reservoirs of energy are available in both these cases. That is the gravitational binding energy of the orbiting disk and the spin energy of the central black hole (Meszaros and Rees, 1997). The first mechanism can provide up to 40% of the rest mass of the disk[3], while the second mechanism can provide up to 29% of the rest mass of the black hole (Blandford and Znajek, 1977).

There are a number of possible ways to extract energy from these black hole – accreting torus systems.

- Thermal energy due to the viscous dissipation in the disk released via neutrinos. The neutrino annihilation process creates high energy electrons via $\nu + \bar{\nu} \rightarrow e^+ + e^-$.

- Dissipation of magnetic fields (Poynting flux) that are generated due to the differential rotation of the accretion disk.

- The rotational energy of the central black hole itself can be directly extracted through the Blandford and Znajek (1977) process.

It is interesting to note here that the total amount of energy available can be greater than the the rest mass of the accretion disk. The reason is that the black hole is rapidly spinning and more massive than the disk.

The evidence supporting the collapsar model, which has been extensively studied as the possible progenitor of long GRBs can be summarized as follows.

- The association of several nearby long GRBs with supernovae.

- Long GRB host galaxies have a high specific star formation rate.

- Long GRBs trace star-forming regions of host galaxies.

However, this evidence is far from settled. There are a number of unclear issues such as the nature of the progenitor star (isolated or binary), the production of the jet, and its ability to plough through the stellar envelope.

---

[3]40% is the theoretical limit for a torus disk around a maximally rotating black hole

The situation with short bursts is more complicated. The only thing we know with high confidence is that short GRB progenitors are different from long GRB progenitors. We also know that short GRBs are not associated with supernovae. In addition, the observed properties of short GRBs that are listed in section 2.5.2 are consistent with the merger model. However, they do not necessarily rule out other alternative models.

3.4 Interpretations of Temporal Properties of GRBs

3.4.1 Timescales in Relativistic Flows

When we discuss time scales in the context of GRBs, it is important to understand the presence of three frames: 1) the observer frame or the frame of the detector, 2) the source frame or the rest frame of the cental engine, and 3) the comoving frame of the shocked emitting material. The transformation of time scales from the source frame to the observer frame is straight forward. The difference between the two frames occurs due to the expansion of the universe (cosmological redshift, z) and multiplication by a factor of $(1 + z)$ will transform all time scales in the source-frame to the observer-frame.

The particles in the comoving frame move relativistically with velocity v relative to the source-frame. This velocity can be represented by $\beta = v/c = (1 - 1/\Gamma^2)^{1/2}$. Here Γ is the Lorentz factor of the particles in the flow relative to the GRB source-frame. Consider a single electron that emits two photons at radii R_1 and R_2 ($R_1 < R_2$). The first photon emitted at R_1 will reach an observer in the rest-frame of the GRB before the photon emitted at R_2. The time difference between the two photons is given by,

$$\Delta T = \frac{R_2 - R_1}{v} - \frac{R_2 - R_1}{c} = \frac{R_2 - R_1}{c}\left(\frac{1}{\beta} - 1\right). \tag{3.12}$$

For $\Gamma \gg 1$ (using $\beta^{-1} = (1 - 1/\Gamma^2)^{1/2} \approx 1 + 1/(2\Gamma^2)$),

$$\Delta T = \frac{R_2 - R_1}{2c\Gamma^2} = \frac{\Delta R}{2c\Gamma^2} = T_R \tag{3.13}$$

Here, T_R is the characteristic *radial timescale*. If the emission is continuous from R_1 to R_2 this characteristic time will limit the duration of the peaks inside the GRB.

Another characteristic timescale for GRBs can be obtained considering the curvature of the radiating shell. Figure 3.4 shows that photons emitted along the line-of-sight have to
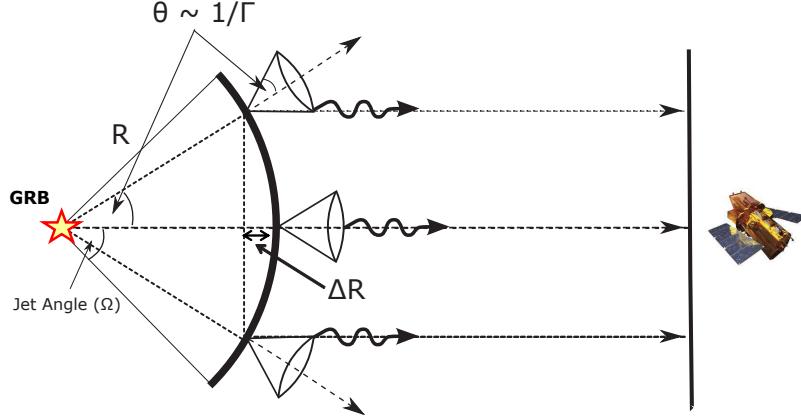
Figure 3.4 Illustration of the meaning of angular timescale.

travel less far compared to photons from part of the shell moving at an angle θ relative to the line-of-sight. The path difference between the two photons is $\Delta R = R(1 - \cos\theta)$. Thus, the arrival time difference between the two photons is,

$$T_{\text{ang}} = \frac{R}{c}(1 - \cos\theta). \tag{3.14}$$

T_{ang} is the characteristic *angular timescale* (or *angular spreading time*). Since $\theta = 1/\Gamma$, for $\Gamma \gg 1$ we get (using $\cos\theta \approx 1 - \theta^2/2$),

$$T_{\text{ang}} \approx \frac{R}{c}\frac{\theta^2}{2} = \frac{R}{2c\Gamma^2}. \tag{3.15}$$

Hence, for an observer close to the line-of-sight, observed timescales T_R and T_{ang} are characterized by $T \propto R/(2c\Gamma^2)$, i.e., both timescales have the same dependency in R and Γ (Vedrenne and Atteia, 2010).

3.4.2 Modelling of GRB Pulses

Distribution of Pulse Properties

A GRB light curves consists of one or more pulses. A pulse has a number of properties: 1) rise time (t_{r}), 2) fall time (t_{f}), 3) pulse amplitude (C), 4) pulse area (A_{p}), 5) pulse duration (or width, w) or full-width at half-maximum $(FWHM)$. For GRBs, all these pulse properties show log-normal distributions (see Quilligan et al. (2002) and references

therein). The log-normal distribution also applies to the spectral properties such as E_{p} of the GRBs (Preece et al., 2000).

These log-normal distributions arise due to a combination of independent statistical processes. Thus, the overall distribution of these parameters identifies the statistical process, but does not provide much information about the underlying events that causes the formation of the pulse profile and spectral profile. In the standard internal shock model, a number of factors can contribute to the timing and spectral profile of pulses (Rees and Meszaros, 1992, 1994; Piran, 1999):

1. The masses, thickness and Lorentz factors of interacting shells in the blast wave

2. The nature of the jet i.e., uniform jets, structured jets, etc

3. The distance of the colliding shells from the central engine

4. The curvature of the colliding shells

5. The energy conversion mechanism

6. The radiation mechanism in the shocks such as synchrotron, synchrotron-self Compton, or inverse Compton scattering

These factors combine together to produce the log-normal distribution of timing and spectral properties of GRB pulses.

Pulse-Width Evolution with Time

There is evidence that the prompt emission light curves of GRBs show multiple pulses whose width (w) on average are the same (Ramirez-Ruiz and Fenimore, 2000). That is, on average there is no lengthening of w with time since the trigger during the prompt phase. This implies that the emission episodes, on average, should arise from regions with similar sizes and possibly the same distance from the cental engine. However, a recent study by Margutti et al. (2010) found that for X-ray flares, the pulse width evolves with time. More specifically, X-ray flares evolve with time to larger widths.

Pulse-Width Evolution with Energy

Fenimore et al. (1995) has shown that the prompt gamma-ray pulse width, w, varies as a function of energy ($w \propto E^{-0.4}$). Norris et al. (1996) also confirmed this relation. This

type of energy dependance of the pulse width has also been observed for X-ray flares as well (Chincarini et al., 2010; Margutti et al., 2010).

Relations between Pulse Properties

There are a number of relations between various GRB pulse properties. For example, the rise time and fall time of pulses are correlated with the width of the pulse (for more details see Quilligan et al. (2002)).

The Pulse Start Conjecture

The pulse start conjecture states that GRB pulses start at the same time in different energy bands. This conjecture was first proposed by Nemiroff (2000) and later tested by Hakkila and Nemiroff (2009) with a large number of BATSE GRB pulses. The pulse start conjecture was generally found to hold for prompt gamma-ray pulses. For long GRBs the typical uncertainty is ~ 0.4 seconds and for short GRBs the uncertainty is ~ 0.1 seconds (Hakkila and Nemiroff, 2009). The implication of this result is that energy is injected at the beginning of each and every GRB pulse, and the subsequent spectral evolution dictates the peaking and the decay of the pulse. X-ray flare pulses, however, do not follow the pulse start conjecture (Margutti et al., 2010).

3.4.3 Models for Spectral Lag and Lag-Luminosity Relation

Many authors have tried to explain the physical cause of the lag-luminosity relation and a number of models have been proposed. Salmonson (2000) argues that the anti-correlation is due to the variations in the line-of-sight velocity of various GRBs. Ioka and Nakamura (2001) suggest that the relation is a result of variations of the off-axis angle when viewing a narrow jet. Schaefer (2004) invokes a rapid radiation cooling effect to explain the correlation. This effect tends to produce short spectral lags for highly luminous GRBs. We will discuss this topic further in Chapter 8.

3.4.4 Variability in GRB Prompt Emission Light Curves

In the collapsar model, the duration of a GRB is determined by the collapse timescale of the massive stellar core. For Helium cores with mass ranging from $8M_\odot$ to $15M_\odot$, this timescale is about 10 seconds. Stellar collapses that create long GRBs are assumed to be rotating

sufficiently rapidly to form an accretion disk around the newly formed black hole (Woosley, 1993; MacFadyen and Woosley, 1999).

Continuously in-falling gas briefly resides in the accretion disk before being drawn into the black hole. Short timescales are expected due to the variability in the accretion rate and due to the jet instabilities as the ultra-hot jet material expands along the polar axis of the star while interacting with the stellar envelope.

Accretion disks with radius $\sim 10^7$ cm have typical accretion timescales of ~ 0.01 seconds. MacFadyen and Woosley (1999) have shown that fluctuation in the accretion rate caused by instabilities have timescales of the order of 50 ms. It is conceivable that in models where accretion energy is used to power relativistic polar jets, these fluctuations in accretion may translate into variations in the jet Lorentz factor, possibly causing the variability in the GRB light curve.

Another source of variability is instabilities arising due to the propagation of a relativistic jet through the stellar envelope. Instabilities in the flow caused by shear between the jet and the material in the star envelope may results in variable jet Lorentz factors. Variability timescales in this case are of the order of 0.1 seconds (Kobayashi et al., 2002).

3.4.5 Presence of Central Engine Information in the Light Curve

The existence of the correlations such as lag-luminosity and variability-luminosity relations suggests that the prompt emission light curve is embedded with temporal information related to the microphysics of GRBs. Recent simulation studies (Morsony et al., 2010) involving the propagation of a jet through stellar material indicate that this temporal variability, at different time scales, possibly relating to the central engine and the propagation of the jet itself, may be directly measurable from the prompt emission.

Chapter 4

Instrumentation

4.1 Introduction

After the Burst and Transient Source Experiment (BATSE) on the Compton Gamma Ray Observatory (CGRO), $Swift$ has been the leading GRB mission for the last five years. Unprecedented quick slewing capability and prompt localization of $Swift$ enabled deep afterglow searches and redshift determinations for many GRBs. In this thesis we utilize the data from the $Swift$ satellite. In this chapter, we summarize the basic properties of the instruments and the standard data analysis procedures of $Swift$.

4.2 The *Swift* Mission

4.2.1 *Swift* Satellite

The *Swift* satellite, which was launched on November 20, 2004, is a multiwavelength observatory for gamma-ray burst (GRB) astronomy. It is a first-of-its-kind autonomous rapid-slewing satellite for transient astronomy. *Swift* has three instruments on board. These instruments, Burst Alert Telescope (BAT), X-ray Telescope (XRT), and UV/Optical Telescope (UVOT), are shown on the spacecraft in Figure 4.1 (Gehrels et al., 2004). The XRT and UVOT are co-aligned and pointed near the center of the BAT field of view (FOV).
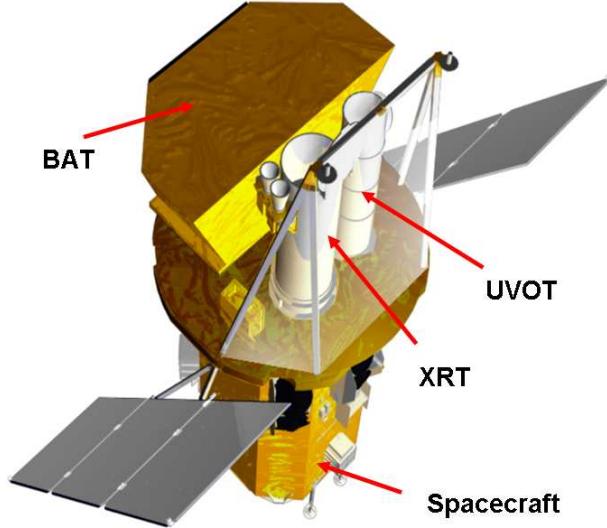
Figure 4.1 *Swift* satellite

Table 4.1 *Swift* Mission Characteristics

Mission Parameters	Value
Slew rate	50° in less than 75 s
Orbit	Low Earth, 600 km altitude
Inclination	22°
Launch vehicle	Delta 7320-10 with 3 m fairing
Mass	1450 kg
Power	1040 W
Launch date	November 20, 2004

4.2.2 Burst Alert Telescope (BAT)

BAT is a highly sensitive, large field-of-view (FOV) instrument designed to provide critical GRB triggers and $4'$ positions. BAT has capability to detect bursts 3 times fainter than the BATSE detector aboard CGRO. It has a field-of-view of 2 steradians (one sixth of the sky). The BAT detects about 100 GRBs per year. Within the first ~10 s of detecting a burst, BAT will calculate an initial position, decide whether the burst merits a spacecraft slew, and, if worthy, sends the position to the spacecraft. Basic characteristics of BAT are given in Table 4.2 (Barthelmy et al., 2005). We will discuss the BAT instrument in more detail in section 4.3.

Table 4.2 Burst Alert Telescope (BAT) Characteristics

BAT Parameter	Value
Energy range	15–150 keV
Energy resolution	~ 7 keV
Aperture	Coded mask, random pattern, 50% open
Detection area	5240 cm^2
Detector material	CdZnTe(CZT)
Detector operation	Photon counting
Field of view	1.4 sr (half coded)
Detector elements	256 modules of 128 elements module^{-1}
Detector element size	$4 \times 4 \times 2$ mm^3
Coded-mask cell size	$5 \times 5 \times 1$ mm^3 Pb tiles
Instrument dimensions	2.4 m $\times$ 1.2 m $\times$ 1.2 m
Telescope PSF	< 20"
Source position and determination	1'– 4'
Sensitivity	$\sim 10^{-8}$ ergs cm^{-2} s^{-1}
Number of bursts detected	>100 yr^{-1}

4.2.3   X-ray Telescope (XRT)

XRT is a focusing X-ray telescope with a 110 cm^2 effective area CCD detector, 23' FOV, 18" resolution, and 0.2-10 keV energy range. XRT uses a grazing incidence Wolter 1 telescope to focus X-rays on to a CCD. XRT is able to obtain spectra and images of GRB afterglows. The images are primarily used to improve the burst locations reported by BAT. The details of XRT are described in Burrows et al. (2005a).

Table 4.3 X-Ray Telescope (XRT) Characteristics

XRT Parameter	Value
Energy range	0.2–10 keV
Telescope	JET-X Wolter 1
Detector	E2V CCD-22
Effective area	110 cm^2 at 1.5 keV
Detector operation	Photon counting, integrated imaging, and timing
Field of view	23".6 $\times$ 23".6
Detector elements	600×602 pixels
Pixel scale	2".36
Telescope PSF	18" HPD at 1.5 keV
Sensitivity	2×10^{-14} ergs cm^{-2} s^{-1} (1 mcrab) in 10^4 s

4.2.4   UV/Optical Telescope (UVOT)

The Ultraviolet/Optical Telescope (UVOT) is an optical and ultraviolet, 30 cm aperture Ritchey-Chretien telescope. It has six bandpass filters operating over a range of 170–650

nm, plus two grisms. The UVOT has a FOV of 17×17 square arcminutes with limiting sensitivity of 24th magnitude in 1000 second exposure and with 0.3 arcsecond position accuracy.

There are two data collection modes for the UVOT: event mode and imaging mode. In the event mode, UVOT records time-tagged photons events with ~ 11 ms timing resolution. In imaging mode, photons are added up to create an image. The images are used for $0.3 - 2.5$ arc-second position localizations. Spectra created using event-event data are used to determine redshifts and Lyman-alpha cut-offs. The details of UVOT are described in Roming et al. (2005).

Table 4.4 Ultraviolet/Optical Telescope (UVOT) Characteristics

UVOT Parameter	Value
Wavelength range	170–600 nm
Telescope	Modified Ritchey-Chretien
Aperture	30 cm ($\sim$12 inch) diameter
f number	12.7
Detector	Intensified CCD
Detector operation	Photon counting
Field of view	17" $\times$ 17"
Detection elements	2048 $\times$ 2048 pixels
Telescope PSF	0".9 FWHM at 350 nm
Colors	6
Sensitivity	$B = 24$ in white light in 1000 s
Pixel scale	0".5

4.2.5 *Swift* Observing Scenario

The BAT detects GRBs through a sudden increase in counts over the background level, which are called rate triggers. It also has a second type of trigger called image trigger, which triggers on new significant sources found in the BAT sky image. Once triggered, BAT calculates the location of the burst onboard and sends it to the spacecraft. Then the spacecraft autonomously repoints itself to the burst location (approximately in 20 to 75 seconds). By doing that it brings the burst within the field-of-view of high resolution narrow field instruments (XRT and UVOT). Once slewed, XRT and UVOT will send more accurate position information of the burst to ground observers to do followup observation with large ground based observatories.

4.3 The BAT Instrument

4.3.1 Design Overview

The Burst Alert Telescope or BAT is the primary instrument on $Swift$, which was designed and built at the NASA Goddard Space Flight Center. Since photons which have energy greater than about 15 keV are difficult to focus using mirrors or any other method, BAT utilizes the code-mask aperture technique to localize gamma-ray sources. More details about this technique are given in section 4.3.3. The main components of the BAT instrument are
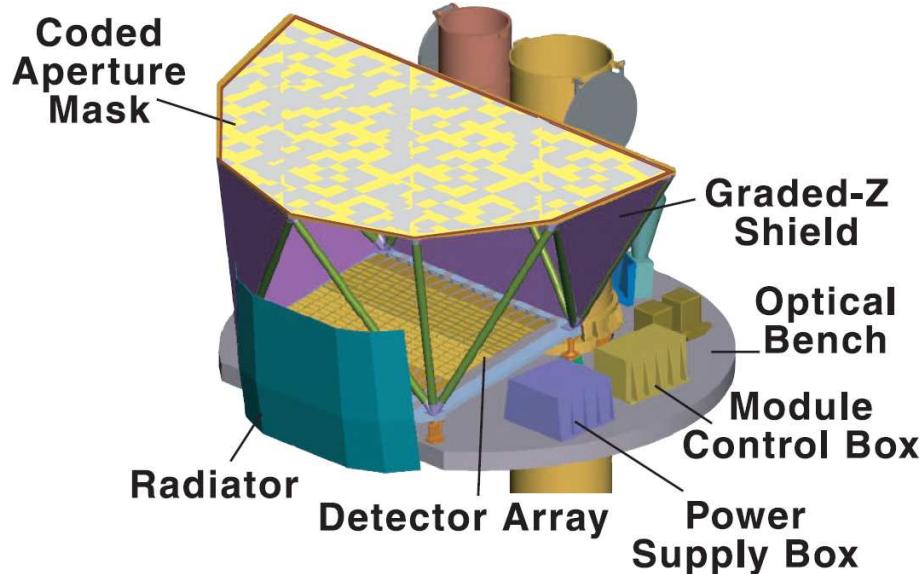
Figure 4.2 BAT cutaway drawing showing the D-shaped coded mask, the CZT array, and the graded-Z shielding. The mask pattern is not to scale.

shown in Figure 4.2. The detector array sits 1-m behind the coded aperture mask. The D-shaped $2.7\,\mathrm{m}^2$ coded-aperture mask is built using a random pattern of $5 \times 5 \times 1\,\mathrm{mm}^3$ lead tiles with 50% of the mask open. The BAT instrument is surrounded by a radiation shield to protect it from any stray radiation.

4.3.2 CdZnTe Detector Plane

The BAT instrument consists of a detector plane of 32,768 CdZnTe (CZT) detector elements. These $4 \times 4\,\mathrm{mm}^2$ elements are arranged into 8×16 arrays and two of these arrays are collectively called a Detector Module (DM). Eight DMs are assembled in a structure called a Block. Sixteen blocks are integrated to form the full BAT detector array. This ar-

rangement of 32K pixels or elements into 128 DMs and 16 Blocks, each with its own power supply, electronics, control parameters, and communication channels, gives parallelism and redundancy against failures.
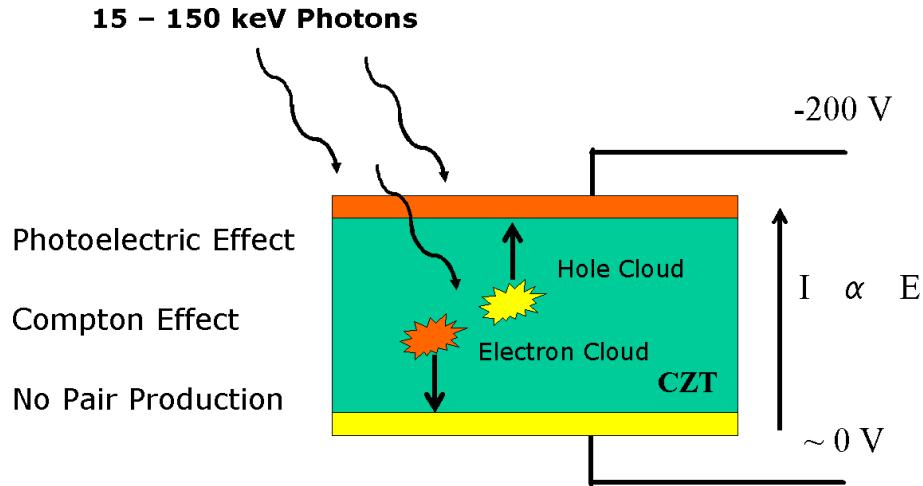
Figure 4.3 CZT Detector Element

An incident beam of photons can create moving electrons through three processes; 1) Photoelectric effect, 2) Compton effect and 3) Pair production. With photons in the energy range of $15 - 350$ keV, pair production is not possible (pair production needs photons with energy greater than 1.022 MeV). In the CdZnTe elements, incident photons will create electron and hole clouds through the photoelectric effect and Compton effect (see Figure 4.3). The hole cloud will travel towards the negative electrode (cathode) and the electron cloud will move toward the positive electrode (anode) which will result in a small electric current that will be read by electronic circuits as a detection. The strength of the current is a measure of the energy of the incident photon that created the electron and hole cloud.

4.3.3   Coded Aperture Mask Technique

BAT uses a coded aperture mask to localize bursts. The basic imaging scheme is that a gamma-ray source illuminates the coded aperture mask, and casts a shadow onto a position sensitive detector as shown in Figure 4.4. Each position in the sky will produce a unique shadow pattern in the detector plane. Hence by comparing the observed shadow, with pre-calculated shadow patterns for all possible points in the sky we should be able to find the

actual position of the source that created the given shadow pattern. However, in practice each detector can be illuminated by many points on the sky and each point on the sky can illuminate many detectors. To disentangle each point in the sky, special software designed by the $Swift$ BAT team needs to be used.
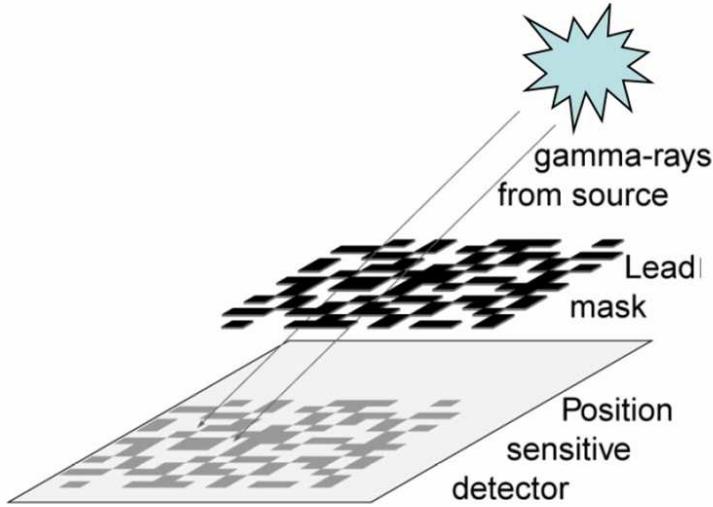
Figure 4.4 A gamma-ray source illuminates the coded aperture mask and creates a unique pattern in the detector.

The BAT has two spaces known as detector space and sky space. The BAT software reconstructs the sky image from the detector plane image (DPI), which is derived from the raw data. DPI is a 286×173 counts map giving the detected BAT counts in each detector. The BAT software cross-correlates the detected counts in the DPI with a mask aperture shadow pattern corresponding to a particular sky location. These shadow patterns are obtained by ray-tracing all possible locations on the sky onto the detector plane. In the shadow pattern fully illuminated detectors are assigned a weight of +1, partially illuminated detectors are assigned a weight of zero and fully blocked detectors are assigned -1. For each location in the sky, a corresponding weighted shadow pattern is multiplied by the detected counts and the result is summed together. If a source was present at a given location in the sky, its corresponding shadow pattern will show an excess of counts in places where the mask is open. The multiplying and summing procedure produces an enhanced correlation at the location of the source. For locations where there were no sources, the mask shadow pattern is uncorrelated with detector counts and the multiplying and summing procedure does not

produce enhanced correlations. The final result of this exercise is a background-subtracted mask-weighted flux for each position in the sky.

One of the major advantages of the coded aperture detector is that a bad pixel in the detector plane will only result in a slight loss of sensitivity. The overall sky image will not be effected in a significant way. In focusing telescopes a bad pixel in the detector array will result in a missing pixel in the sky image and loss of information.

4.3.4 Partial Coding

Parts of the sky that can illuminate the BAT detector determines its field of view (FOV). A number of factors need to be considered in calculating the FOV, such as dimensions of the mask, spatial position of the detector array and information about enabled and disabled detectors. Partial coding is a term that is used to characterize the fraction of the detector that is illuminated by the aperture shadow. If a source is on axis and its aperture shadow fully illuminates the detector array then the BAT is fully coded or 100% coded. There is a small region near BAT's FOV which is fully coded. When a source moves off axis, its shadow partially illuminates the detector array. This partial illumination is called the partial coding fraction. Variation of the partial coding fraction throughout the BAT FOV is shown in Figure 4.5. Note that as the partial coding decreases, the instruments sensitivity also decreases. This is the reason, when a burst is detected off axis, that the light curve is noisier at the beginning and gets better when $Swift$ slews to the source. The BAT analysis software automatically corrects for partial coding effects.
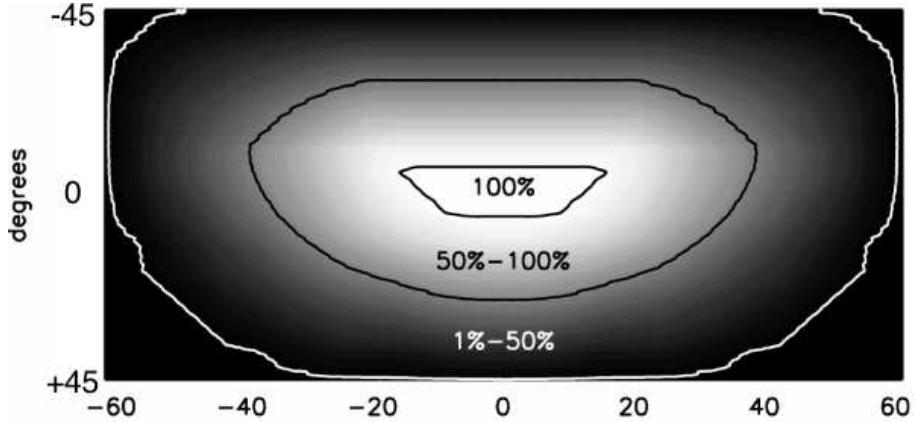
Figure 4.5 BAT partial coding map in sky coordinates (in degrees in both axes), assuming all detectors are enabled.

4.3.5 Burst Detection and Triggering Algorithm

GRB detection in BAT is a two step process. First, BAT looks for increases in the count rate in the detector plane. Triggering algorithms are used for this purpose. Secondly, BAT creates an image of the sky using the detected events during the trigger time interval and compares it with an on-board catalog for known sources. This last step essentially is a confirmation procedure called burst imaging.

The triggering algorithms used in BAT are based on triggering algorithms developed for High Energy Transient Explorer 2 (HETE-2). The algorithm utilizes a large number of criteria based on parameters such as pre-burst background intervals, the duration of the burst interval (ranging from 4 msec to 32 sec), the region of the detector plane illuminated, and energy band passes. These procedures, which look for sudden increase in rate, are called rate triggers. A second type of triggering process called image trigger is also implemented in BAT. This process collects detector array count rate maps very 64 seconds and creates a sky image. Then it scans for point sources and all sources found are compared against an on-board catalog, which can be modified from the ground. If any new sources are found then it reports its location to the ground as a new burst.

The burst imaging and locating process of BAT reduces false triggers significantly. This second step is the primary advantage of BAT. This process enables BAT to trigger on low

trigger threshold levels and increase its sensitivity to weak bursts.

4.3.6 BAT Operating Modes

BAT operates in two modes. The first mode is called the burst mode, which produces burst positions. The second mode is called the survey mode, which produces data for a hard X-ray survey[1]. In this second mode, BAT collects count rate data in 5 min time intervals for 18 energy intervals. Normally, BAT sits on this survey mode, but when a burst is detected it switches to the burst mode and starts collecting photon-by-photon data. It is also equipped with a round-robin buffer to save pre-burst information. The saving of pre-burst information facilitates studies of burst precursors.

4.4 BAT Data Analysis

4.4.1 BAT Data Types

We receive burst data from $Swift$ in two ways. Initially, TDRSS[2] data comes down within seconds after the burst though the TDRSS network. TDRSS is a network of VHF (Very High Frequency) receivers distributed along the Earth's equator to facilitate quick real time communication with satellites. TDRSS data is used to measure the basic properties of the burst. The TDRSS light curve data cover a time from 24 seconds before to 185 seconds after the burst. They have four energy channels. These four channels corresponds to 15-25, 25-50, 50-100 and 100-350 keV. The time binning varies and is most dense (0.128 seconds) close to the trigger time and least dense (4.096 seconds) well after the trigger.

The event-by-event data comes through the Malindi station a few hours after the burst trigger. The time gap between the GRB and the arrival time of event-by-event data can be a few hours. The event data allows the maximum flexibility in terms of selecting a time interval, time and energy resolution. The raw event-by-event data includes all events from cosmic ray events, noisy detectors, and events from other sources in the FOV. We need to use coded mask analysis in order to remove these unwanted spurious events. In the next section we will describe how the mask weighting is used to clean the data.

---

[1]While searching for GRBs, BAT performs an all-sky hard X-ray survey, looking for hard X-ray transients.
[2]Tracking and Data Relay Satellite System

4.4.2   Light Curve Extraction

In order to generate light curves, a process called mask weighting is utilized. The mask weighting assigns a ray-traced shadow value for each individual event, which then enables the user to calculate light curves or spectra. We used the `batmaskwtevt` and `batbinevt` tasks in FTOOLS to generate mask weighted, background-subtracted light curves for our analysis. Resulting light curves and their uncertainties are calculated by propagation of errors from raw counts (subject to Poissonian noise)[3].

BAT light curves can be time binned down to $\sim$ 0.1 ms. However, 0.1 ms time bin size is not suitable for all types of timing analyses. For various types of analyses in this thesis we used a number of different time binnings. The detailed reasons for selecting a particular time bin size for a given type of analysis are given in the later chapters.

---

[3]Details of basic $Swift$ data analysis is available at `http://swift.gsfc.nasa.gov/docs/swift/analysis/`

Chapter 5

Spectral Lag Analysis of GRBs

5.1 Introduction

The spectral lag is the difference in time of arrival of pulses at different energies and is considered to be positive when the high-energy photons arrive earlier than the low energy ones. There are at least three well known ways of extracting spectral lags; (1) pulse peak-fit method (Norris et al., 2005; Hakkila et al., 2008), (2) Fourier analysis method (Li et al., 2004), and (3) cross-correlation function (CCF) analysis method (Cheng et al., 1995; Band, 1997).

The pulse peak-fit method gives a simple straightforward way for extracting lags. The basic scheme is to identify a prominent pulse in the light curve and fit it with a certain pulse model. This fitting is performed for two light curves in two separate energy bands. Then the lag is given by the time offset of the two peaks. This method is, however, limited to very bright bursts with prominent peaks that can be fitted by a particular pulse function. It is not immediately clear how this method would fare in cases where the light curves are sufficiently complex i.e., not dominated by a prominent pulse.

For transient events such as GRBs, using the Fourier analysis technique also has its difficulties (Li et al., 2004). Since GRB light curves do not exhibit obvious periodicities, Fourier transforms typically yield a large number of coefficients to describe their temporal structure. These coefficients, in turn, produce a spectral lag value for each corresponding frequency component i.e., a spectrum of lags is generated. The generated spectra exhibit a variety of shapes depending on the complexity of the light curve (Li et al., 2004) thus making the extraction of an intrinsic lag questionable.

Due to the shortcomings of these methods, in this work we develop a method to calculate the time-averaged spectral lag and its uncertainty via a modification of the CCF method.

5.2 Cross Correlation Function (CCF)

The use of the Pearson cross-correlation function is a standard method for estimating the degree to which two series are correlated. For two counting series x_i and y_i where $i = 0, 1, 2, ...(N-1)$, the CCF with a delay d is defined as

$$CCF_{\text{Std}}(d, x, y) = \frac{\sum_{i=1}^{N-d}(x_i - \bar{x})(y_{i+d} - \bar{y})}{\sqrt{\sum_i(x_i - \bar{x})^2}\sqrt{\sum_i(y_i - \bar{y})^2}}. \tag{5.1}$$

Here $\bar{x}$ and $\bar{y}$ are average counts of the two series x and y respectively. The denominator in the expression above serves to normalize the correlation coefficient so that $-1 \leq CCF_{\text{Std}}(d, x, y) \leq 1$, the bounds indicating maximum correlation and zero indicating no correlation. A high negative correlation indicates a high correlation but of the inverse of one of the series. Note that the time delay (τ) is given by $\tau = d \times$ time bin size.

However, Band (1997) proposed that for transient events such as GRBs, the non-mean subtracted definition given below is more suitable for the time-averaged lag.

$$CCF_{\text{Band}}(d, x, y) = \frac{\sum_{i=\max(1, 1-d)}^{\min(N, N-d)} x_i\, y_{i+d}}{\sqrt{\sum_i x_i^2\, \sum_i y_i^2}} \tag{5.2}$$

We have tested both definitions of the CCF using synthetic light curves with artificially introduced spectral lags (see Appendix C for more details). Our tests showed that the CCF_{Band} consistently recovered the introduced lag while CCF_{Std} sometimes failed (possible reasons for this failure are noted in Band (1997)). Hence in our analysis we used the CCF_{Band} definition and from this point onward we refer to it simply as the CCF.

For a given pair of real light curves, we determine the CCF using Equation 5.2. At this stage the resulting CCF values do not have any uncertainties associated with them. In order to determine these uncertainties, we use a Monte Carlo simulation. Here we make 1,000 Monte Carlo realizations of the real light curve-pair based on their error bars as shown below:

$$\text{LC}_{\text{bin}}^{\text{simulated}} = \text{LC}_{\text{bin}}^{\text{real}} + \xi \times \text{LC}_{\text{bin}}^{\text{real error}}, \tag{5.3}$$

where ξ is a random number generated from a Gaussian distribution with the mean equal to zero and the standard deviation equal to one. For each simulated light curve-pair we calculate the CCF value for a series of time delays. This results in 1,000 CCF values per time-delay bin. The standard deviation of these values per time-delay bin is then assigned as the uncertainty in the original CCF values obtained from the real light curves.

5.3 Extracting Spectral Lags

There may be a number of ways to define the spectral lag, but in this work we define it as the time delay corresponding to the global maximum of the cross-correlation function. To locate this global maximum, we fit a Gaussian curve to the CCF. The uncertainties in the CCF are obtained using a Monte Carlo procedure discussed in section 5.2. In essence, our fitting procedure locates the centroid of the cross correlation function and is thus relatively insensitive to spurious spikes in the CCF. We tested and verified the robustness of this procedure by performing a number of simulations in which artificial lags were first introduced into the light curves and then successfully recovered. In addition, our tests with these artificial light curves show that the CCF can become asymmetric (around its global maximum) if the shape of one of the light curves is significantly different from the other. This energy dependent feature potentially requires a more complex fitting function than a Gaussian or a quadratic to fit the CCF over the entire range. Instead of resorting to a more complex fitting function we were able to recover the (known) lags by fitting the CCFs (with a Gaussian) over limited but asymmetric ranges.

5.3.1 Time Bin Selection

For $Swift$ GRBs the minimum time binning is 0.1 ms but one can arbitrarily increase this all the way up to the duration of the burst. It is important to understand the effect of time binning on the extracted spectral lags. Presumably, by changing the time binning of the light curve one is affecting the signal-to-noise ratio. By employing increasingly coarser binning one is averaging over the high frequency components of the light curve. Clearly, one has to be careful not to use overly large time bin sizes otherwise one risks losing the sought-after information from the light curve.

In order to understand the effect of time binning more fully, we did a number of simula-
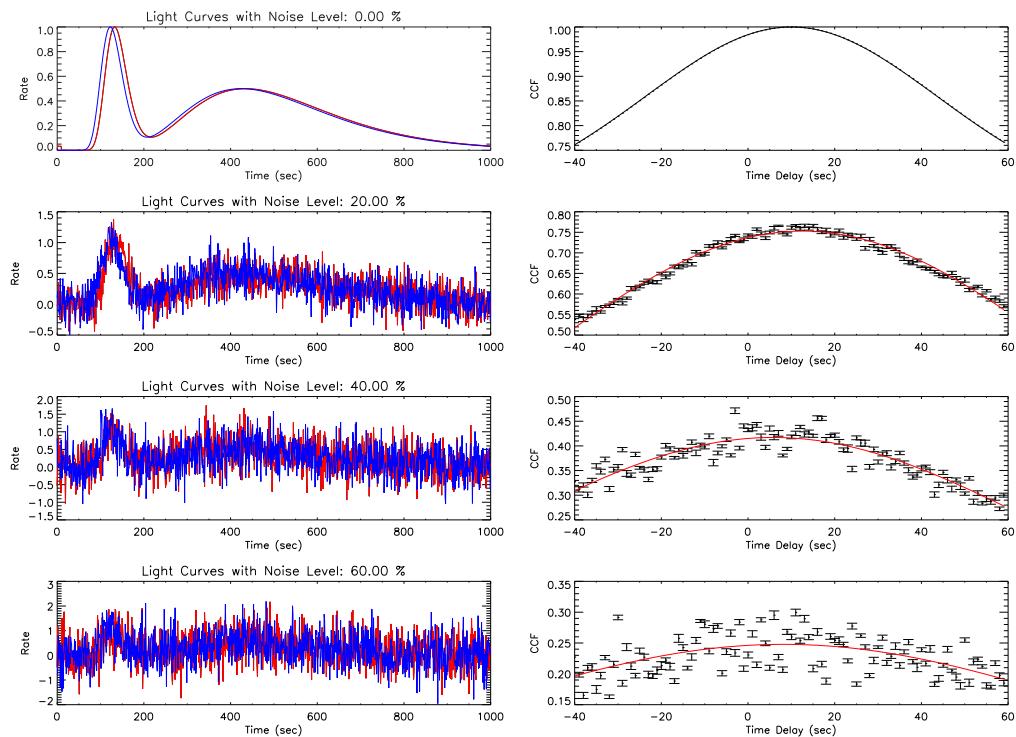
Figure 5.1 The effect of noise on the CCF. Panels on the left show two synthetic light curves, in which a 10-second artificial lag is added. From top to bottom the noise level is increased to 0%, 20%, 40% and 60% respectively. The corresponding CCF vs time delay plots are shown in the right panels along with Gaussian fits.
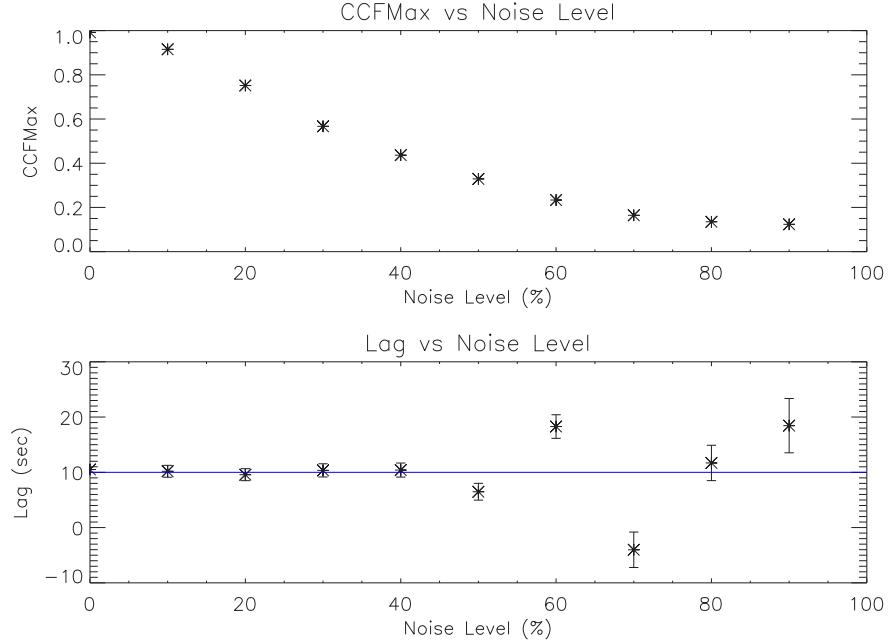
Figure 5.2 The effect of noise on the maximum correlation of the CCF (CCFMax) and the extracted spectral lag. The horizontal line (blue) in the bottom panel indicates the 10-second artificial lag.

tions utilizing peak normalized synthetic light curves (composed of FRED[1]-like pulse shapes with Gaussian distributed noise) in which artificial lags were introduced. We incrementally increased the noise level and studied its effect on the maximum correlation value in the CCF vs time delay (CCFMax) plot. In Figure 5.1 we display the synthetic light curves with several noise levels (0%, 20%, 40% and 60% respectively) as well as the calculated CCF with typical Gaussian fits. As expected, the CCFMax value (see the right panel of Figure 5.1) decreases gradually as the noise level increases. We also note that the scatter in the CCF increases considerably with the noise level. The global maximum in the CCF is clearly visible at the 40% noise level and a good fit is obtained with a Gaussian. However, this is not the case for the 60% noise-level curve, in which the scatter is quite significant, and the CCF global maximum is barely visible leading to a poor fit.

In Figure 5.2 we show the behavior of the CCFMax value and the extracted spectral lag as a function of the noise level. We first note that the CCFMax value smoothly tracks the signal-to-noise level in the light curves (see the upper panel of Figure 5.2). Secondly, we note that the extracted lag value agrees well with the artificially introduced lag of 10 seconds up to a noise level of about 40%. We further note that the scatter in the extracted lag value

---

[1]Fast Rise Exponential Decay

increases as the noise contribution increases beyond 40%. Although it is not immediately obvious from this figure, CCF values above a noise level of 40% show large scatter (see the bottom right panel of Figure 5.1) thus making the extracted lag value uncertain. This is directly reflected in the increasing error bars in the extracted value. These simulations were repeated for a number of time lags and in all cases similar results were obtained; in particular, the behavior of the CCFMax as a function of the noise level was confirmed. Based on the results of these simulations, we chose a CCFMax ~ 0.5, corresponding to a noise level of about 40%, as our guide for picking the appropriate time binning.

Procedurally, we start with a time bin size of 1024 ms and decrease the time binning by powers of two until the CCFMax becomes ~ 0.5 and use that time bin size as the preferred time binning for the lag extraction. By using this procedure we are able to arrive at a reasonable bin size that preserves the fine structure in the light curve and at the same time keeps the contribution of the noise component at a manageable level.

5.3.2   Uncertainty in Spectral Lags

We have studied three methods to determine the uncertainty in the extracted spectral lags. The first method is to use the uncertainty that is obtained by fitting the CCF with a Gaussian curve. The second method is an adaptation of equation (4) used in Gaskell and Peterson (1987)

$$\sigma_{\text{lag}} = \frac{0.75\, W_{\text{HWHM}}}{1 + h\sqrt{n-2}}.$$

(5.4)

Here W_{HWHM} is the half-width at half-maximum of the fitted Gaussian, h the maximum height of the Gaussian and n is the number of bins in the CCF vs time delay plot. This method utilizes more information about the fit and the CCF such as the width, height, and number of bins to estimate the uncertainty. The third method utilizes a Monte Carlo simulation. We found that the first method gives systematically smaller uncertainty in the lag by a factor of two or more relative to the other two methods. The second and third methods give comparable values. We adopted the most conservative of the three methods (i.e. the one based on the Monte Carlo simulation) to determine the uncertainties in the lag.
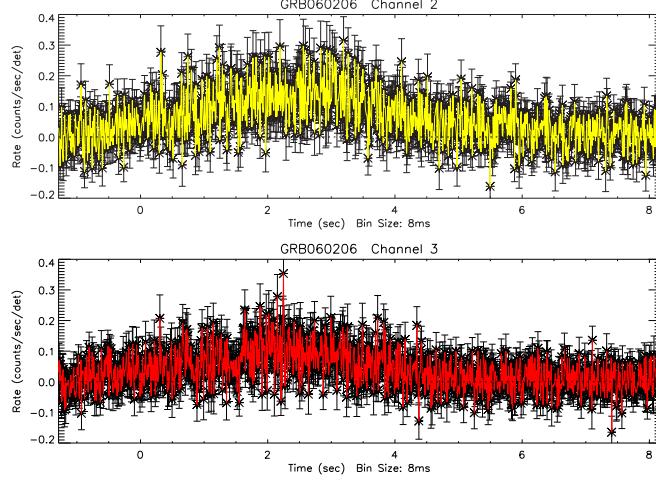
Figure 5.3 Swift-BAT prompt gamma-ray (8 ms time bin) light curves for GRB 060206 with canonical energy channels 2 (25-50 keV) and 3 (50-100 keV).

5.4 Lag Extraction: Case Study

To illustrate the lag extraction procedure more clearly, we present a case study using GRB 060206. The light curve segment is selected by scanning both forward and backward directions from the peak location until the count rate drops to less than 5% of the peak count rate (using $15 - 200$ keV light curve). This selection method is chosen to include the most intense segment of the burst and to capture any additional overlapping pulses near the main structure. Presumably, these pulses also contribute to the overall spectral lag. In the case of GRB 060206 this corresponds to a light curve segment starting 1.29 seconds prior to the trigger and 8.18 seconds after the trigger (see Figure 5.3).

Next we calculate the CCF and plot it as a function of time delay as shown Figure 5.4. Error bars on the CCF points were obtained via a Monte Carlo simulation of 1,000 realizations of the original light curves (see section 5.2). As noted earlier, we start with a time bin size of 1024 ms and decrease the time binning by powers of two until the CCFMax becomes ~ 0.5 for a given channel combination, in this case BAT standard channel 2 ($25 - 50$ keV) and 3 ($50 - 100$ keV). For GRB060206 channels 2 and 3, the time bin size corresponds to 8 ms. The global maximum of the CCF vs time delay plot corresponds to the spectral lag and its value is obtained by fitting a Gaussian curve. We choose a range of the time delay (in this case from -1.5 seconds to 1.5 seconds) manually to identify the global maximum. In order to obtain the uncertainty in the spectral lag, we employ another Monte Carlo simulation, in which we create 1,000 additional realizations of the input light curves as described
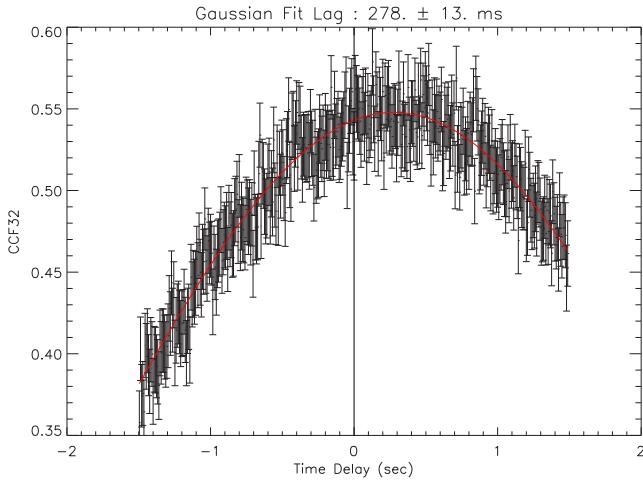
Figure 5.4 CCF as a function of time delay for the two light curves in Figure 5.3. The time delay corresponding to the peak of the Gaussian fit is the spectral lag of the burst, which is 278 ± 13 ms. The uncertainty quoted here is from the fit, which tends to be factor of two or more less than the value obtained by the Monte Carlo simulation shown in Figure 5.5.
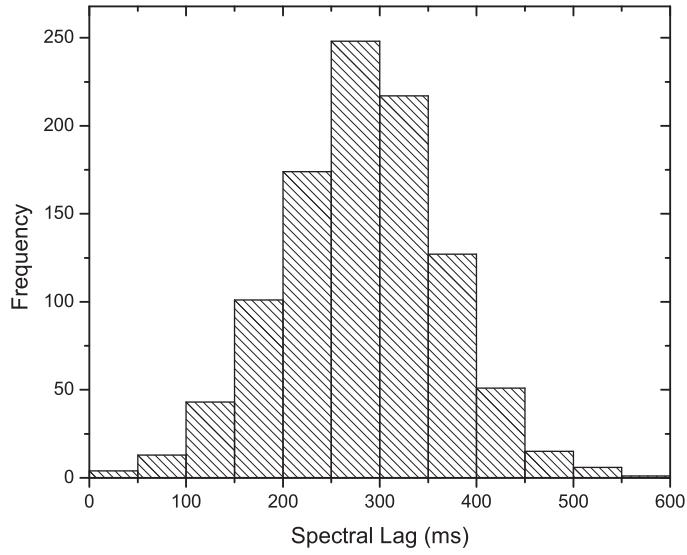
Figure 5.5 Histogram of 1,000 simulated spectral lag values. We take the standard deviation of the distribution of simulated spectral lag values as the uncertainty of the fitted spectral lag value which was found in Figure 5.4. The final spectral lag value is 278 ± 74 ms.

in section 5.2, and repeat the previously described process for the simulated light curves. A histogram of the resulting (1,000) spectral lag values is shown in Figure 5.5 for GRB 060206. The standard deviation of these values is the uncertainty in the spectral lag.

5.5 Lag-Luminosity Relation (Observer Frame)

5.5.1 Sample Selection and L_{iso} Calculation

We selected a sample of long GRBs ($T90 > 2$ sec, excluding short bursts with extended emission), detected by $Swift$ BAT from 2004 December 19 to 2009 July 19, for which spectroscopically confirmed redshifts were available. Out of this initial sample (102), a subset of 41 GRBs were selected with peak rate > 0.3 counts/sec/det ($15 - 200$ keV, 256 ms time resolution). Finally, we selected 31 GRBs for which a clear global maximum can be seen in the CCF vs time delay plots with maximum correlation of at least 0.5 (with 256 ms time binning) for all channel combinations. The spectral parameters of the final sample are given in Table 5.1. We note that our final sample contains bursts with redshifts ranging from 0.346 (GRB 061021) to 5.464 (GRB 060927) and the average redshift of the sample is ~ 2.0.

Out of our sample, 18 bursts have all Band spectral parameters measured and comprise our "Gold" sample. The remaining 13 bursts are further divided into "Silver" and "Bronze" samples. In the "Silver" sample, 10 bursts have E_{p} determined by fitting a cutoff power-law[2] (CPL) to spectra and for GRB 060418, E_{p} is reported without uncertainty, so we assumed a value of 10%. These 10 bursts do not have the high-energy spectral index, β, measured, so we used the mean value of the BATSE β distribution, which is -2.36 ± 0.31 (Kaneko et al., 2006; Sakamoto et al., 2009). The "Bronze" sample (consisting of 3 bursts) does not have a measured E_{p}. We have estimated it using the power-law index (Γ) of a simple power-law (PL) fit as described in Sakamoto et al. (2009). For these 3 bursts, the low-energy spectral index, α and the high-energy spectral index, β, were not known, so we used the mean value of the BATSE α and β distribution, which is -0.87 ± 0.33 and -2.36 ± 0.31 respectively (Kaneko et al., 2006; Sakamoto et al., 2009). All estimated spectral parameters are given in square brackets in Table 5.1.

Using the spectral parameters and redshift information in Table 5.1 we have calculated

---

[2] $dN/dE \sim E^{\alpha} \exp\left(-(2+\alpha)E/E_{\mathrm{p}}\right)$

the peak isotropic luminosities (L_{iso}) for all the bursts in our sample (see Appendix B): these results are shown in Table 5.2. GRB 080430 has the lowest luminosity in the sample ($\sim 1.03 \times 10^{51} \, \mathrm{erg \, s^{-1}}$), and GRB 080607 has the highest luminosity ($\sim 7.19 \times 10^{53} \, \mathrm{erg \, s^{-1}}$). The sample spans roughly three orders of magnitude in luminosity.

5.5.2 Spectral Lag vs. Isotropic Peak Luminosity

We extracted the spectral lags for all combinations of the canonical BAT energy bands: channel 1 (15–25 keV), 2 (25–50 keV), 3 (50–100 keV) and 4 (100–200 keV). We took the upper-boundary of channel 4 to be 200 keV because we found that after the mask weighting the contribution to the light curve from energies greater than $\sim$200 keV is negligible. The nomenclature is straightforward, i.e., the spectral lag between energy channels 4 and 1 is represented by Lag 41. As such there are six channel combinations and the results for all six are shown in Table 5.7. The segment of the light curve used for the lag extraction ($T + X_{\mathrm{S}}$ and $T + X_{\mathrm{E}}$, T is the trigger time), the time binning of the light curve, and the Gaussian curve fitting range of the CCF vs time delay plot (with start time, and end time denoted by LS and LE respectively) are also given in Table 5.7.

Table 5.1.   GRB redshift and spectral information

GRB	z	Peak Flux [a]	E_p [b]	α [c]	β [d]	Reference
GRB050401	2.899[1]	10.70 ± 0.58	119^{+16}_{-16}	$0.83^{+0.13}_{-0.13}$	$2.37^{+0.09}_{-0.09}$	Golenetskii et al. (2005a); Sakamoto et al. (2008a)
GRB050603	2.821[2]	21.50 ± 0.67	349^{+18}_{-18}	$0.79^{+0.04}_{-0.04}$	$2.15^{+0.06}_{-0.06}$	Golenetskii et al. (2005b); Sakamoto et al. (2008a)
GRB050922C	2.199[3]	7.26 ± 0.20	$[133^{+468}_{-39}]$	$[0.87^{+0.33}_{-0.33}]$	$[2.36^{+0.31}_{-0.31}]$	Sakamoto et al. (2008a)
GRB051111	1.550[4]	2.66 ± 0.13	447^{+206}_{-175}	$1.22^{+0.09}_{-0.09}$	$2.10^{+0.27}_{-4.94}$	Krimm et al. (2009a); Sakamoto et al. (2008a)
GRB060206	4.056[5]	2.79 ± 0.11	75^{+12}_{-12}	$1.06^{+0.21}_{-0.21}$	$[2.36^{+0.31}_{-0.31}]$	Palmer et al. (2006); Sakamoto et al. (2008a)
GRB060210	3.913[6]	2.72 ± 0.18	207^{+66}_{-47}	$1.18^{+0.11}_{-0.11}$	$[2.36^{+0.31}_{-0.31}]$	Krimm et al. (2009a); Sakamoto et al. (2008a)
GRB060418	1.490[7]	6.52 ± 0.22	230^{+23}_{-23}	$1.50^{+0.09}_{-0.09}$	$[2.36^{+0.31}_{-0.31}]$	Golenetskii et al. (2006d); Sakamoto et al. (2008a)
GRB060904B	0.703[8]	2.44 ± 0.13	103^{+59}_{-26}	$0.61^{+0.42}_{-0.42}$	$1.78^{+0.16}_{-0.23}$	Krimm et al. (2009a); Sakamoto et al. (2008a)
GRB060908	1.884[9]	3.03 ± 0.16	124^{+48}_{-24}	$0.89^{+0.20}_{-0.20}$	$2.24^{+0.34}_{-4.85}$	Krimm et al. (2009a); Sakamoto et al. (2008a)
GRB060927	5.464[10]	2.70 ± 0.11	72^{+16}_{-7}	$0.90^{+0.25}_{-0.25}$	$[2.36^{+0.31}_{-0.31}]$	Sakamoto et al. (2008a)
GRB061007	1.262[11]	14.60 ± 0.23	498^{+34}_{-30}	$0.53^{+0.06}_{-0.05}$	$2.61^{+0.16}_{-0.31}$	Golenetskii et al. (2006b); Sakamoto et al. (2008a)
GRB061021	0.346[12]	6.11 ± 0.17	777^{+343}_{-148}	$1.22^{+0.08}_{-0.09}$	$[2.36^{+0.31}_{-0.31}]$	Golenetskii et al. (2006c); Sakamoto et al. (2008a)
GRB061121	1.315[13]	21.10 ± 0.29	606^{+56}_{-45}	$1.32^{+0.02}_{-0.03}$	$[2.36^{+0.31}_{-0.31}]$	Golenetskii et al. (2006a); Sakamoto et al. (2008a)
GRB070306	1.496[14]	4.07 ± 0.13	$[76^{+131}_{-52}]$	$[0.87^{+0.33}_{-0.33}]$	$[2.36^{+0.31}_{-0.31}]$	Sakamoto et al. (2008a)
GRB071010B	0.947[15]	7.70 ± 0.19	52^{+6}_{-9}	$1.25^{+0.46}_{-0.31}$	$2.65^{+0.18}_{-0.31}$	Golenetskii et al. (2007a); Markwardt et al. (2007)
GRB071020	2.145[16]	8.40 ± 0.19	322^{+50}_{-33}	$0.65^{+0.17}_{-0.20}$	$[2.36^{+0.31}_{-0.31}]$	Golenetskii et al. (2007b); Holland et al. (2007)
GRB080319B	0.937[17]	24.80 ± 0.31	651^{+8}_{-9}	$0.82^{+0.01}_{-0.01}$	$3.87^{+0.28}_{-0.68}$	Golenetskii et al. (2008a); Racusin et al. (2008)
GRB080319C	1.949[18]	5.20 ± 0.19	307^{+88}_{-58}	$1.01^{+0.08}_{-0.08}$	$1.87^{+0.09}_{-0.39}$	Golenetskii et al. (2008b); Stamatikos et al. (2008)
GRB080411	1.030[19]	43.20 ± 0.56	259^{+22}_{-17}	$1.51^{+0.02}_{-0.03}$	$[2.36^{+0.31}_{-0.31}]$	Golenetskii et al. (2008c); Sato et al. (2008)
GRB080413A	2.433[20]	5.60 ± 0.13	126^{+82}_{-26}	$1.15^{+0.18}_{-0.18}$	$2.12^{+0.21}_{-4.93}$	Krimm et al. (2009a); Marshall et al. (2008a)
GRB080413B	1.101[21]	18.70 ± 0.04	67^{+8}_{-5}	$1.24^{+0.16}_{-0.16}$	$2.77^{+0.14}_{-0.17}$	Krimm et al. (2009a); Barthelmy et al. (2008)
GRB080430	0.767[22]	2.60 ± 0.13	$[67^{+85}_{-51}]$	$[0.87^{+0.33}_{-0.33}]$	$[2.36^{+0.31}_{-0.31}]$	Guidorzi et al. (2008)
GRB080603B	2.689[23]	3.50 ± 0.13	71^{+10}_{-10}	$1.21^{+0.19}_{-0.19}$	$[2.36^{+0.31}_{-0.31}]$	Mangano et al. (2008b)
GRB080605	1.640[24]	19.90 ± 0.38	297^{+29}_{-25}	$0.87^{+0.08}_{-0.08}$	$2.58^{+0.19}_{-0.53}$	Golenetskii et al. (2008d); Sbarufatti et al. (2008)
GRB080607	3.036[25]	23.10 ± 0.69	348^{+17}_{-17}	$0.76^{+0.04}_{-0.04}$	$2.57^{+0.11}_{-0.16}$	Golenetskii et al. (2008e); Mangano et al. (2008a)
GRB080721	2.591[26]	20.90 ± 1.13	485^{+42}_{-37}	$0.93^{+0.07}_{-0.05}$	$2.43^{+0.15}_{-0.26}$	Golenetskii et al. (2008f); Marshall et al. (2008b)
GRB080916A	0.689[27]	2.70 ± 0.13	121^{+50}_{-16}	$0.95^{+0.16}_{-0.16}$	$2.15^{+0.17}_{-0.31}$	Krimm et al. (2009a); Ziaeepour et al. (2008)
GRB081222	2.770[28]	7.70 ± 0.13	134^{+6}_{-6}	$0.55^{+0.04}_{-0.04}$	$2.10^{+0.04}_{-0.04}$	Bissaldi and McBreen (2008); Grupe et al. (2009)
GRB090424	0.544[29]	71.00 ± 1.25	177^{+2}_{-2}	$0.90^{+0.01}_{-0.01}$	$2.90^{+0.06}_{-0.06}$	Connaughton (2009); Cannizzo et al. (2009)
GRB090618	0.540[30]	38.80 ± 0.50	156^{+7}_{-7}	$1.26^{+0.04}_{-0.01}$	$2.50^{+0.09}_{-0.21}$	McBreen (2009); Schady et al. (2009)
GRB090715B	3.000[31]	3.80 ± 0.13	178^{+21}_{-14}	$0.86^{+0.14}_{-0.13}$	$[2.36^{+0.31}_{-0.31}]$	Golenetskii et al. (2009); Vetere et al. (2009)

References. — (1) Watson et al. (2006); (2) Berger and Becker (2005); (3) Piranomonte et al. (2008); (4) Penprase et al. (2006); (5) Fynbo et al. (2009); (6) Fynbo et al. (2009); (7) Prochaska et al. (2006); (8) Fynbo et al. (2009); (9) Fynbo et al. (2009); (10) Fynbo et al. (2009); (11) Fynbo et al. (2009); (12) Fynbo et al. (2009); (13) Fynbo et al. (2009); (14) Jaunsen et al. (2008); (15) Cenko et al. (2007); (16) Jakobsson et al. (2007); (17) D'Elia et al. (2009); (18) Fynbo et al. (2009); (19) Fynbo et al. (2009); (20) Fynbo et al. (2009); (21) Fynbo et al. (2009); (22) Cucchiara and Fox (2008); (23) Fynbo et al. (2009); (24) Fynbo et al. (2009); (25) Prochaska et al. (2009); (26) Fynbo et al. (2009); (27) Fynbo et al. (2009); (28) Cucchiara et al. (2008); (29) Chornock et al. (2009); (30) Cenko et al. (2009); (31) Wiersema et al. (2009).

[a] 1-second peak photon flux measured in photon $\mathrm{cm}^{-2}\,\mathrm{s}^{-1}$ in the energy range $15 - 150$ keV.

[b] Peak energy is given in keV. Values in brackets indicates estimated values using the method described in Sakamoto et al. (2009).

[c] Values in brackets indicates estimated high-energy photon index, α, which is the mean value of the BATSE α distribution (Kaneko et al., 2006; Sakamoto et al., 2009).

[d] Values in brackets indicates estimated high-energy photon index, β, which is the mean value of the BATSE β distribution (Kaneko et al., 2006; Sakamoto et al., 2009).

Note. — Note that uncertainties of parameters that are reported with 90% confidence level have been reduced to 1σ level for consistency.

Table 5.2. GRB redshift and calculated isotropic peak luminosity

GRB	Redshift	Peak Isotropic Luminosity [a]	GRB	Redshift	Peak Isotropic Luminosity [a]
GRB050401	2.899	$(1.38^{+0.16}_{-0.13}) \times 10^{53}$	GRB080319B	0.937	$(6.96^{+0.32}_{-0.14}) \times 10^{52}$
GRB050603	2.821	$(6.32^{+0.47}_{-0.34}) \times 10^{53}$	GRB080319C	1.949	$(6.04^{+8.04}_{-0.42}) \times 10^{52}$
GRB050922C	2.199	$(5.17^{+28.00}_{-0.01}) \times 10^{52}$	GRB080411	1.030	$(5.49^{+1.11}_{-0.34}) \times 10^{52}$
GRB051111	1.550	$(1.55^{+0.61}_{-0.33}) \times 10^{52}$	GRB080413A	2.433	$(5.38^{+4.69}_{-0.83}) \times 10^{52}$
GRB060206	4.056	$(6.28^{+2.50}_{-0.62}) \times 10^{52}$	GRB080413B	1.101	$(1.51^{+0.15}_{-0.06}) \times 10^{52}$
GRB060210	3.913	$(8.53^{+2.75}_{-0.92}) \times 10^{52}$	GRB080430	0.767	$(1.03^{+1.30}_{-0.07}) \times 10^{51}$
GRB060418	1.490	$(1.96^{+0.43}_{-0.13}) \times 10^{52}$	GRB080603B	2.689	$(2.99^{+1.25}_{-0.30}) \times 10^{52}$
GRB060904B	0.703	$(2.18^{+3.59}_{-0.32}) \times 10^{51}$	GRB080605	1.640	$(1.15^{+0.56}_{-0.09}) \times 10^{53}$
GRB060908	1.884	$(1.54^{+22.50}_{-0.22}) \times 10^{52}$	GRB080607	3.036	$(7.19^{+0.64}_{-0.41}) \times 10^{53}$
GRB060927	5.464	$(1.17^{+0.43}_{-0.10}) \times 10^{53}$	GRB080721	2.591	$(5.18^{+0.83}_{-0.47}) \times 10^{53}$
GRB061007	1.262	$(1.01^{+0.20}_{-0.08}) \times 10^{53}$	GRB080916A	0.689	$(1.30^{+19.90}_{-0.15}) \times 10^{51}$
GRB061021	0.346	$(1.30^{+0.60}_{-0.13}) \times 10^{51}$	GRB081222	2.770	$(1.26^{+0.07}_{-0.06}) \times 10^{53}$
GRB061121	1.315	$(7.89^{+1.02}_{-0.47}) \times 10^{52}$	GRB090424	0.544	$(1.62^{+0.05}_{-0.04}) \times 10^{52}$
GRB070306	1.496	$(8.67^{+13.50}_{-0.27}) \times 10^{51}$	GRB090618	0.540	$(8.47^{+1.17}_{-0.34}) \times 10^{51}$
GRB071010B	0.947	$(4.24^{+1.72}_{-0.33}) \times 10^{51}$	GRB090715B	3.000	$(6.79^{+2.42}_{-0.71}) \times 10^{52}$
GRB071020	2.145	$(1.27^{+0.64}_{-0.15}) \times 10^{53}$			

[a]Isotropic equivalent peak photon luminosity in $\mathrm{erg\,s^{-1}}$ between GRB rest frame energy range 1 and 10,000 keV as described in Appendix B.

Table 5.3. Spectral lag values of long duration $Swift$ BAT GRBs

GRB	Trigger ID	LagXX	$T + X_S$ (s)	$T + X_E$ (s)	Bin Size (ms)	LS (s)	LE (s)	Lag Value (ms)
GRB050401	113120	Lag 21	23.03	29.43	32	-1.00	1.50	275 ± 131
		Lag 31	23.03	29.43	32	-1.00	2.00	504 ± 117
		Lag 41	23.03	29.43	64	-1.00	2.00	562 ± 140
		Lag 32	23.03	29.43	16	-1.00	1.00	136 ± 87
		Lag 42	23.03	29.43	64	-1.50	1.50	250 ± 112
		Lag 43	23.03	29.43	64	-2.00	2.00	106 ± 118
GRB050603	131560	Lag 21	-3.83	3.08	8	-0.40	0.40	46 ± 24
		Lag 31	-3.83	3.08	8	-0.40	0.40	59 ± 22
		Lag 41	-3.83	3.08	16	-0.40	0.40	86 ± 29
		Lag 32	-3.83	3.08	4	-0.20	0.20	4 ± 11
		Lag 42	-3.83	3.08	16	-0.40	0.40	34 ± 19
		Lag 43	-3.83	3.08	16	-0.50	0.50	20 ± 18
GRB050922C	156467	Lag 21	-2.70	2.94	8	-0.40	0.40	9 ± 35
		Lag 31	-2.70	2.94	8	-1.00	1.00	180 ± 50
		Lag 41	-2.70	2.94	16	-1.00	1.00	188 ± 78
		Lag 32	-2.70	2.94	4	-1.00	1.00	188 ± 39
		Lag 42	-2.70	2.94	16	-1.00	1.00	178 ± 70
		Lag 43	-2.70	2.94	16	-1.00	1.00	19 ± 72
GRB051111	163438	Lag 21	-6.96	28.62	32	-5.00	4.00	583 ± 273
		Lag 31	-6.96	28.62	32	-4.00	4.00	1383 ± 288
		Lag 41	-6.96	28.62	128	-4.00	8.00	2343 ± 397
		Lag 32	-6.96	28.62	16	-5.00	4.00	776 ± 200
		Lag 42	-6.96	28.62	64	-5.00	5.00	1486 ± 314
		Lag 43	-6.96	28.62	64	-5.00	5.00	866 ± 319
GRB060206	180455	Lag 21	-1.29	8.18	8	-1.50	1.50	241 ± 78
		Lag 31	-1.29	8.18	16	-1.00	2.00	517 ± 85
		Lag 41	-1.29	8.18	64	-1.50	2.00	331 ± 219
		Lag 32	-1.29	8.18	8	-1.50	1.50	278 ± 74
		Lag 42	-1.29	8.18	64	-1.50	1.50	82 ± 193
		Lag 43	-1.29	8.18	64	-2.00	2.00	-163 ± 189
GRB060210	180977	Lag 21	-3.37	5.08	64	-5.00	4.00	700 ± 270
		Lag 31	-3.37	5.08	64	-5.00	4.00	508 ± 254
		Lag 41	-3.37	5.08	256	-5.00	4.00	1038 ± 324
		Lag 32	-3.37	5.08	64	-4.00	4.00	-175 ± 174
		Lag 42	-3.37	5.08	128	-4.00	4.00	98 ± 225
		Lag 43	-3.37	5.08	256	-5.00	2.00	34 ± 195
GRB060418	205851	Lag 21	-7.66	33.04	16	-2.00	2.00	22 ± 62
		Lag 31	-7.66	33.04	32	-2.00	2.00	109 ± 62
		Lag 41	-7.66	33.04	128	-2.00	2.00	476 ± 196
		Lag 32	-7.66	33.04	16	-2.00	2.00	87 ± 50
		Lag 42	-7.66	33.04	64	-1.00	1.00	212 ± 100
		Lag 43	-7.66	33.04	64	-1.00	1.00	162 ± 101
GRB060904B	228006	Lag 21	-1.97	10.32	32	-2.00	2.00	412 ± 195
		Lag 31	-1.97	10.32	32	-2.00	2.00	560 ± 164
		Lag 41	-1.97	10.32	128	-3.00	3.00	602 ± 296
		Lag 32	-1.97	10.32	32	-2.00	2.00	247 ± 140
		Lag 42	-1.97	10.32	128	-2.50	3.00	175 ± 292
		Lag 43	-1.97	10.32	128	-3.00	3.00	32 ± 273

Table 5.3 (cont'd)

GRB	Trigger ID	LagXX	$T + X_S$ (s)	$T + X_E$ (s)	Bin Size (ms)	LS (s)	LE (s)	Lag Value (ms)
GRB060908	228581	Lag 21	-10.91	3.68	32	-2.00	2.00	118 ± 142
		Lag 31	-10.91	3.68	32	-2.00	2.00	346 ± 185
		Lag 41	-10.91	3.68	128	-4.00	4.00	367 ± 315
		Lag 32	-10.91	3.68	16	-2.00	2.00	124 ± 86
		Lag 42	-10.91	3.68	64	-2.00	2.00	233 ± 216
		Lag 43	-10.91	3.68	128	-4.00	4.00	134 ± 253
GRB060927	231362	Lag 21	-1.69	8.04	16	-0.60	0.60	9 ± 46
		Lag 31	-1.69	8.04	64	-1.00	1.00	74 ± 62
		Lag 41	-1.69	8.04	256	-1.50	1.50	200 ± 133
		Lag 32	-1.69	8.04	16	-1.00	1.00	103 ± 45
		Lag 42	-1.69	8.04	128	-1.20	1.50	229 ± 112
		Lag 43	-1.69	8.04	128	-1.20	1.50	126 ± 101
GRB061007	232683	Lag 21	23.86	65.08	2	-0.30	0.50	101 ± 17
		Lag 31	23.86	65.08	2	-0.30	0.50	154 ± 19
		Lag 41	23.86	65.08	4	-0.50	0.80	286 ± 28
		Lag 32	23.86	65.08	2	-0.20	0.20	30 ± 8
		Lag 42	23.86	65.08	2	-0.40	0.40	129 ± 17
		Lag 43	23.86	65.08	2	-0.30	0.40	82 ± 9
GRB061021	234905	Lag 21	-0.46	14.64	8	-1.00	1.00	-25 ± 52
		Lag 31	-0.46	14.64	8	-1.00	1.00	49 ± 51
		Lag 41	-0.46	14.64	32	-1.60	1.60	239 ± 85
		Lag 32	-0.46	14.64	8	-1.00	1.00	62 ± 42
		Lag 42	-0.46	14.64	32	-1.00	1.20	248 ± 78
		Lag 43	-0.46	14.64	32	-1.00	1.20	188 ± 79
GRB061121	239899	Lag 21	60.44	80.66	1	-0.20	0.20	18 ± 13
		Lag 31	60.44	80.66	1	-0.20	0.20	16 ± 12
		Lag 41	60.44	80.66	4	-0.40	0.40	26 ± 26
		Lag 32	60.44	80.66	1	-0.20	0.25	17 ± 7
		Lag 42	60.44	80.66	2	-0.20	0.25	28 ± 12
		Lag 43	60.44	80.66	2	-0.20	0.25	25 ± 11
GRB070306	263361	Lag 21	90.00	118.42	8	-2.00	2.00	88 ± 106
		Lag 31	90.00	118.42	16	-2.00	2.00	146 ± 100
		Lag 41	90.00	118.42	64	-4.00	6.00	1088 ± 391
		Lag 32	90.00	118.42	8	-2.00	2.00	114 ± 102
		Lag 42	90.00	118.42	64	-4.00	6.00	1098 ± 399
		Lag 43	90.00	118.42	64	-4.00	6.00	900 ± 408
GRB071010B	293795	Lag 21	-1.70	17.24	2	-1.00	1.00	-26 ± 48
		Lag 31	-1.70	17.24	4	-1.00	1.00	146 ± 52
		Lag 41	-1.70	17.24	32	-2.00	4.00	1024 ± 163
		Lag 32	-1.70	17.24	4	-1.00	1.00	185 ± 47
		Lag 42	-1.70	17.24	32	-2.00	4.00	1005 ± 157
		Lag 43	-1.70	17.24	32	-2.00	4.00	745 ± 161
GRB071020	294835	Lag 21	-3.22	1.14	2	-0.10	0.15	7 ± 7
		Lag 31	-3.22	1.14	2	-0.10	0.20	37 ± 12
		Lag 41	-3.22	1.14	8	-0.50	0.50	-50 ± 30
		Lag 32	-3.22	1.14	2	-0.10	0.25	47 ± 7
		Lag 42	-3.22	1.14	4	-0.10	0.30	69 ± 12
		Lag 43	-3.22	1.14	4	-0.20	0.30	28 ± 9

Table 5.3 (cont'd)

GRB	Trigger ID	LagXX	$T + X_S$ (s)	$T + X_E$ (s)	Bin Size (ms)	LS (s)	LE (s)	Lag Value (ms)
GRB080319B	306757	Lag 21	-2.85	57.57	2	-0.10	0.14	15 ± 2
		Lag 31	-2.85	57.57	2	-0.10	0.14	32 ± 3
		Lag 41	-2.85	57.57	2	-0.20	0.20	80 ± 17
		Lag 32	-2.85	57.57	2	-0.10	0.14	23 ± 2
		Lag 42	-2.85	57.57	2	-0.20	0.30	88 ± 8
		Lag 43	-2.85	57.57	2	-0.20	0.20	26 ± 5
GRB080319C	306778	Lag 21	-0.77	13.31	16	-1.00	1.00	106 ± 78
		Lag 31	-0.77	13.31	16	-2.00	2.00	216 ± 70
		Lag 41	-0.77	13.31	64	-2.00	2.00	89 ± 132
		Lag 32	-0.77	13.31	16	-1.00	1.00	134 ± 58
		Lag 42	-0.77	13.31	32	-1.00	1.00	-77 ± 95
		Lag 43	-0.77	13.31	32	-1.00	1.00	-119 ± 99
GRB080411	309010	Lag 21	38.46	48.45	2	-1.00	1.00	103 ± 12
		Lag 31	38.46	48.45	2	-1.00	1.00	220 ± 13
		Lag 41	38.46	48.45	2	-1.00	1.00	322 ± 27
		Lag 32	38.46	48.45	2	-1.00	1.00	122 ± 11
		Lag 42	38.46	48.45	2	-1.00	1.00	230 ± 26
		Lag 43	38.46	48.45	2	-1.00	1.00	112 ± 26
GRB080413A	309096	Lag 21	-0.42	9.05	8	-1.00	1.00	96 ± 60
		Lag 31	-0.42	9.05	8	-1.00	1.00	242 ± 65
		Lag 41	-0.42	9.05	64	-1.00	2.00	542 ± 125
		Lag 32	-0.42	9.05	8	-1.00	1.00	157 ± 43
		Lag 42	-0.42	9.05	32	-1.00	2.00	418 ± 111
		Lag 43	-0.42	9.05	32	-1.00	2.00	249 ± 108
GRB080413B	309111	Lag 21	-1.44	4.96	8	-1.00	1.00	59 ± 35
		Lag 31	-1.44	4.96	8	-1.00	1.00	144 ± 37
		Lag 41	-1.44	4.96	16	-1.00	1.00	353 ± 66
		Lag 32	-1.44	4.96	8	-1.00	1.00	82 ± 28
		Lag 42	-1.44	4.96	16	-1.00	1.00	276 ± 56
		Lag 43	-1.44	4.96	16	-1.00	1.00	188 ± 55
GRB080430	310613	Lag 21	-1.24	12.84	32	-2.00	2.00	270 ± 86
		Lag 31	-1.24	12.84	32	-2.00	2.00	391 ± 109
		Lag 41	-1.24	12.84	256	-4.00	4.00	730 ± 374
		Lag 32	-1.24	12.84	32	-2.00	2.00	83 ± 100
		Lag 42	-1.24	12.84	256	-4.00	4.00	540 ± 387
		Lag 43	-1.24	12.84	256	-4.00	4.00	388 ± 397
GRB080603B	313087	Lag 21	-0.54	5.10	16	-1.00	1.00	-222 ± 61
		Lag 31	-0.54	5.10	16	-1.00	1.00	-197 ± 67
		Lag 41	-0.54	5.10	32	-1.00	1.00	-427 ± 163
		Lag 32	-0.54	5.10	16	-1.00	1.00	50 ± 41
		Lag 42	-0.54	5.10	32	-1.00	0.50	-103 ± 71
		Lag 43	-0.54	5.10	32	-1.00	0.50	-172 ± 56
GRB080605	313299	Lag 21	-5.46	15.53	4	-1.00	1.00	58 ± 29
		Lag 31	-5.46	15.53	4	-1.00	1.00	98 ± 33
		Lag 41	-5.46	15.53	16	-0.50	1.20	196 ± 39
		Lag 32	-5.46	15.53	2	-0.30	0.40	73 ± 11
		Lag 42	-5.46	15.53	8	-0.30	0.40	96 ± 17
		Lag 43	-5.46	15.53	8	-0.30	0.40	39 ± 12

Table 5.3 (cont'd)

GRB	Trigger ID	LagXX	$T + X_S$ (s)	$T + X_E$ (s)	Bin Size (ms)	LS (s)	LE (s)	Lag Value (ms)
GRB080607	313417	Lag 21	-6.13	12.05	8	-0.40	0.40	121 ± 119
		Lag 31	-6.13	12.05	8	-0.40	0.60	163 ± 39
		Lag 41	-6.13	12.05	16	-0.40	0.60	194 ± 43
		Lag 32	-6.13	12.05	8	-0.40	0.40	19 ± 17
		Lag 42	-6.13	12.05	8	-0.40	0.40	64 ± 23
		Lag 43	-6.13	12.05	8	-0.40	0.40	25 ± 18
GRB080721	317508	Lag 21	-3.39	8.64	64	-2.00	2.00	99 ± 149
		Lag 31	-3.39	8.64	64	-2.00	2.00	122 ± 138
		Lag 41	-3.39	8.64	128	-2.00	2.00	341 ± 182
		Lag 32	-3.39	8.64	16	-0.80	0.80	16 ± 58
		Lag 42	-3.39	8.64	32	-0.80	0.80	256 ± 308
		Lag 43	-3.39	8.64	32	-0.80	0.80	167 ± 69
GRB080916A	324895	Lag 21	-2.66	39.58	16	-2.00	3.00	566 ± 172
		Lag 31	-2.66	39.58	32	-2.00	4.00	1468 ± 202
		Lag 41	-2.66	39.58	256	-4.00	6.00	2879 ± 271
		Lag 32	-2.66	39.58	32	-4.00	4.00	821 ± 100
		Lag 42	-2.66	39.58	128	-2.00	6.00	1900 ± 165
		Lag 43	-2.66	39.58	64	-2.00	4.00	842 ± 143
GRB081222	337914	Lag 21	-0.80	15.58	2	-0.80	1.20	127 ± 41
		Lag 31	-0.80	15.58	2	-0.80	1.00	262 ± 47
		Lag 41	-0.80	15.58	16	-2.00	3.00	610 ± 111
		Lag 32	-0.80	15.58	2	-0.80	0.80	113 ± 30
		Lag 42	-0.80	15.58	8	-1.80	2.80	444 ± 107
		Lag 43	-0.80	15.58	8	-1.80	2.80	197 ± 110
GRB090424	350311	Lag 21	-0.94	4.95	1	-0.10	0.25	20 ± 12
		Lag 31	-0.94	4.95	2	-0.10	0.25	29 ± 13
		Lag 41	-0.94	4.95	4	-0.10	0.25	39 ± 15
		Lag 32	-0.94	4.95	1	-0.10	0.25	23 ± 9
		Lag 42	-0.94	4.95	4	-0.10	0.25	27 ± 13
		Lag 43	-0.94	4.95	4	-0.20	0.30	17 ± 9
GRB090618	355083	Lag 21	46.01	135.35	4	-1.00	1.00	255 ± 21
		Lag 31	46.01	135.35	4	-1.00	1.00	447 ± 26
		Lag 41	46.01	135.35	4	-1.00	2.00	894 ± 43
		Lag 32	46.01	135.35	4	-1.00	1.00	173 ± 18
		Lag 42	46.01	135.35	4	-1.00	1.50	483 ± 34
		Lag 43	46.01	135.35	4	-1.00	1.50	283 ± 34
GRB090715B	357512	Lag 21	-4.80	21.06	16	-2.50	2.50	288 ± 117
		Lag 31	-4.80	21.06	16	-2.50	2.50	732 ± 127
		Lag 41	-4.80	21.06	64	-2.50	3.00	1080 ± 224
		Lag 32	-4.80	21.06	8	-2.50	2.50	470 ± 100
		Lag 42	-4.80	21.06	32	-2.50	2.50	928 ± 229
		Lag 43	-4.80	21.06	32	-2.50	2.50	375 ± 215

We noticed, as did Wu and Fenimore (2000), that the lag extraction is sensitive to a number of parameters. Hence, in Table 5.7, we specify the band pass that we used to extract the lag, segment of the light curve used, temporal bin resolution, and the fitting range used in the CCF vs time delay plot. These additional parameters are reported in order to facilitate reproduction of the results and direct comparison with other extraction techniques.

Figures 5.6 through 5.11 show log-log plots of isotropic peak luminosity vs redshift corrected spectral lag for various energy channel combinations. Red circles represent bursts from the "Gold" sample, blue diamonds shows bursts from the "Silver" sample and green triangles are bursts from the "Bronze" sample. The best-fit power-law curve is also shown in these plots with a dashed line. Since there is a large scatter in these plots, to compensate, the uncertainties of the fit parameters are multiplied by a factor of $\sqrt{\chi^2/\mathrm{ndf}}$ (see Table 5.4) [3]. The dotted lines indicate the estimated $1\,\sigma$ confidence level, which is obtained from the

_____

[3] ndf - number of degrees of freedom
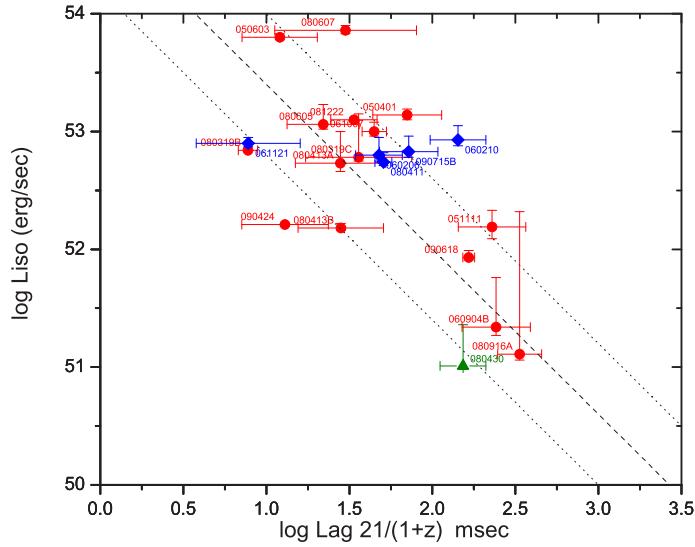
Figure 5.6 Isotropic luminosity as a function of spectral lag between BAT channel 2 (25–50 keV) and 1 (15–25 keV). The "Gold", "Silver", and "Bronze" samples are represented with red circles, blue diamonds, and green triangles respectively.
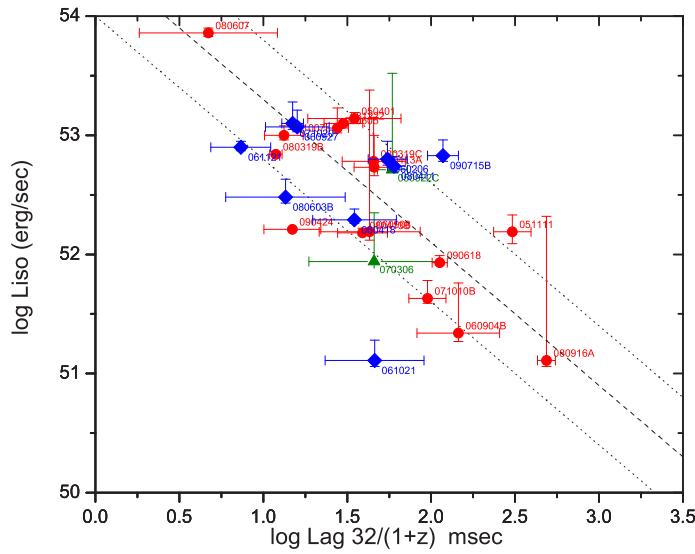
Figure 5.7 Isotropic luminosity as a function of spectral lag between BAT channel 3 (50–100 keV) and 2 (25–50 keV). The "Gold", "Silver", and "Bronze" samples are represented with red circles, blue diamonds, and green triangles respectively.
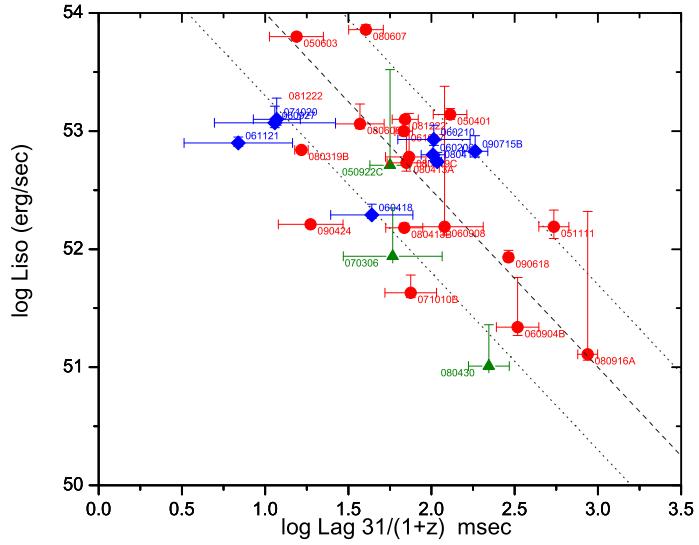
Figure 5.8 Isotropic luminosity as a function of spectral lag between BAT channel 3 (50–100 keV) and 1 (15–25 keV). The "Gold", "Silver", and "Bronze" samples are represented with red circles, blue diamonds, and green triangles respectively.
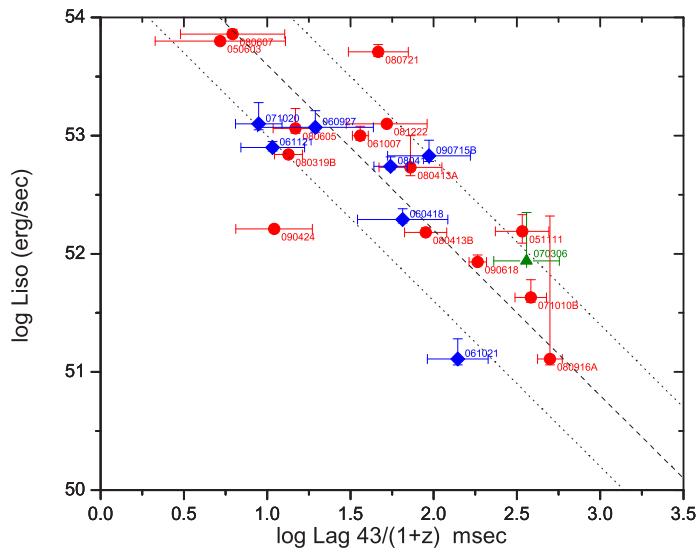
Figure 5.9 Isotropic luminosity as a function of spectral lag between BAT channel 4 (100–200 keV) and 3 (50–100 keV). The "Gold", "Silver", and "Bronze" samples are represented with red circles, blue diamonds, and green triangles respectively.
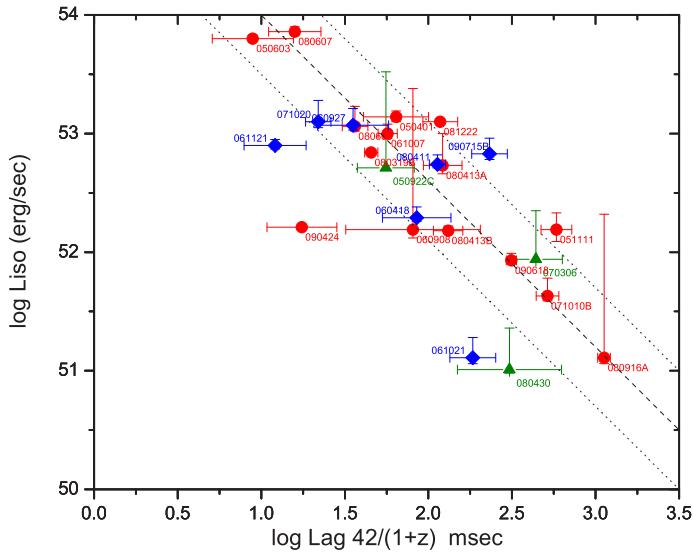
Figure 5.10 Isotropic luminosity as a function of spectral lag between BAT channel 4 (100–200 keV) and 2 (25–50 keV). The "Gold", "Silver", and "Bronze" samples are represented with red circles, blue diamonds, and green triangles respectively.
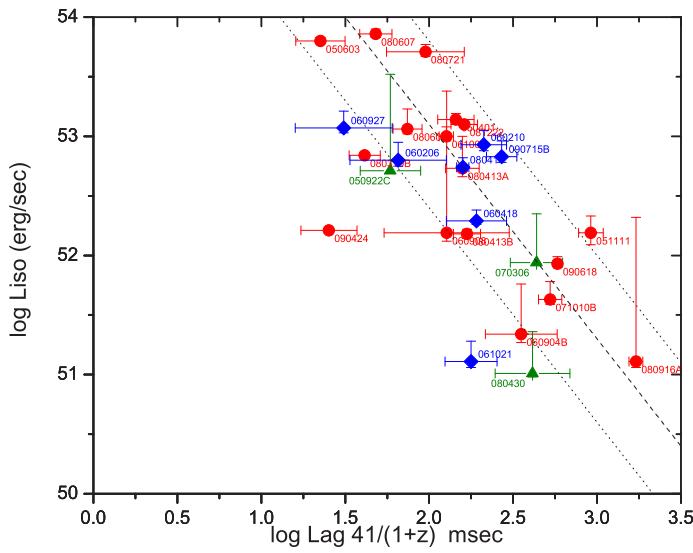
Figure 5.11 Isotropic luminosity as a function of spectral lag between BAT channel 4 (100–200 keV) and 1 (15–25 keV). The "Gold", "Silver", and "Bronze" samples are represented with red circles, blue diamonds, and green triangles respectively.

Table 5.4.   Correlation coefficients and fit parameters

Channels	Correlation	Best Fit	χ^2/ndf
Channel 21	-0.63	$\log L_{\mathrm{iso}} = (54.8 \pm 0.2) - (1.4 \pm 0.1) \log Lag21(1+z)^{-1}$	189.4/19
Channel 32	-0.66	$\log L_{\mathrm{iso}} = (54.5 \pm 0.2) - (1.2 \pm 0.1) \log Lag32(1+z)^{-1}$	216/25
Channel 31	-0.60	$\log L_{\mathrm{iso}} = (55.5 \pm 0.2) - (1.5 \pm 0.1) \log Lag31(1+z)^{-1}$	410.8/26
Channel 43	-0.77	$\log L_{\mathrm{iso}} = (55.0 \pm 0.3) - (1.4 \pm 0.1) \log Lag43(1+z)^{-1}$	109/20
Channel 42	-0.75	$\log L_{\mathrm{iso}} = (55.4 \pm 0.1) - (1.4 \pm 0.1) \log Lag42(1+z)^{-1}$	178.8/23
Channel 41	-0.67	$\log L_{\mathrm{iso}} = (56.7 \pm 0.3) - (1.8 \pm 0.1) \log Lag41(1+z)^{-1}$	212.1/25

cumulative fraction of the residual distribution taken from 16% to 84%.

It is interesting to note that GRB 080603B exhibits five negative lags out of six possible combinations. While these negative lags are not shown in the plots, it is worth noting that negative lags are not necessarily unphysical (Ryde, 2005). Moreover, in the few cases where the uncertainty is large, i.e., the extracted lags are consistent with zero, these points are not plotted either but are listed in Table 5.7. We recognize that the omission of these negative and zero lags is a potential source of bias.

As seen in Figure 5.6 through 5.11, our results support the existence of the lag-luminosity correlation originally proposed by Norris et al. (2000). Table 5.4 lists the correlation coefficients for all six channel combinations. The lag for channel combination 31 has the lowest correlation with L_{iso}, where the correlation coefficient is -0.60 (with chance probability of $\sim 1.5 \times 10^{-3}$) and the lag for channel 43 has the highest correlation with coefficient of -0.77 (with chance probability of $\sim 3.0 \times 10^{-4}$). However, we note that there is considerable scatter in the plots. The results of our best fit curves for each energy band combinations are also given in Table 5.4. The mean value of the power-law indices that we get for various channel combinations is 1.4 ± 0.3. Our value is consistent with the 1.14 power-law index Norris et al. (2000) reported using lags between BATSE energy bands $100 - 300$ keV and $25 - 50$ keV. Our results are also consistent with Stamatikos (2008) and Schaefer (2007) who reported values of 1.16 ± 0.21 and 1.01 ± 0.10 (assuming an uncertainty of 10%), respectively.

5.5.3   Hard-to-Soft Peak Evolution

Band (1997) showed that gamma-ray burst spectra typically undergo hard-to-soft peak evolution, i.e., the burst peak moves to later times for lower energy bands. In our sample we have six lag extractions for each burst. The perfect hard-to-soft peak evolution scenario is indicated by positive lag values for all channel combinations plus lag41 > lag42 > lag43

Table 5.5. Correlation coefficients with various corrections

Channels	No correction	z-correction	k-correction	both corrections
Channel 21	-0.38	-0.63	-0.29	-0.55
Channel 32	-0.43	-0.66	-0.33	-0.60
Channel 31	-0.39	-0.60	-0.31	-0.54
Channel 43	-0.61	-0.77	-0.54	-0.73
Channel 42	-0.58	-0.75	-0.51	-0.71
Channel 41	-0.43	-0.67	-0.32	-0.61

and lag31 > lag32. However, all bursts in our sample do not show this perfect behavior. Band (1997) used a scoring method to quantify the degree of hard-to-soft peak evolution. We used a more elaborate scoring method to assign a score to each GRB as follows: First, we increase the burst score by one if one of the six lag values is positive or decrease it by one if it is negative. Thus, a GRB can get a score ranging from -6 to +6 at this first step. Then, we compare the lag values of channel 4 as the base (lag43, lag42, and lag41). The score is increased by one if the burst meets one of the following conditions: lag41 > lag42, lag41 > lag43 or lag42 > lag43. We continue this procedure for channel 3 as the base also (lag31 > lag32). We decrease the score by one if it is otherwise. According to this scoring scheme a score of +10 corresponds to the perfect case that we mentioned earlier. A positive score indicates overall hard-to-soft peak evolution in the burst to some degree. A negative value indicates soft-to-hard peak evolution. Out of 31 bursts in our sample 19 bursts show perfect hard-to-soft peak evolution with a score of +10. About 97% of bursts in our sample have a score of greater than zero, which is consistent with the 90% value reported by Band (1997).

5.5.4 Limitations of Approximate k-correction

If one wants to use the lag-luminosity relation as a probe into the physics of GRBs (in the source rest frame), then a few corrections to the spectral lag are required; 1) correct for the time dilation effect (z-correction), 2) take into account the fact that for GRBs with various redshifts, observed energy bands correspond to different energy bands at the GRB rest frame (k-correction). Gehrels et al. (2006) approximately corrected observed spectral lag for the above mentioned effects. We also examined these corrections. The z-correction is done by multiplying the lag value by $(1 + z)^{-1}$. The k-correction is approximately done by multiplying the lag value by $(1 + z)^{0.33}$ (Gehrels et al., 2006; Zhang et al., 2009).

In table 5.5 we list the correlation coefficients with no correction, only z-correction, only k-correction and both corrections applied. For example, correlation coefficient of Lag31 and L_{iso} is -0.38 without any corrections. After the k-correction the correlation coefficient is -0.29. Therefore we do not gain a significant improvement in the correlation by applying the k-correction. However, the correlation improves significantly after the z-correction (-0.60). The approximate k-correction of (Gehrels et al., 2006) is based on the assumption that the spectral lag is proportional to the pulse width and pulse width is proportional to the energy (Zhang et al., 2009; Fenimore et al., 1995). These approximations depend on clearly identifying a pulse in the light curve and may be of limited validity for multi-pulse structures.

5.6 Lag-Luminosity Relation (Source Frame)

Typically the spectral lag is extracted between two arbitrary energy bands in the observer-frame. However, because of the redshift dependance of GRBs, these two energy bands can correspond to multiple energy bands in the GRB source-frame thus potentially introducing an arbitrary energy dependance to the extracted spectral lag.

In order to explore whether the lag-luminosity relation is intrinsic to the GRB, one clearly needs to extract spectral lags in the source-frame as opposed to the observer-frame. As mentioned before, at least two corrections are needed to accomplish this: 1) z-correction for the time dilation, 2) k-correction for the redshift dependance of the energy bands. The first correction is straightforward and is achieved by multiplying the extracted lag value (in the observer-frame) by $(1+z)^{-1}$. The second correction, on the other hand, is not so straightforward. Gehrels et al. (2006) attempted to approximately correct the spectral lag by multiplying the lag value (in the observer-frame) by $(1+z)^{0.33}$. As we noted earlier, this approximate correction is based on assumptions that may not be valid for a large fraction of bursts.

5.6.1 Fixed Energy Bands at Source Frame

Using the same sample of 31 bursts used in section 5.5, we avoid the difficulty of performing the approximate k-correction by choosing two appropriate energy bands fixed in the GRB source-frame and projecting these bands into the observer-frame using the relation
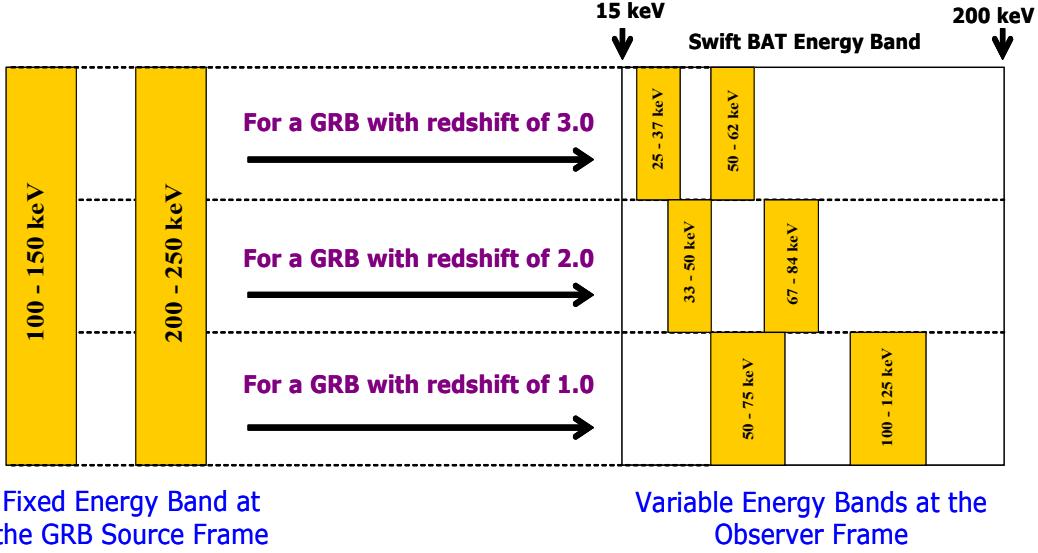
Figure 5.12 Fixed energy bands at the GRB source-frame are projected to various energy bands at the observer-frame, depending on the redshift.

$E_{\mathrm{observer}} = E_{\mathrm{source}}/(1+z)$. The fixed source-frame energy bands used for this analysis are $100 - 150$ and $200 - 250$ keV. These particular energy bands were selected so that after projecting to the observer-frame, they lie in the detectable energy range of the $Swift$ BAT instrument (see Figure 5.12). As mentioned earlier, even though the BAT can detect photons up 350 keV, we limited the upper-boundary to 200 keV (because of mask weighting, the contribution to the light curve from energies greater than ∼200 keV is negligible).

We used the `batmaskwtevt` and `batbinevt` tasks in FTOOLS to generate mask weighted, background-subtracted light curves, for various observer-frame energy bands depending on the redshift. The observer-frame energy bands used for each burst are shown in Table 5.6. Note that the energy gap between the two source-frame energy bands is fixed at 50 keV whereas in the observer-frame, as expected, this gap varies depending on the redshift of each burst (see the Table 5.6). For example, in GRB 060927, this gap is 8 keV and in GRB 061021, it is 37 keV. In comparison, for spectral lag extractions performed in the observer-frame, this gap is treated as a constant.

5.6.2 Source Frame Spectral Lag vs. Isotropic Peak Luminosity

The extracted spectral lags for the source-frame energy bands 100–150 and 200–250 keV are listed in Table 5.7. The $Swift$ BAT trigger ID, the segment of the light curve used for the lag extraction ($T + X_{\mathrm{S}}$ and $T + X_{\mathrm{E}}$, T is the trigger time), the time binning of the light

Table 5.6.　The observer-frame energy bands for bursts in the sample

GRB	Redshift	Low Energy Band (keV)	High Energy Band (keV)	Energy Gap (keV)
GRB050401	2.899	26-38	51-64	13
GRB050603	2.821	26-39	52-65	13
GRB050922C	2.199	31-47	63-78	16
GRB051111	1.549	39-59	78-98	20
GRB060206	4.056	20-30	40-49	10
GRB060210	3.913	20-31	41-51	10
GRB060418	1.490	40-60	80-100	20
GRB060904B	0.703	59-88	117-147	29
GRB060908	1.884	35-52	69-87	17
GRB060927	5.464	15-23	31-39	8
GRB061007	1.262	44-66	88-111	22
GRB061021	0.346	74-111	149-186	37
GRB061121	1.315	43-65	86-108	22
GRB070306	1.496	40-60	80-100	20
GRB071010B	0.947	51-77	103-128	26
GRB071020	2.145	32-48	64-79	16
GRB080319B	0.937	52-77	103-129	26
GRB080319C	1.949	34-51	68-85	17
GRB080411	1.030	49-74	99-123	25
GRB080413A	2.433	29-44	58-73	15
GRB080413B	1.101	48-71	95-119	24
GRB080430	0.767	57-85	113-141	28
GRB080603B	2.689	27-41	54-68	14
GRB080605	1.640	38-57	76-95	19
GRB080607	3.036	25-37	50-62	12
GRB080721	2.591	28-42	56-70	14
GRB080916A	0.689	59-89	118-148	30
GRB081222	2.770	27-40	53-66	13
GRB090424	0.544	65-97	130-162	32
GRB090618	0.540	65-97	130-162	32
GRB090715B	3.000	25-38	50-63	13

curve, and the Gaussian curve fitting range of the CCF vs time delay plot (with start time, and end time denoted as LS and LE respectively) are also given in Table 5.7. Out of 31 bursts in the sample there are 18 bursts which have lags greater than zero. The remaining 13 burst either have lags consistent with zero (11 bursts) or negative values (2 bursts).

For the 18 bursts with non zero lags, we find that the redshift corrected lag (τ) is anti-correlated with L_{iso}. The correlation coefficient for this relation is -0.74 $\pm$ 0.07 with a chance probability of $\sim 2.0 \times 10^{-3}$. The uncertainty in the correlation coefficient was obtained through a Monte Carlo simulation utilizing uncertainties in L_{iso} and τ. The extracted correlation coefficient is consistent with the correlation coefficient (averaged over the six combinations of standard BAT energy channels) of ~ -0.68 obtained in section 5.5.2.

Figures 5.13 shows a log-log plot of isotropic peak luminosity vs redshift-corrected spectral lag. The solid line shows the following best-fit power-law curve.

$$\log L_{iso} = (55.4 \pm 0.3) - (1.6 \pm 0.1) \log \frac{\tau}{1+z} \tag{5.5}$$

Since there is a considerable scatter, the uncertainties of the fit parameters are multiplied by a factor of $\sqrt{\chi^2/ndf} = \sqrt{67.22/16} = 2.05$. The dashed lines indicate the estimated 1 σ confidence level, which is obtained from the cumulative fraction of the residual distribution taken from 16% to 84%. The best-fit power-law index (-1.6 ± 0.1) is steeper compared to the observer-frame results obtained by Norris et al. (2000) (~ -1.14). However, it is consistent with the average power-law index of 1.4 ± 0.3 obtained in section 5.5.2.

Since about one third of the original sample of 31 bursts have spectral lags either negative or consistent with zero, in Figure 5.14 we display the results for the complete sample on a log-normal plot. The red circles represent bursts with non-zero lags. The blue squares show negative lags or those consistent with zero. The solid line is the best-fit curve obtained in Figure 5.13 and the dashed lines show 1 σ confidence level of the best-fit curve. We note that the extracted spectral lag appear to approach zero-lag asymptotically as the luminosity increases.

Table 5.7.   Spectral lag values of long duration $Swift$ BAT GRBs

| GRB	Trigger ID	$T + X_S$ (s)	$T + X_E$ (s)	Bin Size (ms)	LS (s)	LE (s)	Lag Value (ms)
GRB050401	113120	23.03	29.43	64	-2.00	2.00	310 ± 145
GRB050603	131560	-3.83	3.08	16	-0.40	0.40	-16 ± 21
GRB050922C	156467	-2.70	2.94	16	-1.00	1.00	136 ± 68
GRB051111	163438	-6.96	28.62	64	-4.00	4.00	333 ± 251
GRB060206	180455	-1.29	8.18	16	-2.00	2.00	86 ± 111
GRB060210	180977	-3.37	5.08	128	-4.00	4.00	658 ± 259
GRB060418	205851	-7.66	33.04	64	-2.00	2.00	-110 ± 106
GRB060904B	228006	-1.97	10.32	512	-6.00	6.00	124 ± 436
GRB060908	228581	-10.91	3.68	32	-2.00	2.00	78 ± 124
GRB060927	231362	-1.69	8.04	32	-1.00	1.00	18 ± 75
GRB061007	232683	23.86	65.08	4	-0.20	0.20	52 ± 22
GRB061021	234905	-0.46	14.64	512	-4.00	4.00	-430 ± 975
GRB061121	239899	60.44	80.66	4	-0.20	0.20	22 ± 10
GRB070306	263361	90.00	118.42	32	-4.00	2.00	-362 ± 247
GRB071010B	293795	-1.70	17.24	64	-2.00	2.00	404 ± 159
GRB071020	294835	-3.22	1.14	4	-0.20	0.40	35 ± 13
GRB080319B	306757	-2.85	57.57	4	-0.10	0.14	23 ± 6
GRB080319C	306778	-0.77	13.31	32	-1.00	1.00	174 ± 91
GRB080411	309010	38.46	48.45	4	-0.50	0.50	116 ± 25
GRB080413A	309096	-0.42	9.05	8	-1.00	1.00	107 ± 59
GRB080413B	309111	-1.44	4.96	32	-1.00	1.00	115 ± 50
GRB080430	310613	-1.24	12.84	256	-4.00	4.00	91 ± 431
GRB080603B	313087	-0.54	5.10	16	-1.00	1.00	5 ± 59
GRB080605	313299	-5.46	15.53	8	-0.20	0.20	35 ± 18
GRB080607	313417	-6.13	12.05	8	-0.50	0.50	26 ± 30
GRB080721	317508	-3.39	8.64	64	-2.00	2.00	-86 ± 110
GRB080916A	324895	-2.66	39.58	128	-2.00	4.00	585 ± 214
GRB081222	337914	-0.80	15.58	4	-1.00	1.00	227 ± 51
GRB090424	350311	-0.94	4.95	16	-0.20	0.20	14 ± 14
GRB090618	355083	46.01	135.35	8	-2.00	2.00	267 ± 72
GRB090715B	357512	-4.80	21.06	16	-2.00	3.00	275 ± 155
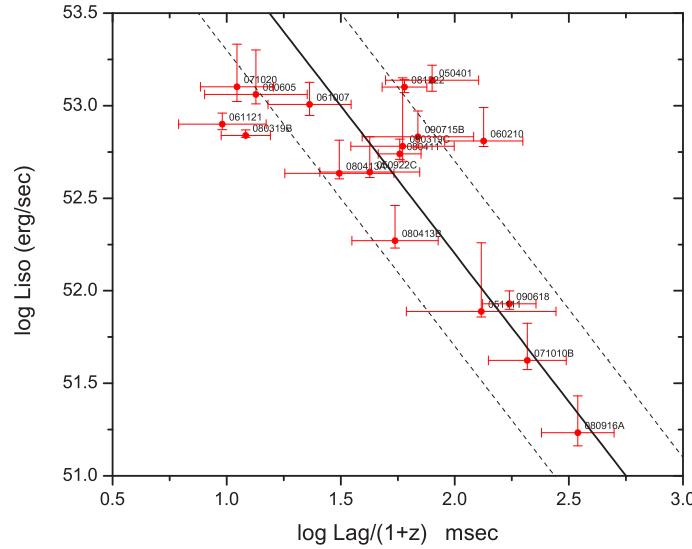
Figure 5.13 The spectral lags between the source-frame energy range bands $100 - 150$ keV and $200 - 250$ keV and the isotropic peak luminosity is plotted in a log-log plot.
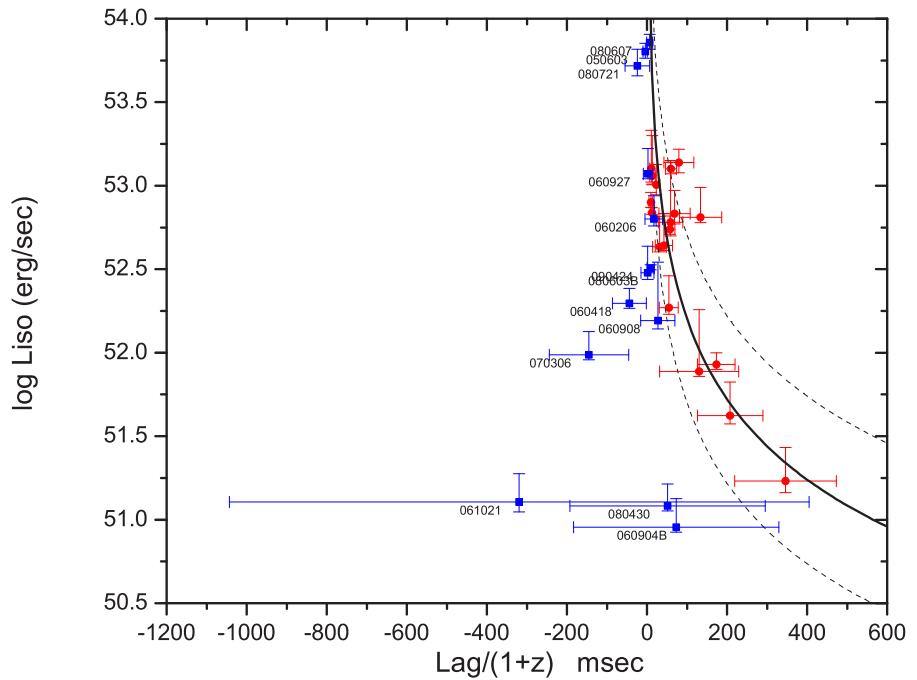
Figure 5.14 The spectral lags between the source-frame energy range bands $100 - 150$ keV and $200 - 250$ keV and the isotropic peak luminosity is plotted in a log-normal plot. The red circles represent bursts which have non zero lags. Bursts with negative lag values and lag values consistant with zero are shown in blue squares. Solid curve is the best fit power-law obtained in Figure 5.13.

5.7 Summary

In this chapter we have analyzed spectral lags based on the largest $Swift$ sample to date of 31 GRBs with measured redshifts. We used the CCF method to extract spectral lags and used a Monte Carlo simulation to determine its uncertainty. We extracted the spectral lags for all combinations of the standard $Swift$ observer-frame hard x-ray energy bands: 15-25 keV, 25-50 keV, 50-100 keV and 100-200 keV and plotted the time dilation corrected lag as a function of isotropic peak luminosity. We also extracted spectral lags between fixed source-frame energy bands 100–150 keV and 200–250 keV and investigated the lag-luminosity relation. We summarize the main results of our analysis as follows:

- The mean value of the correlation coefficient for various channel combinations is -0.68 with a chance probability of $\sim 0.7 \times 10^{-3}$.

- The mean value of the power-law index of the lag-luminosity correlation for fixed observer-frame energy bands is 1.4 ± 0.3.

- There is a higher degree of correlation of -0.74 ± 0.7 (chance probability of 2.0×10^{-3}) between the spectral lag and the isotropic peak luminosity in the fixed source-frame energy bands.

- The source-frame best-fit power-law gives an index of -1.6 ± 0.1, which is steeper than the index found in the observer-frame case.

- The lag-luminosity relation exists both in the fixed observer-frame energy band case and the fixed source-frame energy band case.

- Our study provides further evidence for the existence of the lag-luminosity relation both in observer and source frames, however with large scatter.

Chapter 6

Power Spectral Analysis of GRBs

6.1 Introduction

As we have seen in chapter 2, Gamma-ray Bursts (GRBs) show very complicated time profiles. The Fourier power density spectrum (PDS) of GRBs, on the other hand, seem to show relatively simple behavior. Giblin et al. (1998) found that a typical PDS shows a low-frequency power-law component and a high-frequency flat component (usually associated with Poisson noise). Beloborodov et al. (1998, 2000) considered each GRB as a realization of some common stochastic process and showed that when averaged over many bursts the resulting PDS exhibits a power-law behavior with an exponent of -1.67, which the authors note is consistent with the -5/3 Kolmogorov spectral index expected from processes involving turbulent flow. In addition, they claim that there is a break in the averaged PDS at ~ 1 Hz. The meaning of the break was not clear, since the authors were not in a position to correct their sample for the time dilation due to the cosmological redshifts.

Lazzati (2002) analyzed GRB power spectra by dividing them into six luminosity bins using the variability-luminosity correlation (Fenimore and Ramirez-Ruiz, 2000; Reichart et al., 2001; Guidorzi, 2005; Guidorzi et al., 2005, 2006; Li and Paczyński, 2006; Rizzuto et al., 2007). The PDS was averaged in each bin after correcting for pseudo-redshifts obtained through the variability-luminosity relation (Fenimore and Ramirez-Ruiz, 2000). Lazzati (2002) showed that the dominant frequency (f_d) of the PDS is strongly correlated with the variability parameter obtained by taking a modified variance of the de-trended light curve (Fenimore and Ramirez-Ruiz, 2000). Here f_d is obtained by finding the maximum of the function $f \times \text{PDS}(f)$ (see Lazzati (2002) for more details). The author further claims that

the red-noise component of the averaged PDS for the six luminosity bins is well described by a broken power-law function with a low-frequency slope of -2/3 and high-frequency slope of -2. In this case, the break frequency is a function of both luminosity and the variability parameter.

Borgonovo et al. (2007) did a similar analysis of power spectra but used measured redshift information to correct for time dilation effects before averaging. The burst sample was subdivided into two populations based on the calculated values of the autocorrelation function. After averaging, the PDS of one population shows a power-law index of $\sim$ -2.0 (consistent with the spectral index expected of Brownian motion) and the PDS of the other population is characterized by a low-frequency exponentially decaying component and a high-frequency power-law component with an index of $\sim$ -1.6 (which again is consistent with the -5/3 Kolmogorov spectral index).

Most of the previous work on power density spectra of GRBs has been based on observations with the Burst and Transient Source Experiment (BATSE) on the Compton Gamma Ray Observatory (Giblin et al., 1998; Beloborodov et al., 1998, 2000; Lazzati, 2002; Borgonovo et al., 2007) where a relatively modest amount of redshift information is available. The availability of redshift information in the $Swift$ era enables the study of intrinsic properties of bursts as well as providing an opportunity for further exploration of correlations involving burst parameters such as luminosity and variability.

In this chapter we investigate Fourier power density spectra of 206 $Swift$ long bursts. Unlike previous work, we avoid averaging PDS of multiple bursts and examine them individually. We have developed a method to extract individual PDS for each burst with uncertainties. Then we extract PDS for all the GRBs in the sample and investigate the distribution of the extracted parameters. In addition, we propose a new frequency-luminosity relation based on a sample of 58 GRBs with spectroscopically measured redshifts.

6.2 Fourier Power Spectrum Analysis

6.2.1 PDS Extraction

Using mask-weighted, 1-ms time binned light curves, we calculate the Fourier transform, a_f, of each GRB light curve, $R(t)$ (measured in counts/sec/detector), using a standard Fast
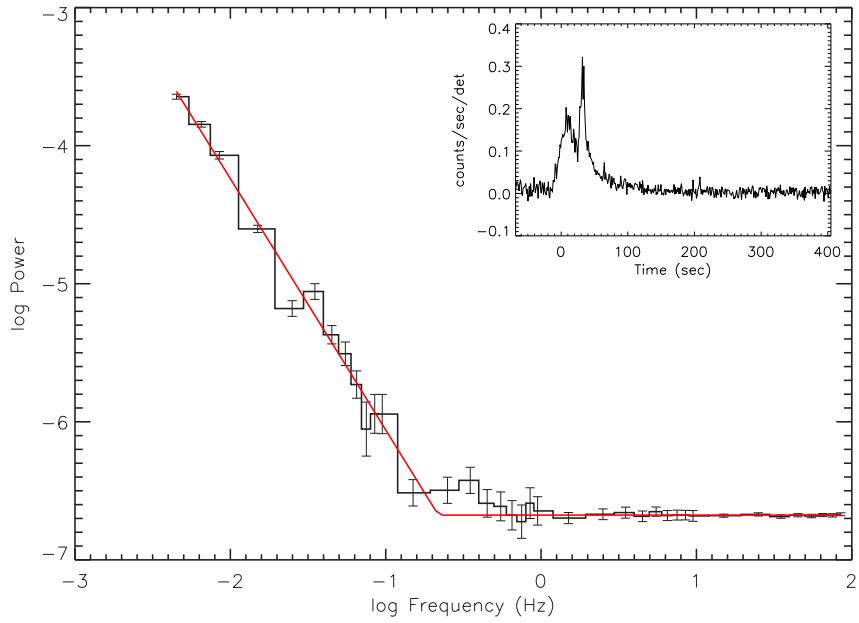
Figure 6.1 Power Density Spectrum of GRB 081203A. The low frequency power-law component is referred to as the 'red-noise' component and the flat high frequency region is called the 'white-noise' component. The inset shows the light curve of GRB081203A.

Fourier Transform (FFT)[1] algorithm (Jenkins and Watts, 1969; Press, 2002). We used a time segment of the burst light-curve where the total fluence is accumulated (i.e. start and end times corresponding to burst T100 which is calculated by the `battblocks` task). The PDS of each burst is calculated using $P_f = a_f\, a_f^*$. The power spectra are not normalized nor are they averaged.

This process of treating PDS individually is different from that of Beloborodov et al. (1998, 2000); Lazzati (2002) and Borgonovo et al. (2007), as they used some averaging process to obtain the slope of the red-noise component of the power spectra. The wide variety of light curves exhibited by GRBs is potentially indicative of different emission and scattering processes that eventually shape the observed light curves and therefore we have avoided averaging power spectra so as not to compromise this valuable information.

Typically, to obtain reliable fit parameters, the light curve is divided into multiple segments and a PDS is calculated for each segment. The overall PDS is then obtained by averaging the individual PDS. This method, however, is not suitable for transient events such as GRBs. Instead, in this work, we construct power spectra using logarithmic binning.

---

[1]We used the FFT routine in the IDL (Interactive Data Language) data analysis package.
`http://www.ittvis.com/ProductServices/IDL.aspx`

This techniques is used to redistribute the data points in the frequency domain so as to produce an acceptable fit over the relevant frequency range.

The uncertainties of the individual PDS are calculated as follows: For each burst, we simulate 100 light curves based on the original light curve ($R_{\mathrm{bin}}^{\mathrm{real}}$) and its uncertainty ($R_{\mathrm{bin}}^{\mathrm{real\,error}}$), i.e.

$$R_{\mathrm{bin}}^{\mathrm{simulated}} = R_{\mathrm{bin}}^{\mathrm{real}} + \zeta \times R_{\mathrm{bin}}^{\mathrm{real\,error}}. \tag{6.1}$$

Here ζ is a random number generated from a gaussian distribution with the mean equal to zero and the standard deviation equal to one. For each simulated light curve we calculate a PDS. Then we re-bin each PDS logarithmically. The uncertainties in the original PDS (obtained from the original light curve) are derived by taking the standard deviation of the 100 simulated PDS.

The power spectra for the GRBs in the sample are fitted with the function depicted in equation 6.2 (see Figure 6.1 for a typical fit). This function consists of a power-law component (to fit the low-frequency "red noise" component) and a constant component (to fit the flat high-frequency "white noise" component).

$$\log P(f) = \begin{cases} \alpha(\log f - \log f_{\mathrm{th}}) + \log P_{\mathrm{w}} & \text{for } f \leq f_{\mathrm{th}} \\ \log P_{\mathrm{w}} & \text{for } f > f_{\mathrm{th}}. \end{cases} \tag{6.2}$$

Here f_{th} is the threshold frequency where the red-noise component intersects the white-noise component of the power density spectrum, and P_{w} is the white-noise power density.

6.2.2 Sample Selection and Parameter Extraction

Out of 451 GRBs which triggered $Swift$ BAT from 2004 December 19 to 2009 December 31, we selected a sample of 226 long GRBs that show a significant red-noise component above the flat white-noise region. In Figure 6.2, we represent the two samples (the sample with clear red noise component is shown in red boxes and the sample with no or weak red-noise component is shown in blue inverted triangles) in a peak-photon-flux versus T100-duration plot. For the most part, the bursts that do not show a clear red-noise component are generally either weak and/or short in duration.

For the selected sample of 226 long GRBs we fitted the corresponding PDS with a simple power-law behavior given in equation 6.2, using the nonlinear least squares routine
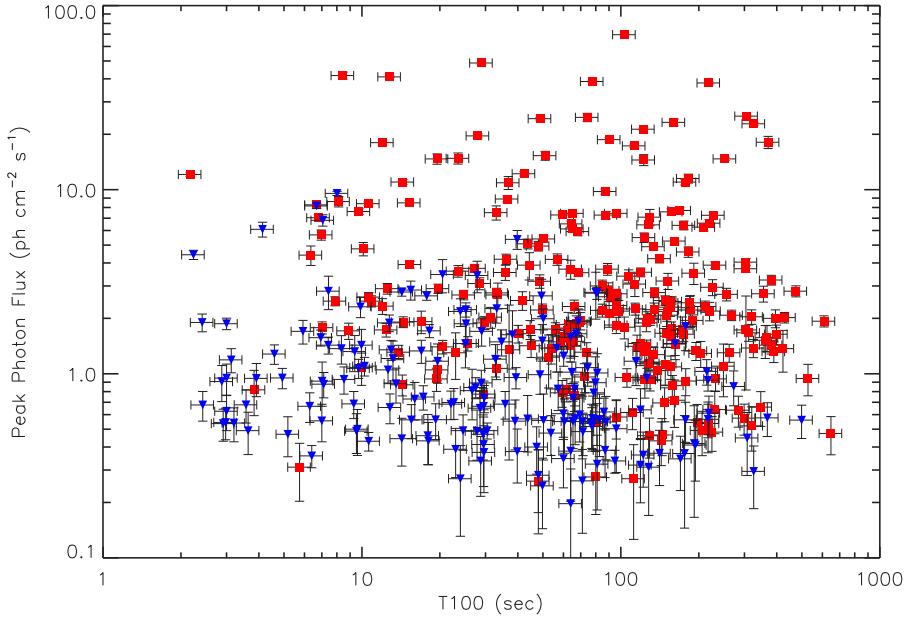
Figure 6.2 The peak photon flux versus the T100 duration. The final sample with a significant red noise component is shown in red boxes and the sample with no or weak red-noise component is shown in blue inverted triangles.

MPFIT (Markwardt, 2009). A typical fit is shown in Figure 6.1. Out of the 226 GRBs in the sample, 20 bursts could not be fitted by a simple power-law. These GRBs were excluded from further analysis. For the final sample of 206 bursts, the distributions of the extracted slopes (α) and threshold frequencies (f_{th}) are shown in Figure 6.3 and Figure 6.4 respectively. The distribution of slopes (α's) has a Gaussian-like shape and peaks around $\sim$ -1.4 with σ of about 0.6. The distribution of threshold frequencies (f_{th}'s) peaks around 1 Hz and also shows a broad distribution. The distribution of the redshift corrected f_{th} (i.e., $f_{th}(1+z)$), as depicted in the bottom panel of Figure 6.4, shows a large dispersion and non-gaussian shape. In Figure 6.5, we show a plot of α and f_{th}; we see a very weak positive correlation (0.24 ± 0.02) but we note at this stage of the analysis that f_{th} has not been corrected for noise contamination nor has it been corrected for redshift.

There are 76 GRBs in our sample with measured redshifts (spectroscopic or otherwise). For this sub-sample it is interesting to see whether the extracted parameters are redshift dependent. Figure 6.6 shows α (top panel), f_{th} (middle panel), and the redshift-corrected f_{th} (bottom panel) as a function of redshift. Very weak correlations are observed between α and redshift and also between f_{th} and redshift. However, no significant correlation is
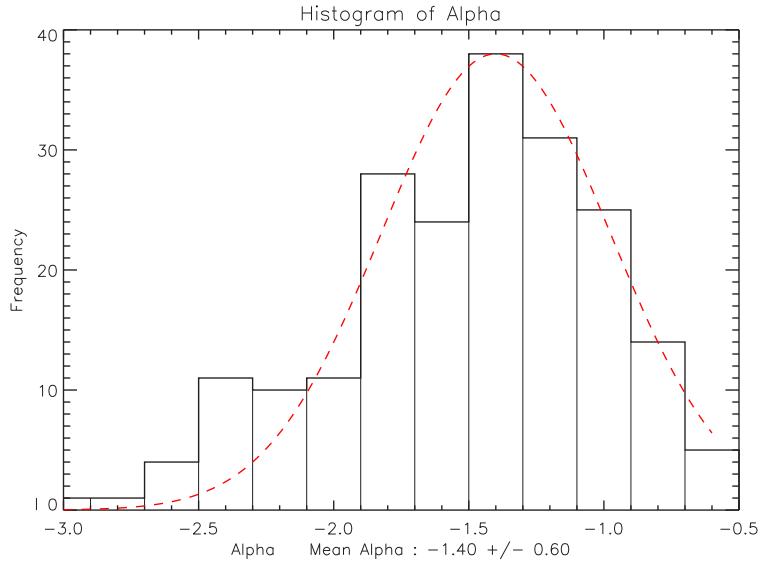
Figure 6.3 Histogram of the extracted slopes (α). The distribution shows a peak around -1.4 ± 0.6.
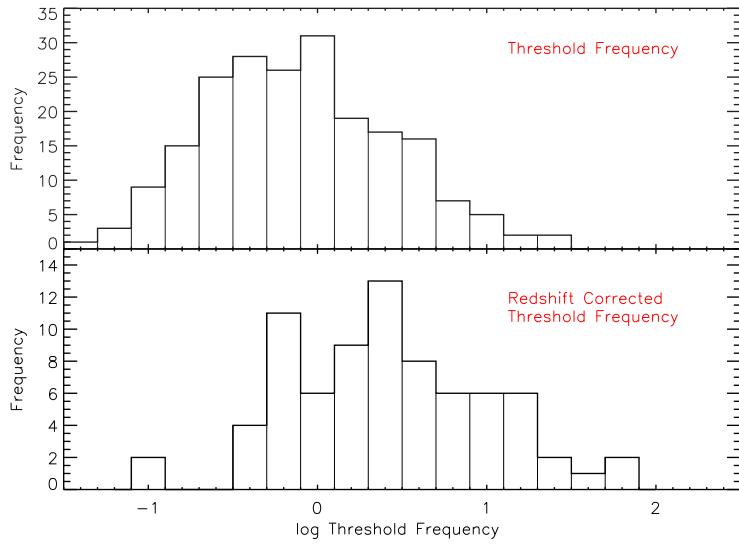
Figure 6.4 A histogram of extracted threshold frequencies (f_{th}) is shown in the top panel. The histogram peaks around ~ 1 Hz. The bottom panel shows a histogram of redshift-corrected f_{th} for subset of bursts with redshift measurements. Both distributions show a large dispersion.
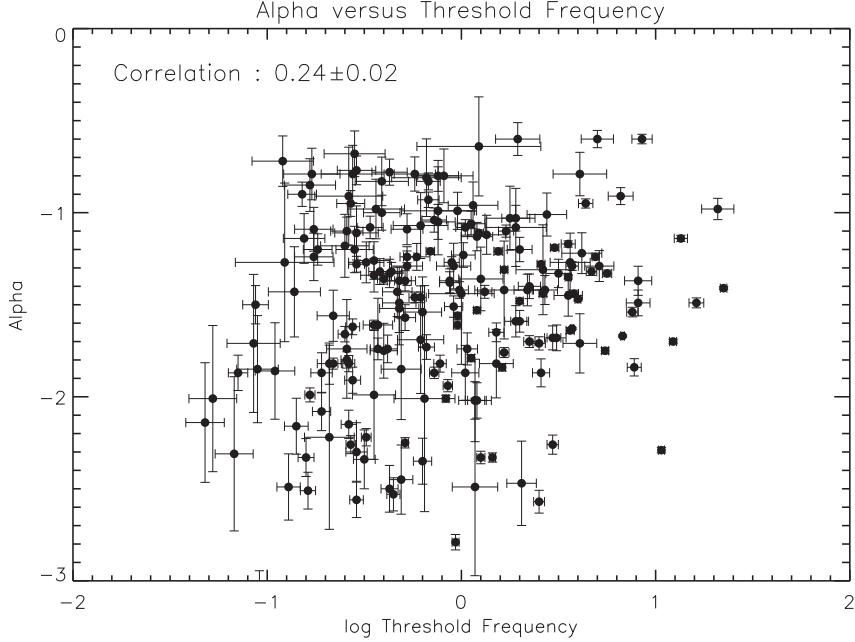
Figure 6.5 The extracted slope, α as a function of the threshold frequency, f_{th}. A very weak positive correlation is observed.

observed between $f_{\text{th}}(1 + z)$ and redshift.

6.3 Frequency-Luminosity Relation

In Ukwatta et al. (2009a) we proposed a correlation between the isotropic peak luminosity and the red-shift corrected f_{th} based on 27 GRBs. To investigate this further with a larger sample we have selected a sample of 58 bursts with spectroscopically measured redshifts and good spectral information. For this sample, we have calculated isotropic peak luminosity as described in Appendix B. Based on the availability of spectral information, we have divided the sample into three sub-samples: "Gold", "Silver", and "Bronze". The "Gold" sample with 15 bursts have all Band spectral parameters measured (Band et al., 1993). In the "Silver" sample (15 bursts), the E_{p} has been determined by fitting a cutoff power-law[2] (CPL) to spectra. These 15 bursts do not have the high-energy spectral index, β, measured, so we used the mean value of the BATSE β distribution, which is -2.36 ± 0.31 (Kaneko et al., 2006; Sakamoto et al., 2009). The "Bronze" sample, with 28 bursts, does not have a measured E_{p}. We have estimated it using the power-law index (Γ) of a simple power-law

---

[2]$dN/dE \sim E^{\alpha} \exp\left(-(2 + \alpha)E/E_{\text{p}}\right)$
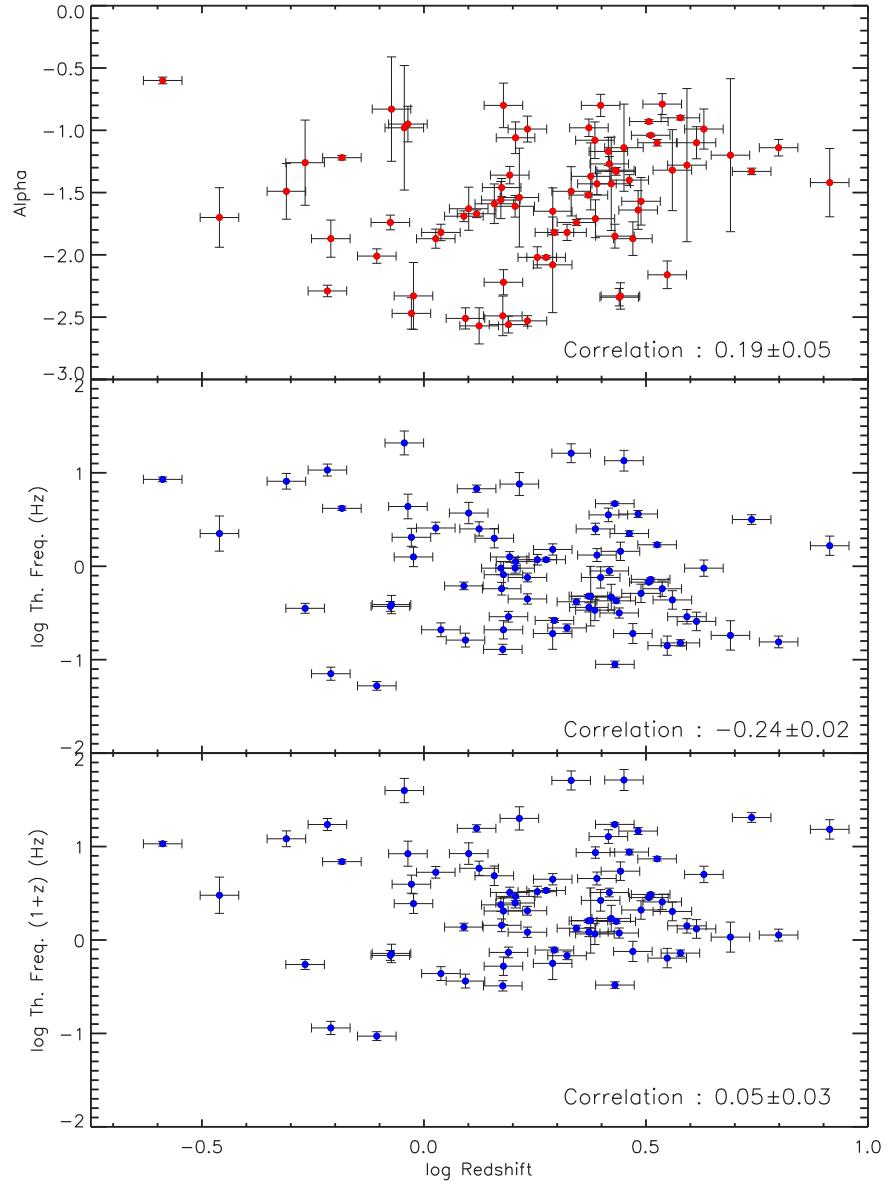
Figure 6.6 The slope α as a function of redshift (top panel), the threshold frequency as a function of redshift (middle panel), and redshift-corrected f_{th} as a function of redshift (bottom panel). The top and the middle panels show very weak correlations while the bottom panel shows no significant correlation. Note that conservative 10% uncertainties were assumed for redshift values.

(PL) fit as described in Sakamoto et al. (2009). For these 28 bursts, the low-energy spectral index, α, and the high-energy spectral index, β, were not known, so we used the mean values of the BATSE α and β distribution, which are -0.87 ± 0.33 and -2.36 ± 0.31 respectively (Kaneko et al., 2006; Sakamoto et al., 2009).
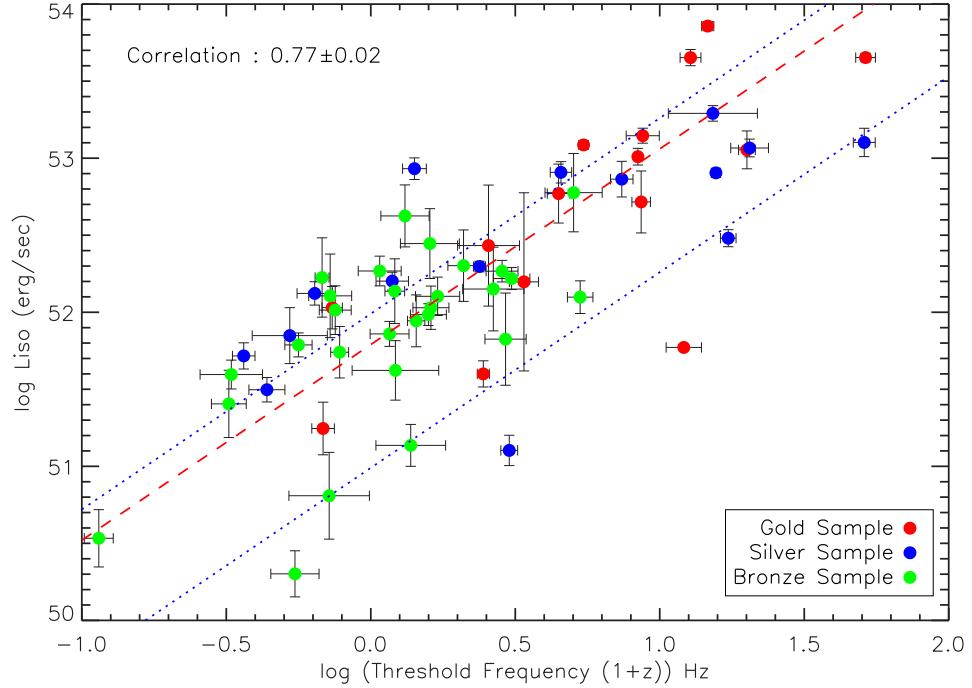
Figure 6.7 Isotropic peak luminosity as a function of the redshift- corrected threshold frequency, $f_{\text{th}}(1+z)$. The parameters are correlated with a correlation coefficient of 0.77 ± 0.02 and the best-fit power-law yields an exponent of 1.27 ± 0.12.

The isotropic luminosity as a function of the redshift-corrected threshold frequency is shown in Figure 6.7. In the figure, the "Gold", "Silver", and "Bronze" samples are shown in red, blue, and green filled circles respectively. A clear positive correlation can be seen in the figure. The Pearson's correlation coefficient is 0.77 ± 0.02, where the uncertainty was obtained through a Monte Carlo simulation. The probability that the above correlation occurs due to random chance is $\sim 4.5 \times 10^{-9}$. Our best-fit is shown as a red dashed line in Figure 6.7 yielding the following relation between L_{iso} and f_{th}:

$$\log L_{\text{iso}} = (51.79 \pm 0.12) + (1.27 \pm 0.12) \log(f_{\text{th}}(z+1)). \qquad (6.3)$$

To compensate for the large scatter in the plot, the uncertainties of the fit parameters are

multiplied by a factor of $\sqrt{\chi^2/\text{ndf}} = \sqrt{1766/56} \approx 6.0$ where ndf is the number of degrees of freedom. The blue dotted lines indicate the estimated 1σ confidence level, which is obtained from the cumulative fraction of the residual distribution taken from 16% to 84%.

Our result for the slope in Figure 6.7 is consistent with the value of 1.4 ± 0.2 obtained by Ukwatta et al. (2009a) using 27 GRBs. This is encouraging because the results of Ukwatta et al. (2009a) were obtained using non-mask-weighted event-by-event data instead of the mask-weighted data that we use in the current work. We also note that with the increase of the sample size by about a factor of two the correlation coefficient has also improved from 0.69 ± 0.03 to 0.77 ± 0.02. The correlation between frequency and luminosity is clearly intriguing but there remain potential observational biases which we address in a later section.

6.4 Brightness Dependance of PDS Fit Parameters

It has been reported previously (Beloborodov et al., 2000) that the PDS slope is correlated with the burst brightness. In order to check our sample for this effect, we display, in Figure 6.8, the slope (α) against brightness indicators: the peak photon flux and the fluence. Very weak negative correlations are observed in both cases.

The other extracted parameter, the noise crossing threshold frequency (f_{th}) of the PDS, is also expected to depend on the brightness of the GRB. Presumably, the 'red-noise' component of the PDS comes primarily from the GRB but the flat 'white-noise' component can in principle arise from the Poisson noise (intensity fluctuations) associated with the GRB and the natural background in the field-of-view of the detector. For distant and/or intrinsically weak bursts, noise unrelated to the burst may dominate the observed white-noise component, thereby overwhelming the red-noise part of the signal. This, in turn, would make the extraction of the threshold frequency brightness-dependent. In Figure 6.9 we plot the peak photon flux and the photon fluence as a function of the threshold frequency. The red dashed line in the top panel of Figure 6.9 is the best fit, given by equation 6.4, and blue dotted lines indicate a 1σ confidence interval.

$$\log \text{PPF} = (0.58 \pm 0.03) + (0.82 \pm 0.04) \log f_{\text{th}} \tag{6.4}$$

Indeed, a positive correlation can be seen between f_{th} and the peak photon flux. However,
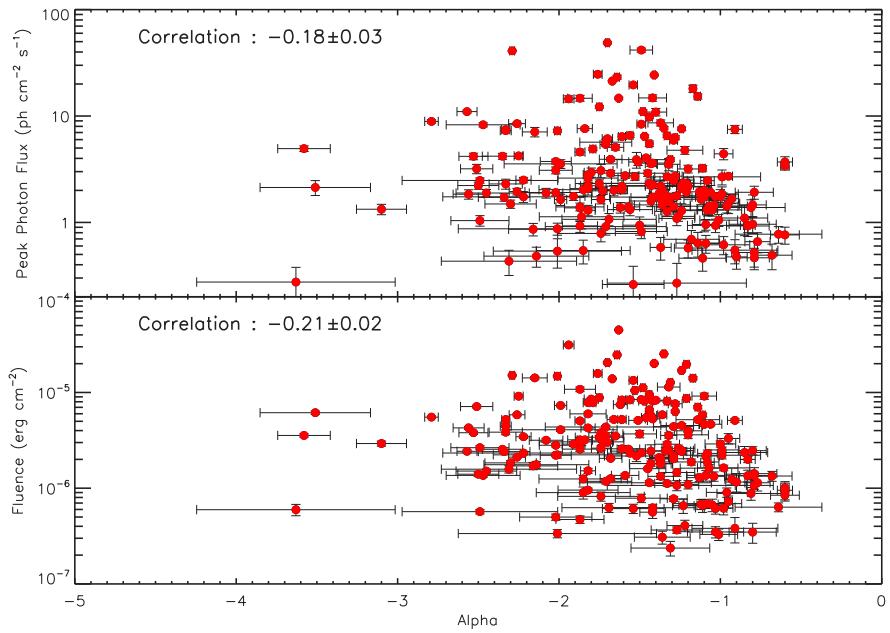
Figure 6.8 The peak photon flux as a function of alpha (top panel) and the fluence as a function of alpha (bottom panel). Very weak negative correlations are observed in both cases.
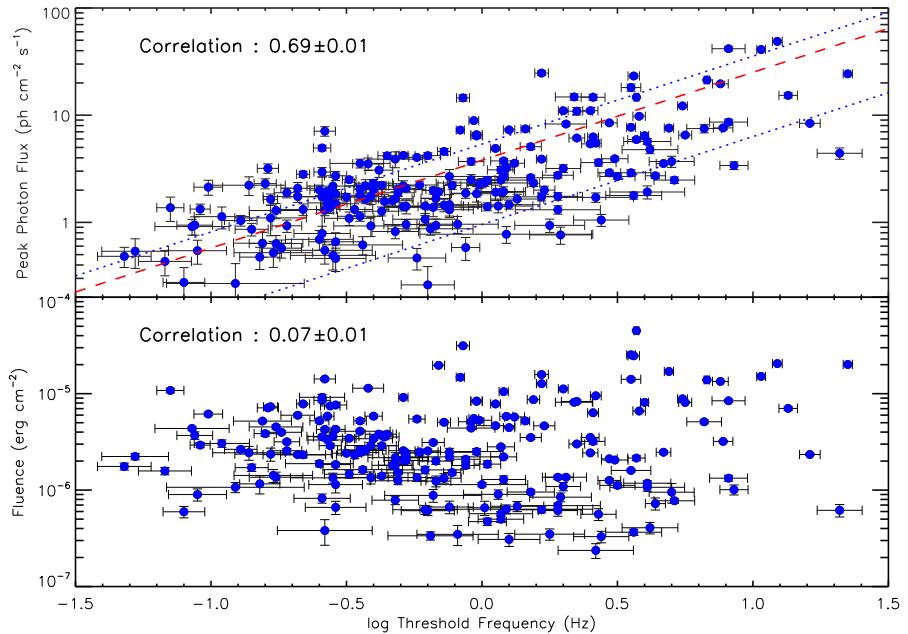

Figure 6.9 The peak photon flux as a function of threshold frequency (top panel) and the photon fluence as a function of threshold frequency (bottom panel). No significant correlation is observed between fluence and f_{th} but a significant correlation is observed between peak photon flux and f_{th}.
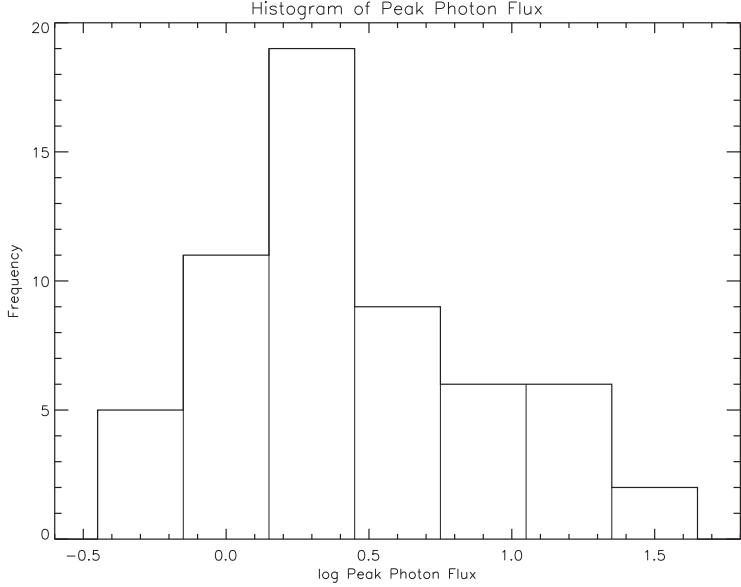
Figure 6.10 Histogram of the peak photon flux of the sample of 58 bursts used to generate Figure 6.7.

no significant correlation is observed between f_{th} and fluence. We discus this important matter in the next section.

It is conceivable that the proposed frequency-luminosity correlation is a direct result of the observed correlation between f_{th} and the peak photon flux of the burst (see the top panel of Figure 6.9). If this is the case, then for a statistically significant sample of bursts with similar apparent brightness, we should not see a correlation between f_{th} and L_{iso}. In order to select a sample of GRBs with similar apparent brightness we plot in Figure 6.10 the peak photon flux distribution for the sample of 58 bursts used to investigate the frequency-luminosity correlation in Figure 6.7. We see from Figure 6.10 that about half of the sample (28 GRBs) have a very similar peak photon flux ($0.0 <$ log (peak photon flux) < 0.5). For this subset of bursts we plotted their peak photon flux and L_{iso} as a function of f_{th} and the results are shown in Figure 6.11. In the top panel of Figure 6.11, it is clear that there is a significant correlation between f_{th} and L_{iso} with correlation coefficient of 0.60 ± 0.06. This implies that the correlation observed in Figure 6.7 ($f_{th}(1 + z)$ - L_{iso} correlation) is not entirely due to the correlation seen in the top panel of Figure 6.9 ($f_{th}-$peak photon flux correlation). We now correct the f_{th} of this limited sample (with similar apparent brightness) for redshift to see its effect. Plotted in the bottom panel of Figure 6.11 are the redshift corrected data. We note that the correlation strength increases to a value of

88
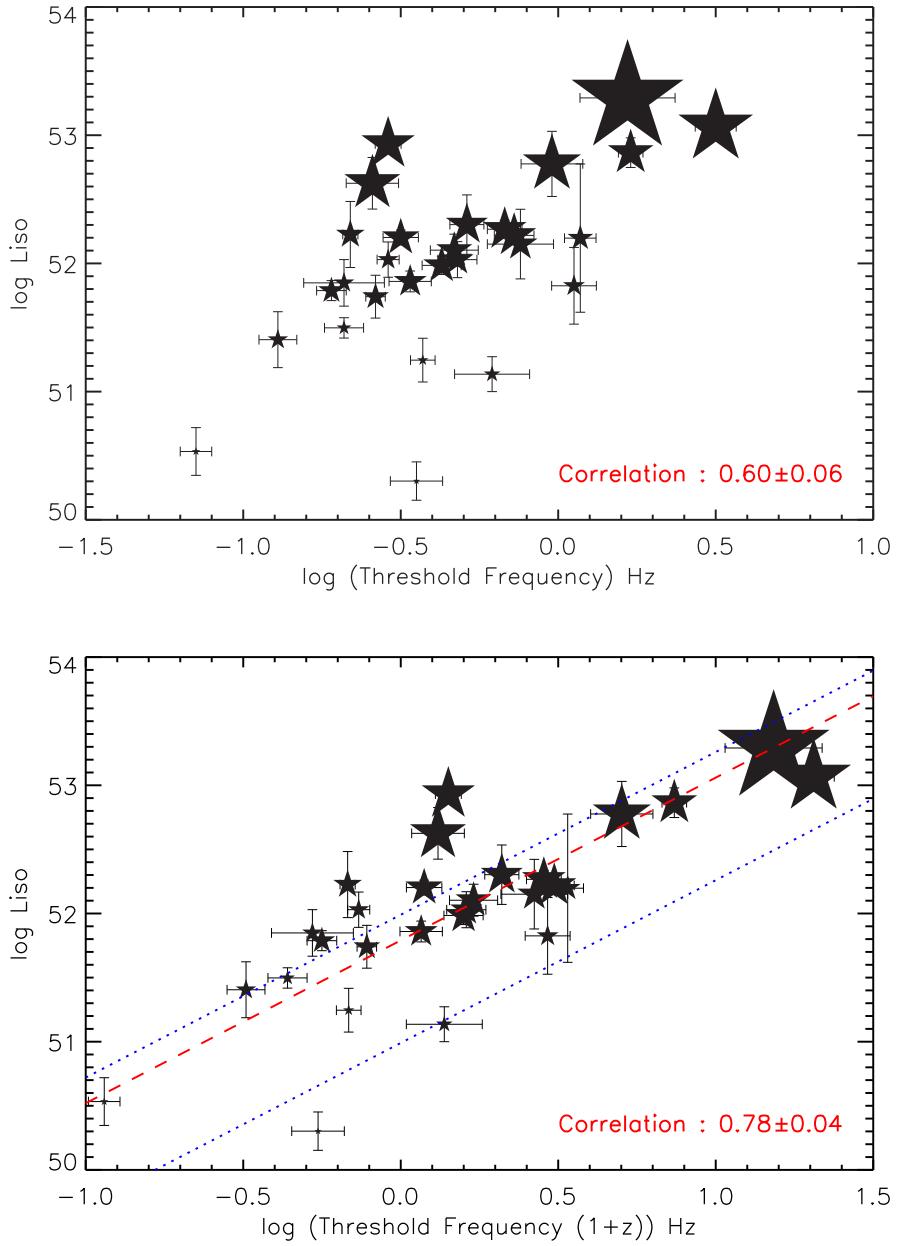
Figure 6.11 The isotropic peak luminosity as a function of threshold frequency (with and without redshift correction) for a sample of bursts with narrow apparent brightness range. The red-dashed and blue-dotted lines are the same fit curves shown in Figure 6.7. The size of the star is proportional to the redshift of the burst.
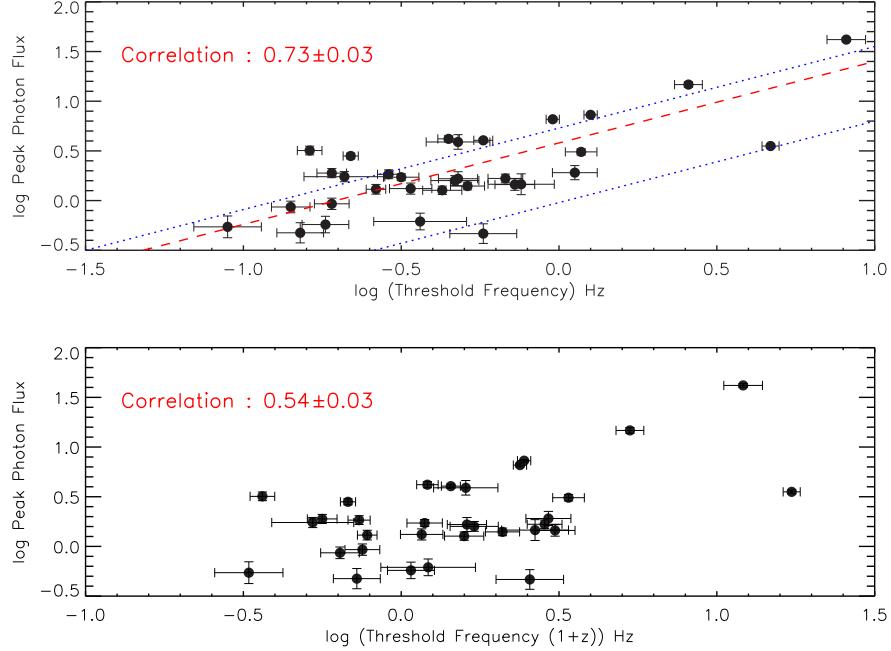
Figure 6.12 Peak photon flux as a function of f_{th} (top panel) and redshift corrected f_{th} (bottom panel) for a sample bursts with roughly constant luminosity. The red dashed line in the top panel is the best fit line obtained in Figure 6.9 and blue dotted lines indicate 1σ confidence interval.

0.78 ± 0.04, in part due to the natural correlation between redshift and L_{iso}.

In addition, we can approach the issue from the other direction, i.e., we select a subset of bursts with similar luminosity and ask the question whether the correlation between peak photon flux and f_{th} comes from the proposed $f_{\text{th}}(1+z)$ - L_{iso} correlation. In order to perform this test we selected a subset of bursts which have roughly the same L_{iso} values ($51.5 < \log L_{\text{iso}} < 52.5$) and plotted their peak photon flux as a function of f_{th}. In Figure 6.12 we show the peak photon flux as a function of f_{th} (top panel) and the redshift corrected f_{th} (bottom panel). There is clearly a strong correlation between the two parameters in both panels. It is interesting, however, that after the redshift correction, the correlation strength drops significantly. Accordingly, it would appear that the correlation between the peak photon flux and f_{th} (top panel of Figure 6.9) is not entirely due to the $f_{\text{th}}(1+z)$ - L_{iso} correlation (Figure 6.7). Since the spectral power is proportional to the square of the flux and the PDS follows a $f^{-\alpha}$ behavior (see Figure 6.3), we expect to see a correlation between peak photon flux and f_{th}. Hence, this correlation is mainly observational.

6.5 Observational Biases of Frequency-Luminosity Relation

6.5.1 Measuring Noise Level of Light Curves

Now we turn to the question of observational biases and in particular the dependance of the extracted threshold frequency on the noise-level of the burst. The obvious question is how to determine the noise-level for each burst. One way of defining the noise-level is the following:

$$\text{Noise Level} = \frac{\text{Std.Dev.(Detrended LC)}}{\text{Peak Count Rate}} \times 100\%. \tag{6.5}$$

The detrending of the light curve (LC) can be done in a number of ways and we adopted the following method: We generated two light curves of the same burst with two bin sizes. In order to produce the coarser binned light curve, we chose a time bin size that resulted in at least 100 points in the burst duration (T100). The other light curve may have bin sizes that vary from 1 ms up to the coarser bin size. Clearly, with the different binning, the two light curves will have a different number of points. In order to detrend properly, we need to have the same number of points in the two light curves. We accomplish this by using a simple linear interpolation of the coarser binned light curve. The interpolated light curve is then subtracted from the finer binned light curve to generate the detrended light curve.

Using equation 6.5 we extract a noise level for each burst. Unfortunately, the extracted noise-level depends on the bin size used in the detending process. This is a worrisome feature and therefore needs to be either removed or accounted for before the noise level of all the bursts can be treated on an equal footing.

The level of the flat white-noise region of the PDS does not depend on the bin size, i.e., for a given burst the white noise level is constant irrespective of the bin size, and for that matter so too are the extracted parameters α and f_{th}. In order to remove the bin size dependence in the extraction of the noise-level, we modify equation 6.5 as follows.

$$\text{Noise Level} = \frac{1}{\sqrt{N}} \frac{\text{Std.Dev.(Detrended LC)}}{\text{Peak Count Rate}} \times 100\%. \tag{6.6}$$

Here N is the number of data points in the finely binned light curve. Our tests indicate that the results given by equation 6.6 do not depend on the time bin size of the light curve and provide a robust measure of the noise-level of a given burst.
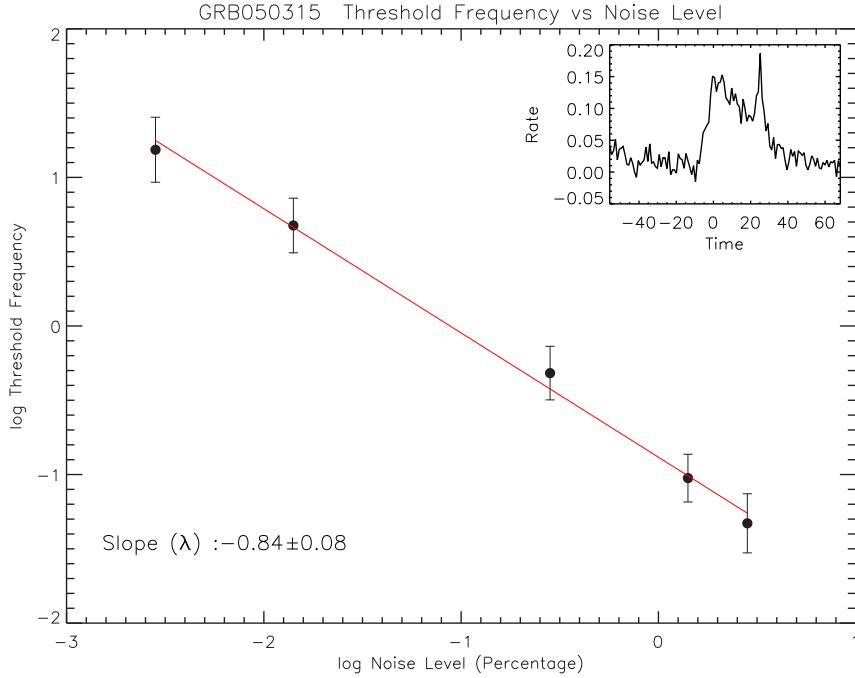
Figure 6.13 The extracted threshold frequency as a function of the noise-level in a log-log scale. The threshold frequency displays a power-law dependance on the noise-level of the burst with a index (λ) of -0.84 ± 0.08 for GRB 050315. The inset shows the time profile of the burst.

6.5.2 Threshold Frequency: Noise Level Dependance

In order to further investigate the dependance of f_{th} on the noise-level, we performed additional tests. We simulated different noise levels by adding increasing amounts of Gaussian noise to a burst light curve (in this case GRB 050315). Then we extracted f_{th} values for each setting of the noise-level. Our results, the extracted frequency values versus the noise-level, are shown in Figure 6.13 as a log-log plot. The threshold frequency does indeed depend on the noise-level. However, there is a linear relationship between the logarithmic values of the two quantities. This relation is important to know because it can be used to correct the extracted f_{th} values to some nominal noise-level that is common to all bursts in the sample.

By performing the same test on the other bursts in our sample, we established that the relation between f_{th} and the noise-level depends on the profile of the burst, i.e., the slope (λ) of the log-log plot is different for each burst. Shown in the bottom panel of Figure 6.14 is the distribution the slopes, λ, obtained for our sample of 58 bursts used in the f_{th}-L_{iso} relation. Correspondingly, the noise-level (NL) distribution is shown in the top panel of Figure 6.14. This distribution shows a clear peak around the log value of -0.2 (NL $\sim$ 0.6)

while the λ distribution peaks around the value of -0.8.
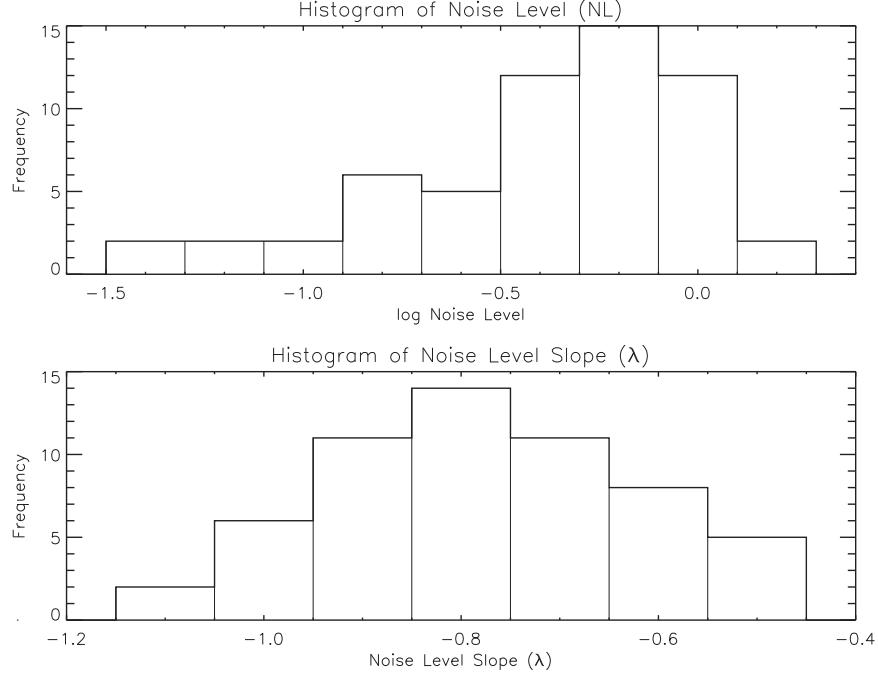
Figure 6.14 Distribution of noise-levels (top panel) and noise-level slope, λ, (bottom panel) in the sample.

6.5.3 Noise Corrected Frequency-Luminosity Relation

We are now in a position to treat all the bursts in our sample on an equal footing and test whether the f_{th}-L_{iso} correlation, observed in Figure 6.7, survives. The aim is to extract threshold frequencies which are consistent with a noise-level that is common to all the bursts in our sample. In order to accomplish this, we choose an arbitrary noise level of NL = 1.0 (see Figure 6.13) and use the following relation to extract a corrected f_{th} for each burst:

$$\log f_{\mathrm{th[NL=1]}} = \log f_{\mathrm{th[NL=burst]}} - \lambda_{\mathrm{burst}} \log(\mathrm{NL}_{\mathrm{[NL=burst]}}). \qquad (6.7)$$

Here, $f_{\mathrm{th[NL=burst]}}$ is the extracted threshold frequency for a given burst, λ_{burst} is the noise-level slope corresponding to the same burst and $\mathrm{NL}_{\mathrm{[NL=burst]}}$ is the burst noise-level determined by equation 6.6. The correction procedure is repeated for each burst in our sample. The corrected threshold frequency values of 58 long GRBs are given in Table 6.1. To gauge the size of the correction, we plot in Figure 6.15 (in a log-log scale) the corrected f_{th} values versus the uncorrected f_{th}. We note that there is a strong correlation between the two pa-

93

rameters. This is a reflection of the clustering of the NL and λ seen in Figure 6.14. We also plotted the NL as a function of the noise-corrected, redshift-corrected f_{th} in Figure 6.16. There is no correlation between these two parameters, thus giving us confidence in the noise correction procedure.
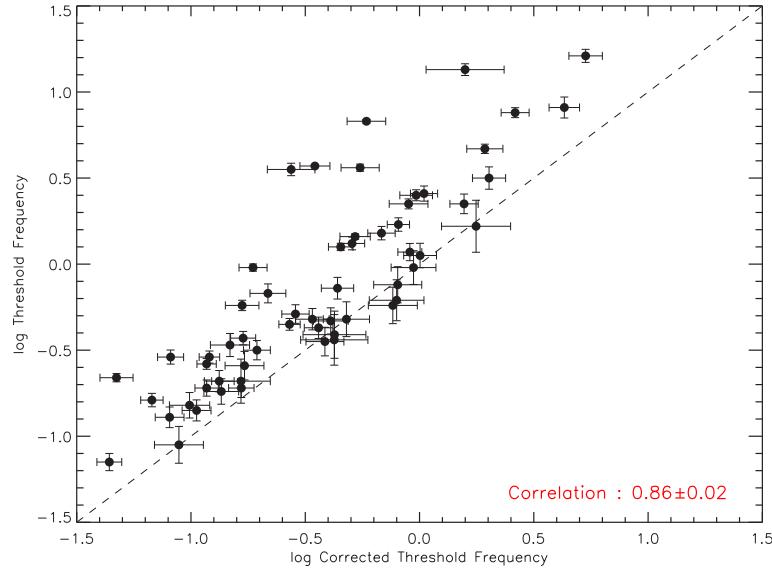

Figure 6.15 The threshold frequency versus the noise-corrected threshold frequency. The two parameters show a strong correlation with correlation coefficient of 0.86. The dashed line indicates the equality line of the two parameters.

Table 6.1.   Corrected threshold frequency values of 58 long GRBs.

GRB	Redshift	Noise Level	λ	$\log f_{\mathrm{th}}$ Hz	Corrected $f_{\mathrm{th}}(1+z)$ Hz
GRB050315	1.949	0.560	-0.84 ± 0.08	-0.72 ± 0.05	0.35 ± 0.04
GRB050319	3.240	0.610	-1.02 ± 0.15	-0.14 ± 0.06	1.86 ± 0.30
GRB050401	2.900	0.540	-0.58 ± 0.09	0.35 ± 0.06	6.11 ± 0.87
GRB050505	4.270	0.980	-0.72 ± 0.17	-0.02 ± 0.10	4.96 ± 1.13
GRB050603	2.821	0.090	-0.89 ± 0.16	1.13 ± 0.03	6.05 ± 2.44
GRB051109A	2.346	1.000	-0.67 ± 0.14	-0.32 ± 0.10	1.60 ± 0.38
GRB051111	1.550	0.340	-0.81 ± 0.06	-0.54 ± 0.03	0.31 ± 0.03
GRB060115	3.530	0.680	-0.75 ± 0.10	-0.85 ± 0.06	0.48 ± 0.07
GRB060210	3.910	0.320	-1.11 ± 0.08	-0.54 ± 0.04	0.40 ± 0.05
GRB060418	1.490	0.150	-0.86 ± 0.07	-0.02 ± 0.02	0.47 ± 0.07
GRB060502A	1.510	0.790	-0.99 ± 0.09	-0.68 ± 0.13	0.42 ± 0.12
GRB060510B	4.900	0.750	-1.02 ± 0.14	-0.74 ± 0.07	0.80 ± 0.14
GRB060526	3.210	0.310	-0.97 ± 0.11	-0.17 ± 0.06	0.91 ± 0.17
GRB060605	3.780	0.560	-0.74 ± 0.19	-0.82 ± 0.07	0.47 ± 0.10
GRB060607A	3.082	0.430	-0.69 ± 0.07	-0.29 ± 0.05	1.17 ± 0.16
GRB060714	2.710	0.800	-0.74 ± 0.09	-0.37 ± 0.06	1.34 ± 0.19
GRB060729	0.540	1.100	-0.87 ± 0.08	-0.45 ± 0.08	0.59 ± 0.11
GRB060908	1.884	0.640	-0.58 ± 0.08	0.07 ± 0.05	2.62 ± 0.32
GRB060927	5.470	0.510	-0.67 ± 0.11	0.50 ± 0.07	13.03 ± 2.19
GRB061007	1.261	0.050	-0.79 ± 0.05	0.57 ± 0.01	0.79 ± 0.12
GRB061021	0.346	0.160	-0.50 ± 0.10	0.35 ± 0.03	1.21 ± 0.24
GRB061110B	3.440	1.310	-1.05 ± 0.14	-0.24 ± 0.11	3.39 ± 0.85
GRB061121	1.314	0.040	-0.76 ± 0.06	0.83 ± 0.01	1.35 ± 0.27
GRB070110	2.352	1.180	-0.93 ± 0.10	-0.44 ± 0.15	1.42 ± 0.49
GRB070306	1.496	0.180	-0.72 ± 0.09	-0.24 ± 0.03	0.42 ± 0.07
GRB070318	0.840	0.330	-0.71 ± 0.08	-0.43 ± 0.04	0.31 ± 0.04
GRB070411	2.954	0.840	-0.79 ± 0.11	-0.72 ± 0.06	0.66 ± 0.08
GRB070529	2.500	1.070	-0.83 ± 0.20	-0.12 ± 0.11	2.81 ± 0.69
GRB070612A	0.617	0.640	-1.07 ± 0.11	-1.15 ± 0.05	0.07 ± 0.01
GRB071010B	0.947	0.150	-0.54 ± 0.06	0.10 ± 0.02	0.88 ± 0.11
GRB071020	2.145	0.270	-0.85 ± 0.11	1.21 ± 0.04	16.76 ± 2.84
GRB071031	2.692	0.990	-0.64 ± 0.17	-1.05 ± 0.11	0.33 ± 0.08
GRB080210	2.641	0.870	-0.97 ± 0.08	-0.33 ± 0.08	1.49 ± 0.26
GRB080310	2.427	0.360	-0.81 ± 0.12	-0.47 ± 0.07	0.51 ± 0.10
GRB080319C	1.950	0.350	-0.76 ± 0.10	0.18 ± 0.04	2.01 ± 0.28

Table 6.1 (cont'd)

| GRB	Redshift	Noise Level	λ	$\log f_{\text{th}}$ Hz	Corrected $f_{\text{th}}(1+z)$ Hz
GRB080413A	2.433	0.230	-0.65 $\pm$ 0.10	0.40 $\pm$ 0.03	3.32 $\pm$ 0.55
GRB080603B	2.690	0.240	-0.62 $\pm$ 0.12	0.67 $\pm$ 0.03	7.12 $\pm$ 1.31
GRB080605	1.640	0.170	-0.60 $\pm$ 0.07	0.88 $\pm$ 0.03	6.92 $\pm$ 0.98
GRB080607	3.036	0.070	-0.71 $\pm$ 0.07	0.56 $\pm$ 0.02	2.22 $\pm$ 0.43
GRB080707	1.230	1.320	-0.91 $\pm$ 0.10	-0.21 $\pm$ 0.12	1.77 $\pm$ 0.49
GRB080710	0.845	1.190	-0.50 $\pm$ 0.15	-0.41 $\pm$ 0.14	0.78 $\pm$ 0.25
GRB080721	2.602	0.060	-0.91 $\pm$ 0.08	0.55 $\pm$ 0.04	0.99 $\pm$ 0.24
GRB080805	1.505	0.580	-0.86 $\pm$ 0.08	-0.89 $\pm$ 0.06	0.20 $\pm$ 0.03
GRB080810	3.350	0.430	-0.88 $\pm$ 0.08	0.23 $\pm$ 0.04	3.52 $\pm$ 0.40
GRB080905B	2.374	0.590	-0.65 $\pm$ 0.17	-0.32 $\pm$ 0.06	1.15 $\pm$ 0.19
GRB081008	1.967	0.390	-0.86 $\pm$ 0.07	-0.58 $\pm$ 0.03	0.35 $\pm$ 0.03
GRB081203A	2.100	0.140	-0.78 $\pm$ 0.08	-0.66 $\pm$ 0.02	0.15 $\pm$ 0.02
GRB081222	2.770	0.120	-0.48 $\pm$ 0.07	0.16 $\pm$ 0.02	1.97 $\pm$ 0.30
GRB090418A	1.608	0.840	-0.63 $\pm$ 0.14	0.05 $\pm$ 0.07	2.62 $\pm$ 0.44
GRB090423	8.200	1.040	-1.60 $\pm$ 0.32	0.22 $\pm$ 0.15	16.26 $\pm$ 5.77
GRB090516	4.109	0.650	-0.94 $\pm$ 0.10	-0.59 $\pm$ 0.08	0.88 $\pm$ 0.17
GRB090812	2.452	0.260	-0.71 $\pm$ 0.07	0.12 $\pm$ 0.04	1.75 $\pm$ 0.22
GRB090926B	1.240	0.320	-0.77 $\pm$ 0.06	-0.79 $\pm$ 0.04	0.15 $\pm$ 0.02
GRB091020	1.710	0.400	-0.55 $\pm$ 0.08	-0.35 $\pm$ 0.03	0.73 $\pm$ 0.08
GRB091024	1.092	0.560	-0.78 $\pm$ 0.08	-0.68 $\pm$ 0.06	0.28 $\pm$ 0.04
GRB091029	2.752	0.560	-0.84 $\pm$ 0.07	-0.50 $\pm$ 0.06	0.73 $\pm$ 0.10
GRB091127	0.490	0.460	-0.82 $\pm$ 0.08	0.91 $\pm$ 0.06	6.41 $\pm$ 0.99
GRB091208B	1.063	0.360	-0.88 $\pm$ 0.09	0.41 $\pm$ 0.04	2.16 $\pm$ 0.30
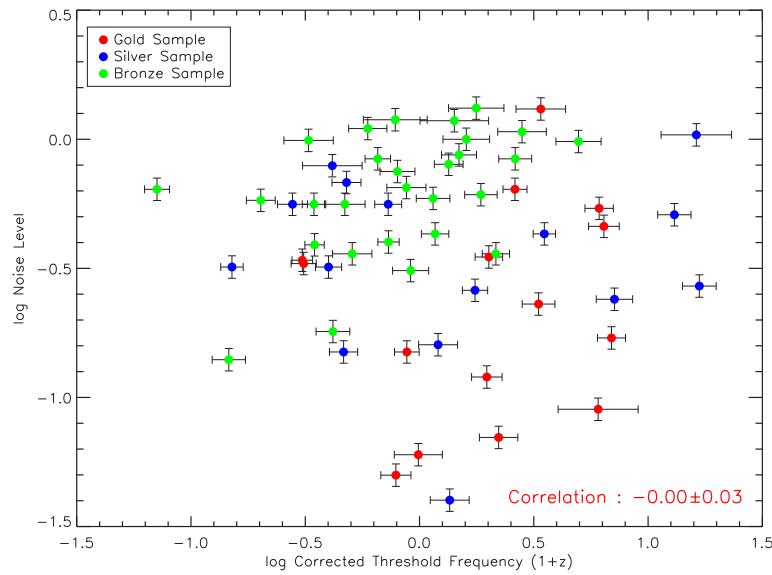
Figure 6.16 The noise-corrected, redshift-corrected threshold frequency versus noise level.
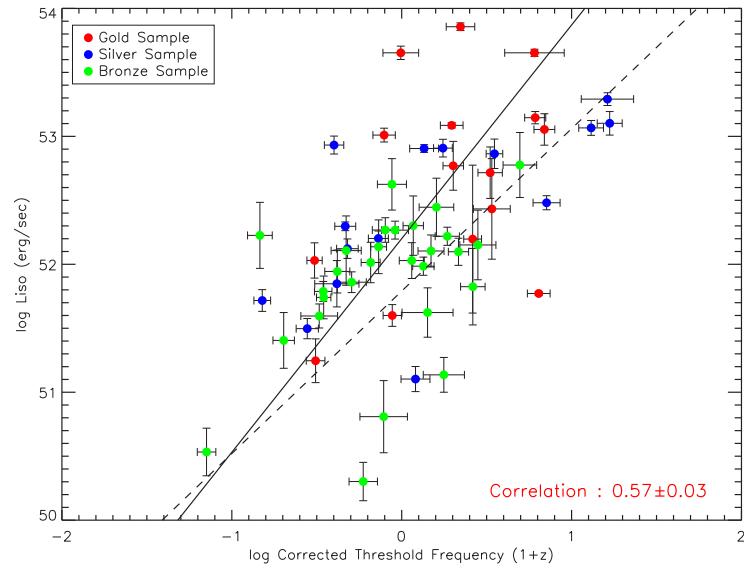

Figure 6.17 The noise-corrected, redshift-corrected threshold frequency versus isotropic peak luminosity. The correlation coefficient between the two parameters is 0.57 ± 0.03. The solid line shows the best-fit power-law with a index of 1.67 ± 0.01. The dashed line shows the best-fit from Figure 6.7.

Table 6.2 Correlation coefficients

Coefficient Type	Correlation Coefficient	Null Probability
Pearson's r	0.57±0.03	1.42×10^{-5}
Spearman's r_s	0.58±0.04	1.72×10^{-6}
Kendall's τ	0.43±0.03	2.03×10^{-6}

We show in Figure 6.17 the noise-corrected threshold frequency - luminosity relation. As is evident, the relation survives the noise correction albeit with a somewhat smaller correlation coefficient of 0.57±0.03. Various correlation coefficients of the relation are shown in Table 6.2, where the uncertainties were obtained through a Monte Carlo simulation. The null probability that the correlation occurs due to random chance is also given for each coefficient type.

The new best-fit is shown as a solid line in Figure 6.17 yielding the following relation between L_iso and $f_\mathrm{th[NL=1]}$:

$$\log L_\mathrm{iso} = (52.2 \pm 0.1) + (1.67 \pm 0.01) \log(f_\mathrm{th}(z+1)). \tag{6.8}$$

The uncertainties in the fitted parameters are expressed with the factor of $\sqrt{\chi^2/\mathrm{ndf}} = \sqrt{1255/56} \approx 5.0$.

6.6 Summary

In this chapter we have analyzed PDS of 206 GRBs. We fitted each PDS with a simple power-law and determined the red-noise exponent and the threshold frequency where white noise begins. For a subset of GRBs, we extracted a frequency-luminosity relationship. For this sample, we treated all bursts on an equal footing by determining a common noise level, thereby minimizing the potential observational biases. We summarize the main results of our analysis as follows:

- The distribution of the extracted α (slope of the red-noise component) values peaks around -1.4 and that of f_th around 1 Hz.

- The dispersion in the distribution of α is large and so the Kolmogorov index of -5/3 is accommodated by our analysis.

- The distribution of the redshift-corrected threshold frequency shows a large dispersion

and is non-gaussian in shape.

- Evidence is presented for a possible frequency-luminosity relationship, i.e., the redshift-corrected f_{th} is correlated with the isotropic luminosity. The correlation coefficient is 0.57 ± 0.03 and the best-fit power-law has an index of 1.67 ± 0.01. We appreciate that in reality there may be complicated underlying interrelationships involving peak photon flux, f_{th}, and redshift and therefore the evidence for the frequency-luminosity relation should be considered tentative.

- The proposed frequency-luminosity correlation, if confirmed, may serve to provide a measure of the intrinsic variability observed in GRBs.

Chapter 7

Hurst Rescale Range Analysis of GRBs

7.1 Introduction

GRB light curves show very complex temporal structures, which almost look like *fractals*. A fractal is a structure that is composed of sub-structures that resemble the larger structure. This is a property referred to as *self-similarity*. Fractals or self-similar structures do not have a single characteristic length scale. They look similar in different length scales and scale with the same scaling factor in all dimensions. It is also possible to extend this fractal concept to time series that lack a single time scale. These types of time series are called *self-affine* records.

Quantitatively, the self-affiness can be defined in terms of a parameter called the Hurst exponent (H). Let $R(t)$ be a time profile that results from a stochastic process. We rescale the time profile with a scaling factor, c, and the rescaled time profile is $R(ct)$. After the rescaling the two profiles are related to each other as follows.

$$R(t) = c^{-H} R(ct) \tag{7.1}$$

Note that if $H = 1$ then $R(t)$ is self similar.

There are a number of methods to extract the value of H for a given time series. In this chapter, we will utilize a method called Hurst Rescale Range Analysis (or R/S analysis) to

extract H values for a sample of long GRBs and investigate long-term correlations.

7.2   Hurst Rescale Range Analysis

The Hurst rescaled range analysis (Hurst, 1951; Feder, 1988; Gammel, 1998) is an effective method to detect correlations in time series measurements. Historically, Hurst was interested in measuring the long-term variation in water levels in lakes and rivers. He devised the rescaled range statistic (the details of which are given below) to quantify these variations. More recently, the technique has found application in many areas of applied physics and mathematics including fractals, chaos theory, and long-memory processes.

The approach is based on calculating the range of variations (in a time series), R, and normalizing this range with the standard deviation, S, obtained from the analysis of all subintervals of data partitioned over the complete range of the data set. The R/S statistic for an evenly binned time series ξ_i is defined as follows: With s as one of the sequential indices on ξ_i, define

$$\langle \xi \rangle_s = \frac{1}{s} \sum_{i=1}^{s} \xi_i, \tag{7.2}$$

$$X(t, s) = \sum_{u=1}^{t} (\xi_u - \langle \xi \rangle_s), \tag{7.3}$$

$$R(s) = \max X(t, s) - \min X(t, s), \;\; \text{where } 1 < t < s, \tag{7.4}$$

$$S(s) = \left[\frac{1}{s} \sum_{t=1}^{s} (\xi_t - \langle \xi \rangle_s)^2 \right]^{\frac{1}{2}}, \tag{7.5}$$

and

$$R'(s) = R(s)/S(s). \tag{7.6}$$

Hurst and others have shown that many natural phenomena follow an empirical power-law: $R/S \sim s^H$, for large $\sim s$, where H is the Hurst exponent. Mandelbrot and Wallis (1969) have linked the range analysis technique to a class of problems and/or processes involving random fluctuations such as those pertaining to Fractal Brownian Motion (Feder, 1988). Indeed, analyses of such processes indicate that a Hurst exponent of 0.5 represents

completely random and uncorrelated behavior with no stochastic memory in time. Furthermore, values of $H > 0.5$ are associated with processes involving correlated behavior or persistence with time, while those with $H < 0.5$ indicate an anti-persistence with time. The Hurst exponent, H, is also directly related to the fractal dimension, D, via the relation $D = 2 - H$.

7.3   A Test Case: Classical Brownian Motion
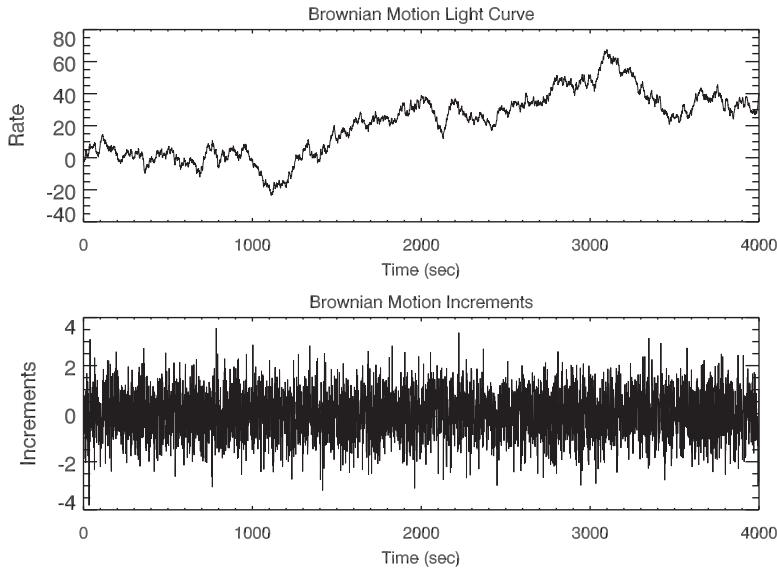
Figure 7.1 Top panel shows a synthetic light-curve that follows Brownian motion. The bottom panel shows the incremental steps in the light-curve.

In order to test and illustrate the application of the rescaled range analysis technique, we apply it to synthetic light curves that follow Brownian motion. We use the pseudo random number generator `randomn()` in the IDL[1] data analysis package to generate 1000 light curves with 4000 data points each. Figure 7.1 shows one such generated light curve: The top panel shows the rate as a function of time and the bottom panel shows increments at each point as a function of time. We note that the increments have a Gaussian distribution with mean zero and a standard deviation of one. For classical Brownian motion (and other processes that depict uncorrelated events with no stochastic memory in time), we expect to

---

[1]Interactive Data Language
http://www.ittvis.com/ProductServices/IDL.aspx

obtain $H \sim 0.5$ or $D \sim 1.5$.

We apply the R/S technique to the increments of the light curve as opposed to the light curve itself (as noted by Feder (1988)). Figure 7.2 shows the R/S statistic versus Time (Time $= s \times$ Time bin size) on a log-log scale. A least-squares fit to the data yields a Hurst exponent of ~ 0.5. In Figure 7.3 we display a histogram of H values extracted from a sample of 1000 synthetic light curves. As expected for Brownian motion, a clear peak around 0.53 ± 0.08 is observed.
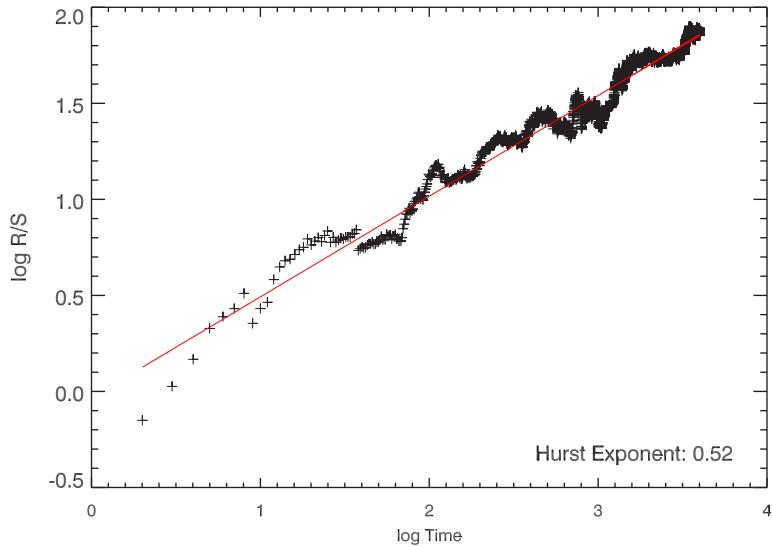
Figure 7.2 The R/S statistic for the Brownian-motion increments plotted as a function of time on a log–log scale. The slope of the best-fit line is the Hurst exponent and gives a value ~ 0.5.

7.4   R/S Analysis of GRBs

BAT light curves can be time binned down to ~ 0.1 ms. However, since various GRBs have durations ranging from a fraction of a second to a few hundred seconds, in this analysis we adopted a policy where we change the binning in powers of two (2^i ms where $i =$0,1,2,...,10) and a given light curve must have at least 4000 data points within T100, a time duration in which the total fluence of the GRB is accumulated. If a given GRB does not have at least 4000 points with the smallest binning of 1 ms then that particular GRB is not included in the sample. Out of 451 GRBs which triggered $Swift$ BAT from 2004 December 19 to 2009
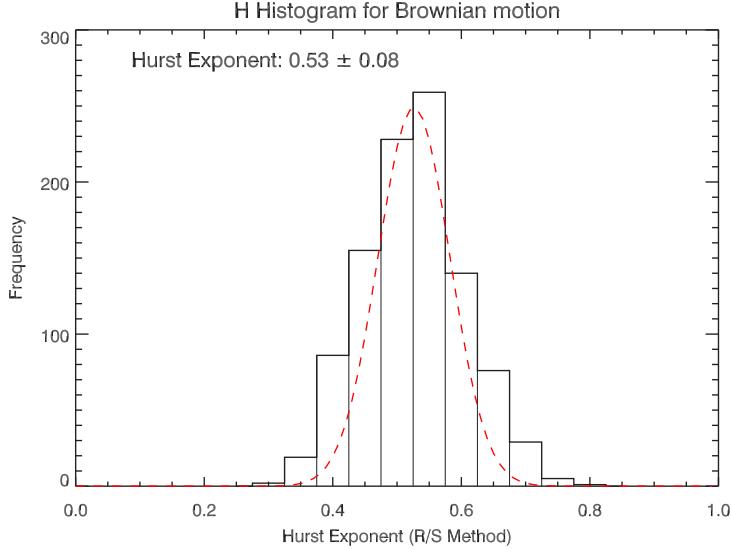
Figure 7.3 Hurst Exponents obtained (using the R/S method) for a sample of 1000 simulated Brownian-motion time series. As expected (for uncorrelated events), the distribution peaks around 0.53 ± 0.08.

December 31, we selected a sample of 396 long GRBs, using the afore mentioned criteria.

We have calculated the R/S statistic for all the bursts in the sample. In Figures 7.4-7.5 we display light curves (for number of GRBs) and the calculated R/S statistic, illustrating the degree to which scaling is either present or not present in the selected GRBs. In Figure 7.4 (GRB 060413), the R/S statistic clearly shows a power-law behavior (or scaling) for a significant portion of the light curve. We also note that the first few data points of the R/S statistic do not lie in the scaling region. This is consistent with the observations of Hurst and others that the R/S method may only be valid for large s (time index). Indeed, application of the Hurst analysis in other fields have shown that this feature is quite general and authors have suggested that in order to extract robust Hurst exponents one needs to have a sufficiently large time series (> 500 points). A linear fit to the data in the scaling region yields a Hurst exponent of 0.16. For GRB 060418, the R/S statistic (see Figure 7.5, bottom panel) shows a sizable structure in addition to a scaling region. The structure (the transition region where the slope of R/S statistic changes dramatically) appears approximately around 110 seconds. This transition region in the R/S statistic is associated with the sharp narrow pulse that appears in the light curve around $T \sim 110$ seconds (see Figure 7.5, top panel). Even for this burst it is possible to extract a reliable

104
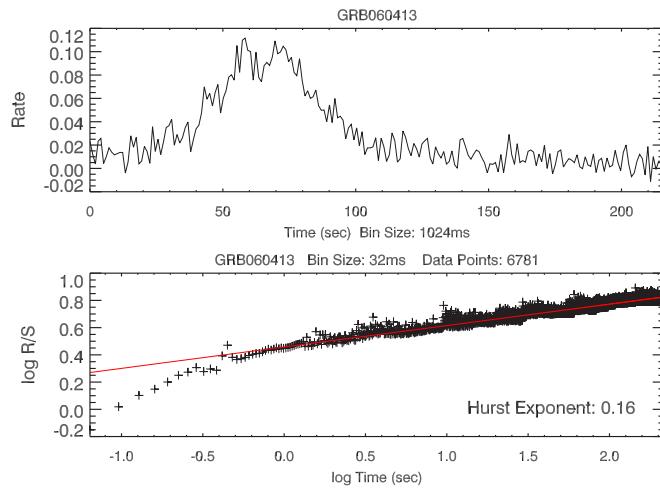
Figure 7.4 The light curve (top panel) and the R/S statistic as a function of time (bottom panel) for GRB 060413. A clear scaling region can be seen after ~ 1 seconds and yields a Hurst exponent of 0.16.
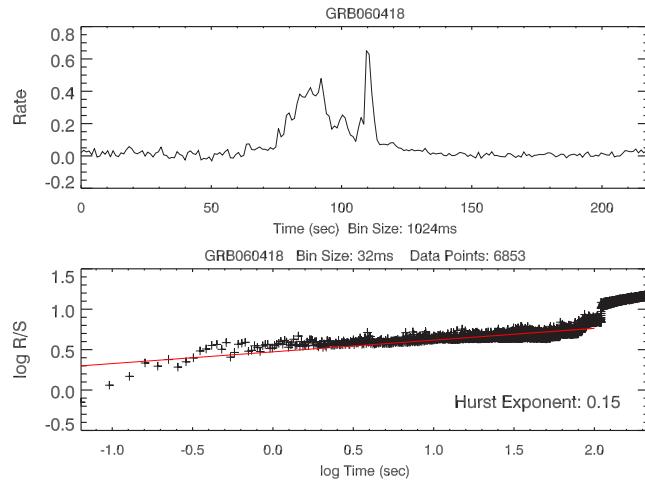

Figure 7.5 The light curve (top panel) and the R/S statistic as a function of time (bottom panel) for GRB 060418. A scaling region can be seen below ~ 100 seconds and yields a Hurst exponent of 0.15.
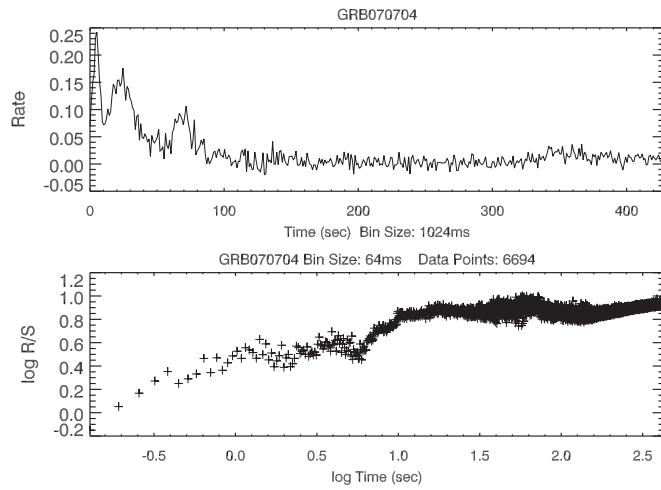
Figure 7.6 The light curve (top panel) and the R/S statistic as a function of time (bottom panel) for GRB 070704. No clear scaling region can be seen.
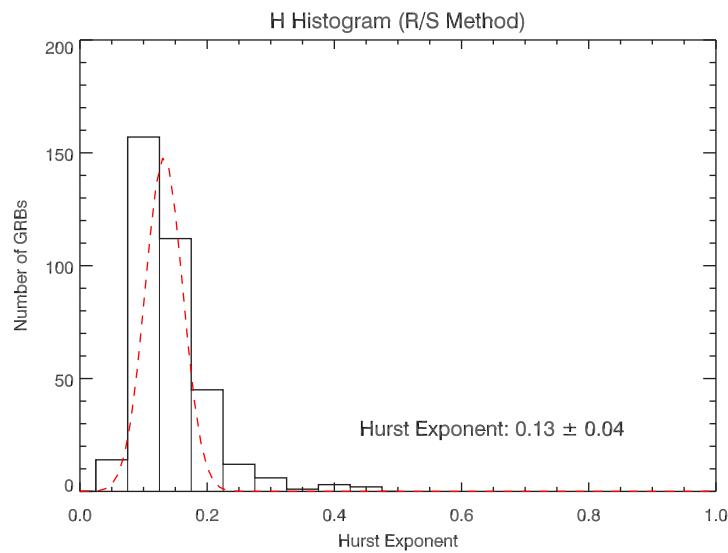
Figure 7.7 Histogram of Hurst Exponents of light curve deviations for 352 GRBs using the rescaled range analysis technique.

Hurst exponent by fitting the scaling region $T \sim 1$ to $T \sim 110$ seconds. The extracted H (0.15) is in good agreement with that obtained from GRB 060413. Finally, we show in Figure 7.6 an example (GRB0 70704) where the expected power-law behavior of the R/S statistic is not immediately obvious. This burst and others like it that have sharp and multiple pulses in their respective light curves introduce structures in the R/S statistic, which in turn, makes the extraction of the H exponents rather questionable. After visual inspection of the R/S statistic for each GRB in our sample, we removed 44 bursts that were not easily described by a single power-law. Hence, our final sample consists of 352 long GRBs.

We extracted the Hurst exponent using the rescaled-range analysis method for our final sample. A histogram of the Hurst exponents obtained using the R/S method is shown in Figure 7.7. The histogram show a relatively narrow peak around $H \sim 0.13 \pm 0.04$ indicating anti-persistent behavior.

An anti-persistent time series reverses itself more often than a random series would. In other words, anti-persistence is the tendency to specifically avoid repeating patterns.

7.5   Summary

In this chapter, we probed long-term correlations in the prompt emission of GRBs by utilizing the Hurst rescaled range analysis method. This method enabled us to extract a parameter called the Hurst exponent, H, which characterizes long-term behavior in the light curves.

A Hurst exponent of 0.5 is indicative of processes that exhibit uncorrelated behavior. Values of $H > 0.5$ are associated with processes involving persistence with time, while those with $H < 0.5$ indicate an anti-persistence with time. The results of our analysis are summarized below.

- We have analyzed 352 $Swift$ long GRBs using the Hurst rescaled range analysis technique.

- Our analysis shows that the Hurst exponents for GRBs peak around ~ 0.13.

- A H value of around ~ 0.13 indicates that long GRBs exhibit anti-persistence.

Chapter 8

Discussion

In this thesis we have investigated spectral lag and variability of Swift BAT GRBs. In the process we have discovered a potentially new correlation between isotropic luminosity and the noise-crossing threshold frequency of the FFT power spectrum. We also present evidence indicating that GRBs show anti-persistent behavior. In this chapter we will discuss possible implications of our findings.

8.1 Spectral Lags: Observer-frame versus Source-frame

In chapter 5 we extracted spectral lags in fixed energy bands in the observer-frame and also fixed energy bands in the source-frame. In the observer-frame case we had four energy channels (canonical BAT energy bands: channel 1 (15–25 keV), 2 (25–50 keV), 3 (50–100 keV) and 4 (100–200 keV)), thus six lag extractions per burst. It is interesting to study to what degree these different lags correlate with source-frame lags (between fixed source-frame energy channels 100–150 keV and 200–250 keV). In Figure 8.1 we show all combination of observer-frame lags as a function of source-frame lags. The black data points show lags without the redshift correction and red data points show lags with the redshift correction. From Figure 8.1 it is clear that all plots show some correlation both in redshift corrected (shown in red) and redshift uncorrected (shown in black) cases. We note that the correlation coefficients are greater than 0.5 in redshift uncorrected cases where BAT channel 1 is involved in the lag extraction. In the redshift corrected case all plots show correlation coefficients greater than 0.5 except the Lag43 plot. Despite these relatively high correlation coefficients there is large scatter in all the plots. This is likely due to energy

Table 8.1. KS test results comparing lag values obtained in the source-frame with that obtained between various BAT energy channels.

Lag Type (Channels)	D statistic	Probability
Lag 21	0.161	0.778
Lag 31	0.323	0.062
Lag 41	0.452	0.002
Lag 32	0.194	0.559
Lag 42	0.323	0.062
Lag 43	0.129	0.944

crossover effects in the observer-frame channels because of the redshift dependence.

Figure 8.2 depicts the lag distributions corresponding to all channel combinations in the fixed observer-frame energy channels. Black and red histograms correspond to redshift uncorrected and corrected cases respectively. Here we note that the redshift uncorrected lag values show relatively large dispersion compared with redshift corrected lag values. In the source-frame case also we see a similar behavior in the extracted lag values (see Figure 8.3). This behavior is a direct result of the time dilation due to cosmological redshift.

It is also of interest to see how the shift from fixed observer-frame energy bands to fixed source-frame energy bands effects the lag distribution. In essence, by using this frame transformation we have bypassed the so called k-correction (see section 5.5.4). Figure 8.4 shows a comparison of distributions of spectral lags extracted between fixed observer-frame energy bands and fixed source-frame energy bands. All lags are corrected for cosmological time dilation. The blue histograms correspond to observer-frame lags while the red histograms correspond to source-frame lags. It would appear that observer-frame lags between consecutive energy bands (i.e. Lag21, Lag 32, and Lag43) show similar distributions to those in the source frame. Conversely, bands which have a gap (i.e. Lag31, Lag41, and Lag42) show dissimilar distributions (see Table 8.1 for K-S test results).
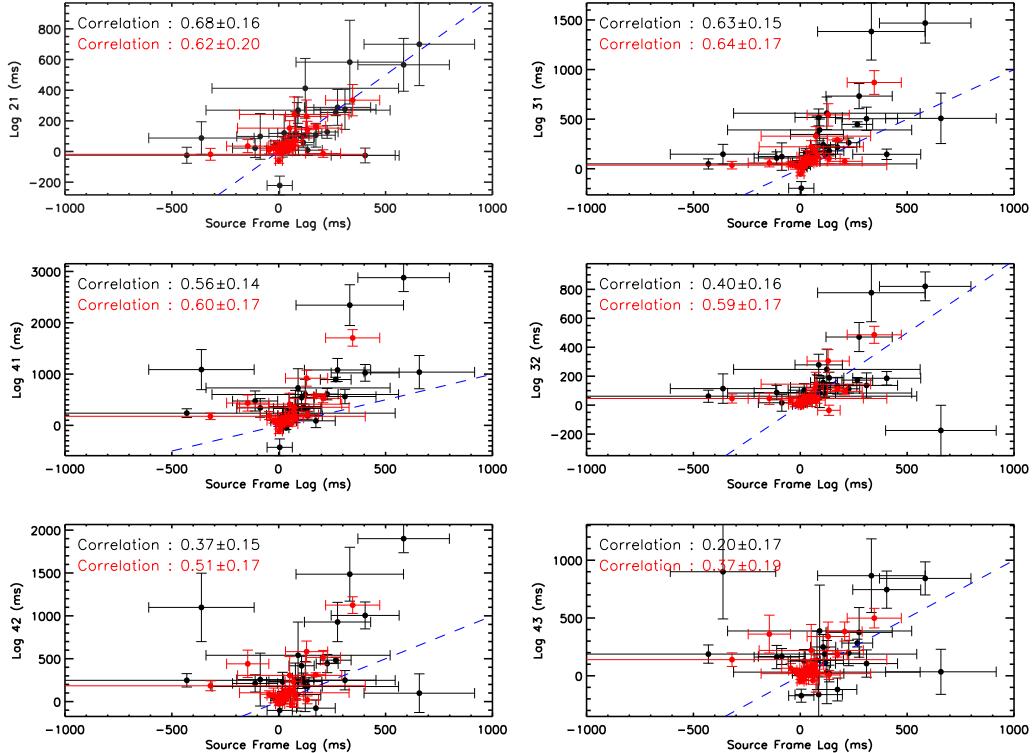
Figure 8.1 All combinations of fixed observer-frame energy channel (canonical BAT energy bands: channel 1 (15–25 keV), 2 (25–50 keV), 3 (50–100 keV) and 4 (100–200 keV)) spectral lag values as a function of fixed source-frame energy channel (between 100–150 keV and 200–250 keV) lag values (for a sample of 31 GRBs). Black and red data points and labels corresponds to redshift uncorrected and corrected cases respectively. The blue dashed line corresponds to the equality line of the two parameters in each panel.
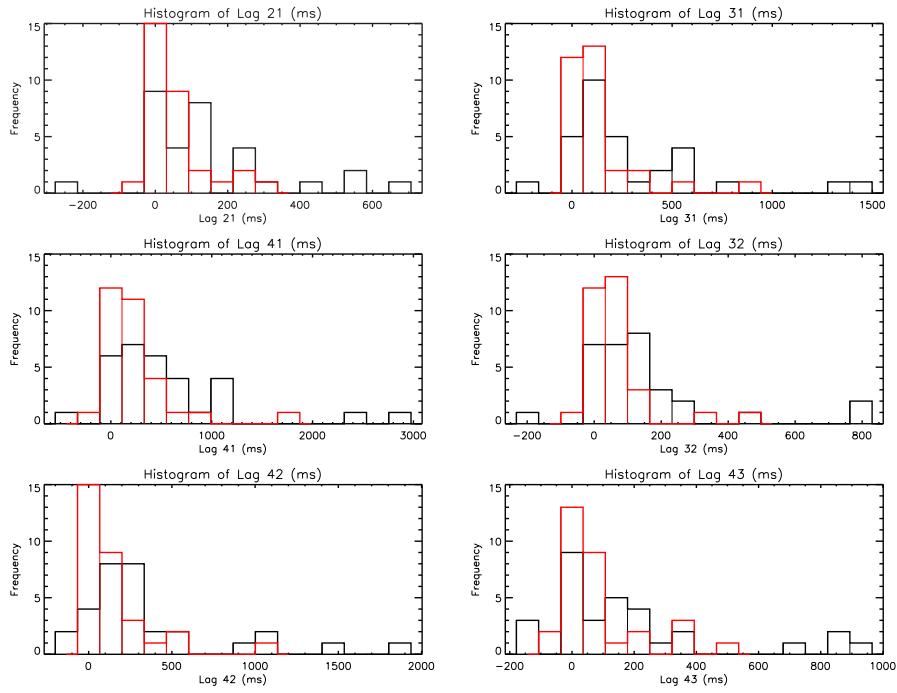
Figure 8.2 The distribution of spectral lag values extracted between fixed observer-frame energy bands. The black histograms show redshift uncorrected case while the red histograms show redshift corrected case.
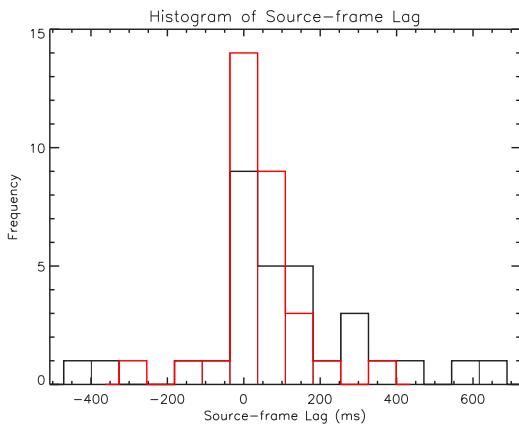

Figure 8.3 The distribution of spectral lag values extracted between fixed source-frame energy bands. Black histogram shows redshift uncorrected case while red histogram shows redshift corrected case.
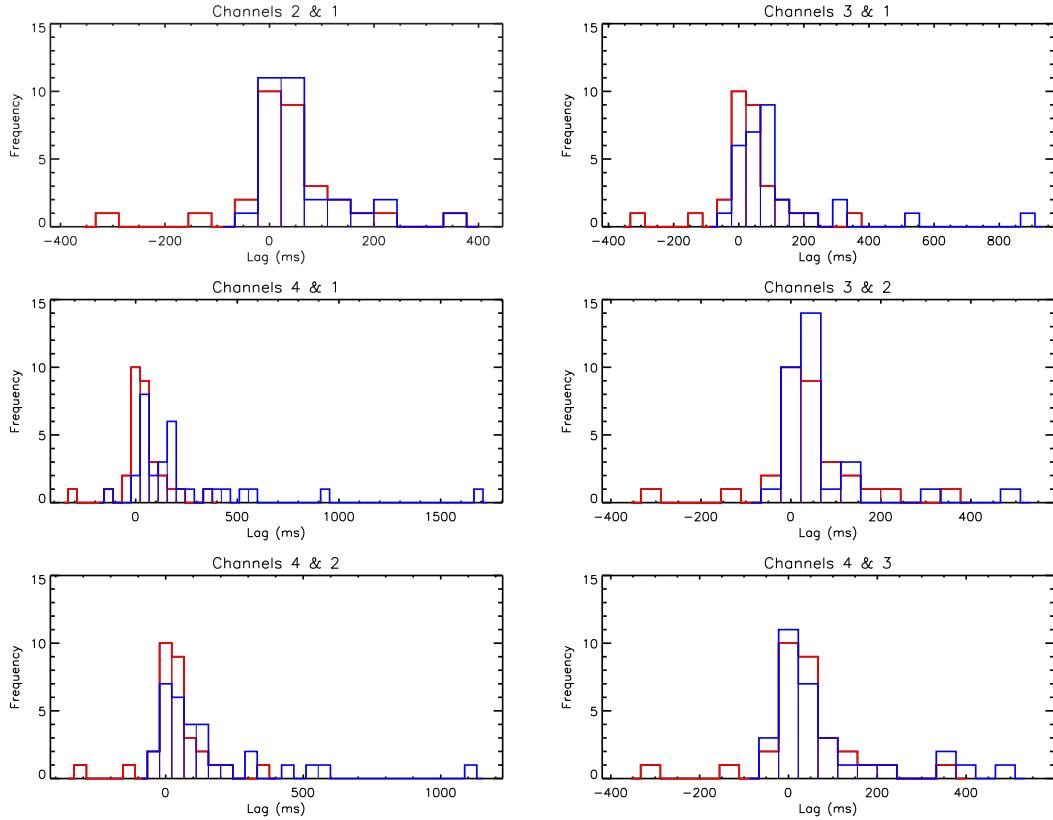
Figure 8.4 A comparison of distributions of spectral lag values extracted between fixed observer-frame energy bands and fixed source-frame energy bands. All lag values are corrected for cosmological time dilation. The blue histograms correspond to observer-frame lags while the red histograms correspond to source-frame lags.

8.2 Spectral Lag - E_{p} Relation

We found in section 5.6.2 that in the source frame $L_{\mathrm{iso}} \propto (Lag/(1+z))^{-1.6}$. If we assume that the Yonetoku relation holds for $Swift$ bursts then $L_{\mathrm{iso}} \propto (E_{\mathrm{p}}(1+z))^{2.0}$ (see Appendix A). Hence, from these two relations we expect to see a correlation between $E_{\mathrm{p}}(1+z)$ and $Lag/(1+z)$ such as $E_{\mathrm{p}}(1+z) \propto (Lag/(1+z))^{-0.8}$.
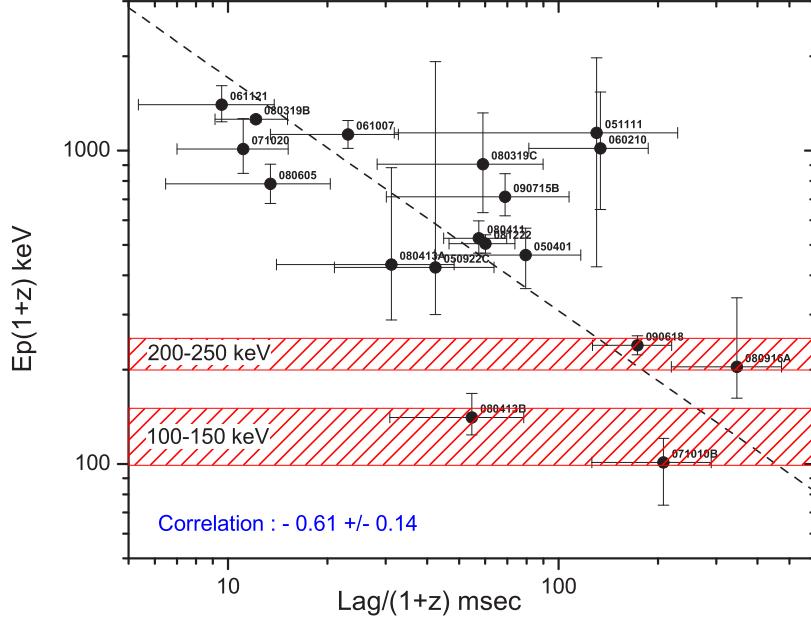

Figure 8.5 The source-frame peak energy (E_p) versus source-frame spectral lag. The fixed source-frame energy bands, $100-150$ keV and $200-250$ keV, are shown in hashed red bands on the plot.

In order to investigate this we plotted source-frame average E_{p} as a function of source-frame lags as shown in Figure 8.5. Clearly there is a correlation between these two parameters with correlation coefficient of -0.61 ± 0.14. The best-fit is shown as a dashed line in Figure 8.5 yielding the following relation between $E_{\mathrm{p}}(1+z)$ and $Lag/(1+z)$:

$$\log E_{\mathrm{p}}(1+z) = (4.0 \pm 0.2) - (0.7 \pm 0.1) \log(Lag/(1+z)). \qquad (8.1)$$

The uncertainties in the fitted parameters are expressed with the factor of $\sqrt{\chi^2/\mathrm{ndf}} = \sqrt{35.15/16} \approx 1.5$.

The best fit slope of 0.7 ± 0.1 is consistent with the expected slope of ~ 0.8 based on the source-frame lag-luminosity and the Yonetoku relation.

8.3 Testing Spectral Lag and Lag-Luminosity Relation Models

In chapter 5, we have provided more evidence for the existence of the lag-luminosity relation based on a sample of $Swift$ BAT data with measured spectroscopic redshifts. The physical origin of the spectral lag and the lag luminosity relation is far from understood. In the literature, several possible interpretations have been discussed (Salmonson, 2000; Ioka and Nakamura, 2001; Kocevski and Liang, 2003; Schaefer, 2004; Ryde, 2005; Shen et al., 2005; Lu et al., 2006). In this section we discuss some of these models and compare with our results.

8.3.1 Spectral Evolution
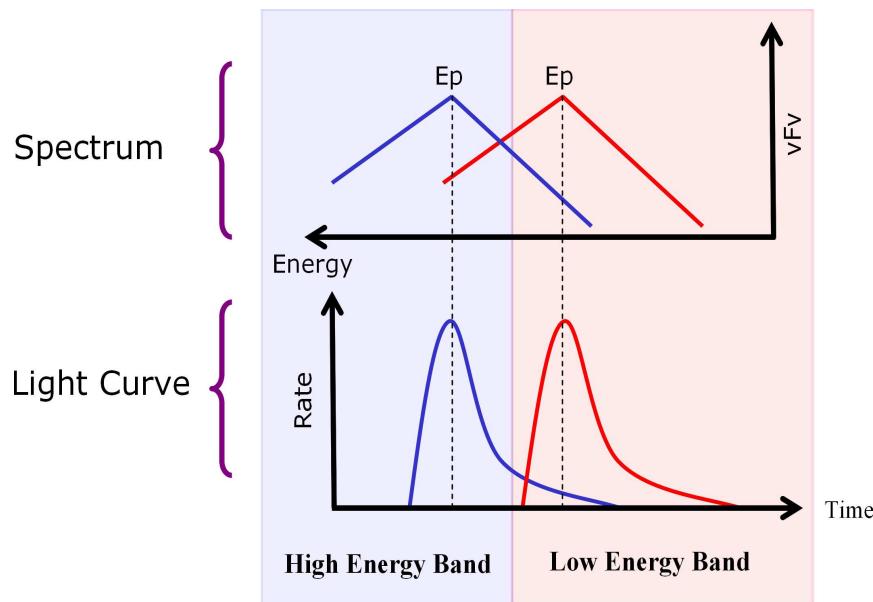
Figure 8.6 The time evolution of the E_{p} across energy bands may cause the observed spectral lag in GRBs.

One proposed explanation for the observed spectral lag is the spectral evolution during the prompt phase of the GRB (Kocevski and Liang, 2003; Ryde, 2005). When the peak energy (E_{p}) moves from a higher energy band to a lower energy band, the temporal peak of the light curve also moves from higher energy band to a lower one, which results in the observed spectral lag. A schematic diagram showing this scenario is shown in Figure 8.6.

114

Initially, E_p of the spectrum is in the high-energy band, which results in a pulse in the light curve of the high energy band. Due to some cooling effect, E_p moves to a lower energy channel after some cooling time. This will cause a pulse in the low-energy light curve. The temporal difference between the two pulses in the light curves would then be a measure of the cooling time scale of the spectrum.

If this is the only process that causes the lag then one would expect the source-frame average E_p to lie within the two energy bands in question. According to Figure 8.5 for the majority of bursts, the source-frame E_p lies out side the energy band $100 - 250$ keV, indicating that the simple spectral evolution scenario described above may not be the dominant process causing the observed lags. In addition, the calculated cooling times based on simple synchrotron models (see section 3.2.3) are in general relatively small compared to the extracted lags. However, it is worth noting that a pulse in a specific energy band may not always mean that the E_p is also within that energy band. Hence our results do not rule out all the models based on spectral evolution.

8.3.2 Curvature Effect

The leading model to explain the spectral lag is the curvature effect or the kinetic effect due to the observer looking at an increasingly off axis annulus area relative to the line-of-sight (Salmonson, 2000; Ioka and Nakamura, 2001; Shen et al., 2005; Lu et al., 2006). Figure 8.7 illustrates how the spectral lag could arise due to the curvature effect of the shocked shell. Here the comoving emissivity of the shell is assumed to be uniform throughout the shell. Softer low-energy radiation comes from the off axis annulus area due to smaller Doppler factors.

Following a similar derivation to Zhang et al. (2009), the path difference between an on-axis photon and an off-axis photon is $\Delta R = R(1 - \cos\theta)$. Here R is the radius of the shell and θ is the jet angle (see Figure 8.7). Hence, the off-axis photons get delayed by a time, t, at the observer-frame,

$$t \sim (1+z)\frac{R}{c}(1 - \cos\theta) \ \rightarrow \ dt = (1+z)\frac{R}{c}d(-\cos\theta). \tag{8.2}$$

The observed energy of the photons (E) is related to the emitted energy (E') of the comoving

Relativistically Expanding Shell

R

GRB

$\theta \sim \dfrac{1}{\Gamma}$

ΔR

**Doppler Factor** $\boxed{D = \dfrac{1}{(1 - v/c\cos\theta)\Gamma}}$
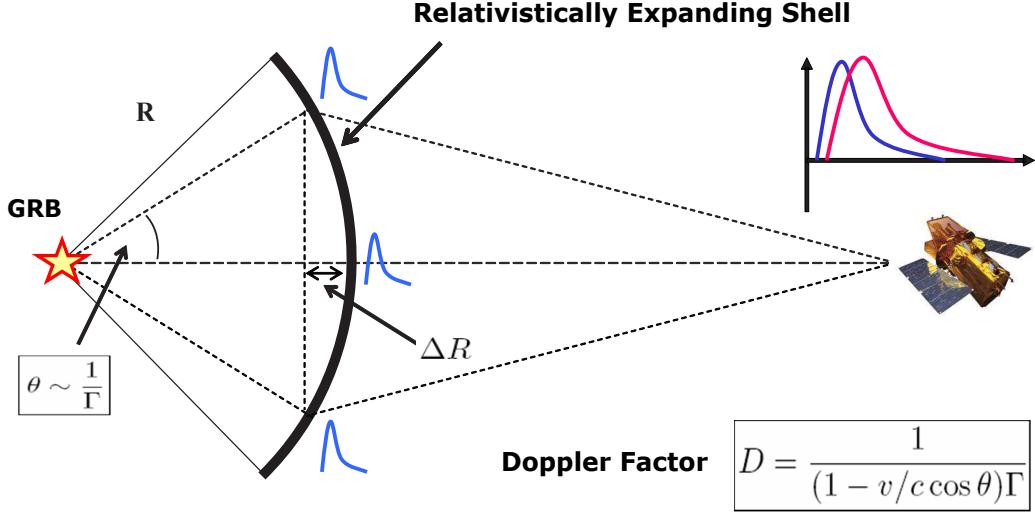
Figure 8.7 Spectral lags could arise due to the curvature effect of the shocked shell.

frame of the shell via the following equation.

$$E = \frac{DE'}{1 + z} \rightarrow dE = \frac{E'}{1 + z} dD \qquad (8.3)$$

Here D is the Doppler factor given below.

$$D = \frac{1}{(1 - \beta\cos\theta)\Gamma} \rightarrow \frac{dD}{d(-\cos\theta)} = \frac{-\beta}{\Gamma(1 - \beta\cos\theta)^2} \qquad (8.4)$$

Here $\beta = v/c$, where v is the bulk velocity of the shell and c is the speed of light. From equations 8.2, 8.3 and 8.4 we get,

$$dE = \frac{E'}{1 + z} dD \rightarrow dE = \frac{E'}{1 + z} \frac{dD}{d(-\cos\theta)} d(-\cos\theta), \qquad (8.5)$$

$$\frac{dE}{dt} = \frac{-cE'\beta}{(1 + z)^2 R\Gamma(1 - \beta\cos\theta)^2}. \qquad (8.6)$$

Hence, the energy dependent lag for the curvature model is given by,

$$\frac{dt}{dE} = -\frac{(1 + z)^2 R\Gamma(1 - \beta\cos\theta)^2}{cE'\beta}. \qquad (8.7)$$

Here the negative sign indicates that high energy photons arrive earlier than the low energy

photons. For the special case $\theta \rightarrow 0$, equation 8.7 simplifies to

$$\frac{dt}{dE} = -\frac{(1+z)^2 R}{4cE'\Gamma^3}.$$ (8.8)

The spectral lag ($\mathrm{Lag}_{E_1}^{E_2}$) between two photons with E_1 and E_2 ($E_1 > E_2$) can be calculated as follows:

$$\mathrm{Lag}_{E_1}^{E_2} = \int_{t(E_1)}^{t(E_2)} dt = -\int_{E_1}^{E_2} \frac{(1+z)^2 R}{4cE'\Gamma^3} \, dE.$$ (8.9)

$$\mathrm{Lag}_{E_1}^{E_2} = \frac{(1+z)^2 R}{4cE'\Gamma^3}(E_1 - E_2)$$ (8.10)

For typical values of $R \sim 3 \times 10^{15}$ cm, $z \sim 2.0$, $\Gamma \sim 100$, $E_1 \sim 200$ keV, $E_2 \sim 50$ keV, and $E' = 80$ keV we get lags ~ 0.4 seconds, which is consistent with the distribution of measured values. However, there are a number of difficulties with this model:

- The curvature model only explains positive lags. Some of the measured lags are negative (about 4% of the lags listed in Table 5.7 are negative at a 1σ level).

- According to the model, the peak flux of the pulse drops rapidly with angle. Hence the model cannot explain the relatively high observed flux in softer energy bands (Zhang et al., 2009).

At the end of the day, spectral lags of GRBs may be caused by multiple mechanisms. But the curvature effect may be responsible for most of the lags seen in GRBs according to the current understanding of GRB physics.

8.4 The Lag-Luminosity Relation for X-ray Flares

An interesting study has been done by Margutti et al. (2010) involving spectral lags. They extracted spectral lags of x-ray flares between x-ray energy channels 0.3-1 keV and 3-10 keV and plotted against the isotropic peak luminosity of the flares. In the same plot they also plotted our lag and luminosity values (Ukwatta et al., 2010) corresponding to gamma-ray energy channels 50-100 keV and 100-200 keV. As shown in Figure 8.8, x-ray flare data also show the same correlation that is observed in the prompt emission light curves.

In their analysis, Margutti et al. (2010) used fixed observer-frame energy bands and obtained $L_{\mathrm{p,iso}}^{0.3-10\mathrm{keV}} \propto t_{\mathrm{lag}}^{-0.95\pm0.23}$ for x-ray flares. On the face of it this slope would appear

to be consistent with the average slope of -1.4 ± 0.3 that we obtained for all six combinations of BAT energy channels. However, if we compare individual matching channels (channels 3 and 4, i.e. 50-100 keV and 100-200 keV; see Figure 5.9), our best-fit yields $L_{\rm p,iso} \propto t_{\rm lag}^{-1.4\pm0.1}$, which is not consistent with the slope obtained by Margutti et al. (2010) for the x-ray flare data. Moreover, for fixed source-frame energy bands the slope of the prompt emission data is -1.6 ± 0.1, which is steeper than any of the slopes obtained in the observer-frame. The inconsistency in the slopes may indicate the onset of physical processes beyond the prompt emission phase.
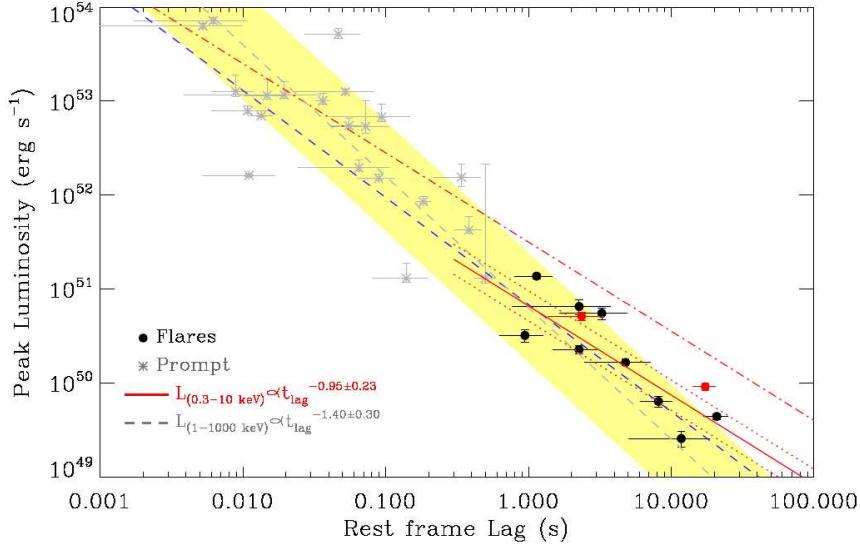

Figure 8.8 The lag-luminosity relation for x-ray flares. The black and red filled circles correspond to x-ray flares. The gray data points are prompt emission values obtained from Figure 5.9. The solid red line is the flare-best-fit corresponding to $L_{\rm p,iso}^{0.3-10\rm keV} \propto t_{\rm lag}^{-0.95\pm0.23}$. The red dotted lines correspond to best-fit sample variance. The black dashed line shows the average slope corresponding to all combinations of fixed observer-frame energy channels. The gray dashed line shows the best-fit line from Figure 5.9 and the yellow shaded area is the 68% confidence region around the fit. For more details see Margutti et al. (2010).

Even though there are inconsistencies in the various slopes, the fact that there is a clear anti-correlation between the luminosity and the lag for prompt emission and for x-ray flares suggests that both phenomena may have a common origin.

8.5 Variability of GRBs

8.5.1 Characteristic Time Scales

Our analysis in Chapter 6 has shown that PDS of a large fraction of GRBs can be described by a simple power-law. The distribution of the power-law indices is essentially Gaussian in shape and peaks around -1.4 ± 0.6. This value is consistent with the findings of Beloborodov et al. (2000) where they find a power-law index or slope of -1.67 (-5/3) with averaged PDS extracted from BATSE data. These authors note that the slope of -5/3 is consistent with the Kolmogorov spectral index expected from processes involving turbulent flow.

In general, the slope of a PDS is indicative of the underlying processes that are responsible for a given time series. For example, a time series that traces pure Brownian motion will produces a PDS with a slope of -2. The fact that a large fraction of bursts show a power-law behavior indicates scaling or self-similar nature of GRBs. This implies that GRBs look the same in a given range of time scales. Unfortunately, extraction of characteristic time scales from the temporal behavior of light curves is a non-trivial task.

Using a sample of BATSE bursts and a technique based on wavelets, Walker et al. (2000) claim that GRBs exhibit a minimum variability time scale of ~ 1 ms. Since the PDS represents the distribution of power over a frequency range, the threshold frequency can be interpreted as a measure of the minimum frequency at which measurable power exists. By converting this threshold frequency to the time domain, one can get an estimate of the upper limit of the variability time of the signal. For our sample this time scale ranges from ~ 50 ms to ~ 10 seconds, i.e., the upper limit for the variability time scale from our analysis is approximately 50 ms.

8.5.2 Variability and Frequency–Luminosity Relations

The validity of the variability-luminosity relation has been investigated by many authors (Fenimore and Ramirez-Ruiz, 2000; Reichart et al., 2001; Guidorzi, 2005; Guidorzi et al., 2005, 2006; Li and Paczyński, 2006; Rizzuto et al., 2007). There has been considerable dispute about the value of the power-law index of the relation. But the existence of the correlation and the fact that it is a positive correlation remain undisputed. However, the correlation does have a large scatter. It has been suspected that the scatter in the correlation is due to the combination of data from different instruments. Rizzuto et al. (2007), however, with

a homogeneous $Swift$ burst sample, showed that the scatter is intrinsic to the variability-luminosity relation. Rizzuto et al. (2007) also confirmed the best-fit power-law index of 1.7 ± 0.4 obtained by Guidorzi et al. (2006) for the variability-luminosity relation.

The frequency-luminosity relation proposed in chapter 6 shows behavior similar to the variability-luminosity relation. The threshold frequency shows a positive correlation with the isotropic peak luminosity of the burst with relatively large scatter. The best-fit power-law index of the frequency-luminosity relation is 1.6 ± 0.1, which is consistent with that of variability-luminosity relation. One is tempted to ask whether the threshold frequency that one obtains from the power spectrum of a GRB light curve provides an alternative variability indicator.

The classical definition of the variability depends on the method used to obtain the smoothed version of the light curve. Fenimore and Ramirez-Ruiz (2000), Reichart et al. (2001) and Li and Paczyński (2006) have proposed various ways of accomplishing this. The lack of a universally accepted definition for variability is a major shortcoming and poses problems in comparing and evaluating the results of various studies. In contrast, the threshold frequency has a very clear definition and does not depend on any smoothing method. However, it needs to be adjusted for noise-level, which requires a simulation in order to obtain the noise-level slope, λ (see section 6.5 for more details). This extra step might be avoided by noting that in Figure 6.14 the distribution of λ shows a Gaussian distribution and peaks around -0.8. That means that one may adopt $\lambda = -0.8$ for all $Swift$ detected bursts and use equation 6.8 to correct the threshold frequency for the noise level without performing a simulation. Hence, threshold frequency is potentially an alternative variability measure for GRBs with an unambiguous definition and a straightforward procedure for its extraction.

8.6 Long-term correlations in GRB light curves

An estimation of long-term correlations in a time series of data (such as a light curve) is useful to understand the underlying physical processes that created those data. The presence of these correlations implies that there is some measurable characteristic in the data that influences the signal trend over a long time interval. The Hurst rescaled range (R/S) analysis is one method to estimate these correlations in time series data.

Using the Hurst rescaled range (R/S) analysis (see chapter 7), we studied correlations

in the prompt emission of a large sample of long GRBs. We remind the reader that a Hurst exponent of 0.5 is indicative of processes that exhibit uncorrelated behavior. Values of $H > 0.5$ are associated with processes involving persistence with time, while those with $H < 0.5$ indicate an anti-persistence with time. We also note that an anti-persistent time series tends to reverse itself more often than a random series would. In other words, anti-persistence is the tendency to avoid repeating patterns. Our extracted Hurst exponents are very narrowly distributed and exhibit a mean value of 0.13 ± 0.04. This is significantly smaller than 0.5, implying that long GRBs exhibit a high degree of anti-persistence with time. We note here that the R/S method for extracting the Hurst exponent suffers from number of limitations. For example it is known that one needs sufficient data points in the time series in order to extract a robust value (typically greater than 500). We discovered an even more severe limitation that is associated with the presence of narrow spikes in the light curve (see Appendix D for more details).
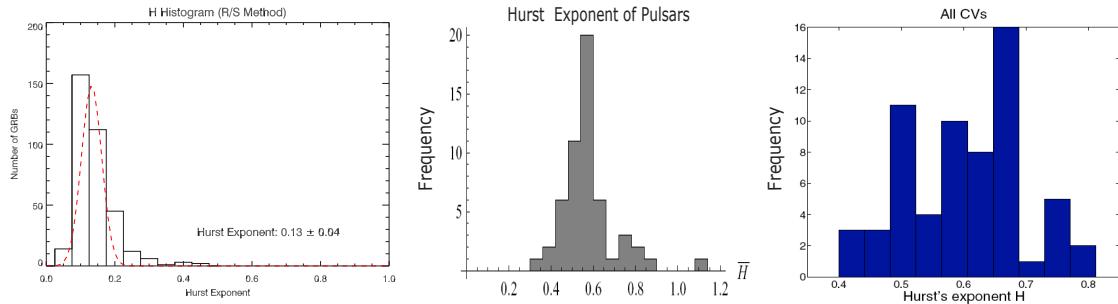

Figure 8.9 Distribution of Hurst exponents for a sample of 352 GRBs (left panel), for a sample of 54 pulsar noise (middle panel; (Na et al., 2009)) and for a sample of 70 CVs (right panel; Fritz and Bruch (1998); Tamburini et al. (2009)).

Having recognized these limitations, we extracted the Hurst exponent using a couple of other techniques: one such method is the technique of box counting (Feder, 1988) and the other one is related to the red-noise slope, α, extracted from the PDS. With box counting one extracts the fractal dimension, D, of the time profile (i.e. the light curve) and relates it to the Hurst exponent via the expression, $H = 2 - D$. In the case of the PDS method, H is extracted from the expression, $H = (\alpha - 1)/2$. Both techniques yield a value of ~ 0.2 for H, but the PDS method leads to a large dispersion in H, which is directly attributable to the large dispersion in the slope parameter, α. Despite the various limitations, the overall value extracted for H is smaller than 0.5, indicative of anti-persistence, i.e., the majority of

GRB light curves result from correlated processes.

By way of comparison, we note that R/S analysis has been reported for a number of astrophysical sources including pulsars and CVs (Cataclysmic Variables). Figure 8.9 shows a distribution of H values of pulsar noise (middle panel) and CVs (right panel). We note that the pulsar noise shows a clear peak around $H \sim 0.5$. This presumably indicates that most of these events are uncorrelated. In the case of the CVs there is also a noticeable peak at $H \sim 0.5$, however, the dispersion in H is actually quite large, with multi-peak structure and an additional pronounced peak around $H \sim 0.68$. In contrast to the pulsar data, the CV data indicate both uncorrelated and correlated behavior. In particular, the peak at $H \sim 0.68$ indicates a high degree of persistence. This high degree of persistence in CVs is potentially linked to the temporal behavior of magnetic fields in these systems (Fritz and Bruch, 1998; Tamburini et al., 2009). Compared to these astrophysical systems, GRBs appear to exhibit anti-persistence . The role of magnetic fields in GRBs is an open question. Unfortunately, the anti-persistent result for H and its potential connection to the magnetic fields in GRBs is not clear at this stage.

Chapter 9

Conclusion

9.1 Summary

During the course of this thesis work, we have investigated spectral lags and variability of GRBs and studied their connection to the luminosity.

9.1.1 Methodology Innovations

We have made significant improvements to the methodology of spectral lag extractions as listed below.

I. Using synthetic light curves with artificially introduced lags, we systematically investigated the effect of various light curve waveforms on the two versions of CCF. We consistently found that the CCF_{Band} (equation 5.2) was better able to recover the introduced lags.

II. We developed criteria to determine the optimal time binning for lag extraction.

III. We used Monte Carlo simulations to estimate the uncertainties in the CCF as well as spectral lags.

IV. For the first time, by using fixed energy bands in the source-frame, we extracted spectral lags, thus making the k-correction unnecessary.

We also significantly improved the PDS extraction methodology as listed below.

I. We used a Monte Carlo simulation utilizing the light curve error bars to estimate uncertainties in the PDS.

II. We used logarithmic frequency binning to obtain the final PDS.

III. We propose a new empirical relation (equation 6.6) to measure the noise-level of a GRB light curve.

IV. We developed a novel method to normalize PDS to a nominal noise-level.

In addition, for the first time, we applied the Hurst rescale-range analysis to GRB data and investigated scaling behavior and long term-correlations of GRBs.

9.1.2 Main Results

The main result of this thesis can be summarized as below.

The Lag-Luminosity Relation

- We have confirmed the lag-luminosity relation in the fixed observer-frame energy bands. The mean value of the correlation coefficient for various channel combinations is -0.68 with a chance probability of $\sim 0.7 \times 10^{-3}$.

- The mean value of the power-law index of the lag-luminosity correlation for fixed observer-frame energy bands is 1.4 ± 0.3.

- We extended the relation to the source frame of the bursts.

- There is a higher degree of correlation of -0.74 ± 0.7 (chance probability of 2.0×10^{-3}) between the spectral lag and the isotropic peak luminosity in the fixed source-frame energy bands.

- The source-frame best-fit power-law gives an index of -1.6 ± 0.1, which is steeper than the index found in the observer-frame case.

GRB Power Spectra and Potentially a New Frequency-Luminosity Relation

- The distribution of the extracted α (slope of the red-noise component) peaks around -1.4 and that of f_{th} around 1 Hz.

- The dispersion in the distribution of α is large and therefore the Kolmogorov index of -5/3 is accommodated by our analysis.

- The distribution of the redshift-corrected threshold frequency shows a large dispersion and is non-gaussian in shape.

- Evidence is presented for a possible frequency-luminosity relationship, i.e., the redshift-corrected f_{th} is correlated with the isotropic luminosity. The correlation coefficient is 0.57 ± 0.03 and the best-fit power-law has an index of 1.67 ± 0.01. We note that in reality there may be complicated underlying interrelationships involving peak photon flux, f_{th}, and redshift and therefore the evidence for the frequency-luminosity relation should be considered tentative.

- The proposed frequency-luminosity correlation, if confirmed, may serve to provide a measure of the intrinsic variability observed in GRBs.

The Hurst Rescaled-Range Analysis of GRBs

- Our analysis shows that the Hurst exponents for GRBs peak around ~ 0.13.

- An H value of around ~ 0.13 indicates that long GRBs exhibit anti-persistence.

- A value of H other than 0.5 indicates that GRBs involve correlated behavior. However, our analysis was not able to extract the time scale over which this correlation exists.

9.2   Future Steps

- Investigate the lag-luminosity relation in different source-frame energy bands using Fermi GBM data.

- Investigate the frequency-luminosity relation using data from other instruments such as Fermi GBM.

- Explore theoretical models that can reproduce the observed details of these relations.

- Investigate long-term correlations in GRBs using other more robust techniques based on wavelets. These techniques offer the possibility of extracting the correlation time scales.

- In addition, one should examine the possibility of probing transitions in H, from anti-persistence to persistence, by studying prompt and afterglow data.

Bibliography

Amati, L., Frontera, F., Tavani, M., in't Zand, J. J. M., Antonelli, A., Costa, E., Feroci, M., Guidorzi, C., Heise, J., Masetti, N., Montanari, E., Nicastro, L., Palazzi, E., Pian, E., Piro, L., and Soffitta, P. (2002). Intrinsic spectra and energetics of BeppoSAX Gamma-Ray Bursts with known redshifts. A.& A., 390:81–89.

Band, D., Matteson, J., Ford, L., Schaefer, B., Palmer, D., Teegarden, B., Cline, T., Briggs, M., Paciesas, W., Pendleton, G., Fishman, G., Kouveliotou, C., Meegan, C., Wilson, R., and Lestrade, P. (1993). BATSE observations of gamma-ray burst spectra. I - Spectral diversity. ApJ., 413:281–292.

Band, D. L. (1997). Gamma-ray burst spectral evolution through cross-correlations of discriminator light curves. *Astrophys. J.*, 486:928.

Barthelmy, S. D., Barbier, L. M., Cummings, J. R., Fenimore, E. E., Gehrels, N., Hullinger, D., Krimm, H. A., Markwardt, C. B., Palmer, D. M., Parsons, A., Sato, G., Suzuki, M., Takahashi, T., Tashiro, M., and Tueller, J. (2005). The Burst Alert Telescope (BAT) on the SWIFT Midex Mission. *Space Science Reviews*, 120:143–164.

Barthelmy, S. D., Baumgartner, W., Cummings, J., Fenimore, E., Gehrels, N., Krimm, H., Markwardt, C., McLean, K., Palmer, D., Sakamoto, T., Sato, G., Stamatikos, M., Tueller, J., and Ukwatta, T. (2008). GRB 080413B, Swift-BAT refined analysis. *GRB Coordinates Network*, 7606:1–+.

Beloborodov, A. M., Stern, B. E., and Svensson, R. (1998). Self-Similar Temporal Behavior of Gamma-Ray Bursts. ApJ. Lett., 508:L25–L27.

Beloborodov, A. M., Stern, B. E., and Svensson, R. (2000). Power Density Spectra of Gamma-Ray Bursts. ApJ., 535:158–166.

Berger, E. (2010). The Environments of Short-Duration Gamma-Ray Bursts and Implications for their Progenitors. *ArXiv e-prints*.

Berger, E. and Becker, G. (2005). GRB 050603: redshift. *GRB Coordinates Network*, 3520:1–+.

Bissaldi, E. and McBreen, S. (2008). GRB 081222: Fermi GBM observation. *GRB Coordinates Network*, 8715:1–+.

Blandford, R. D. and McKee, C. F. (1976). Fluid dynamics of relativistic blast waves. *Physics of Fluids*, 19:1130–1138.

Blandford, R. D. and Znajek, R. L. (1977). Electromagnetic extraction of energy from Kerr black holes. MNRAS, 179:433–456.

Bloom, J. S., Djorgovski, S. G., Kulkarni, S. R., and Frail, D. A. (1998). The Host Galaxy of GRB 970508. ApJ. Lett., 507:L25–L28.

Bloom, J. S., Kulkarni, S. R., and Djorgovski, S. G. (2002). The Observed Offset Distribution of Gamma-Ray Bursts from Their Host Galaxies: A Robust Clue to the Nature of the Progenitors. AJ., 123:1111–1148.

Borgonovo, L., Frontera, F., Guidorzi, C., Montanari, E., Vetere, L., and Soffitta, P. (2007). On the temporal variability classes found in long gamma-ray bursts with known redshift. A.& A., 465:765–775.

Burrows, D. N., Hill, J. E., Nousek, J. A., Kennea, J. A., Wells, A., Osborne, J. P., Abbey, A. F., Beardmore, A., Mukerjee, K., Short, A. D. T., Chincarini, G., Campana, S., Citterio, O., Moretti, A., Pagani, C., Tagliaferri, G., Giommi, P., Capalbi, M., Tamburelli, F., Angelini, L., Cusumano, G., Bräuninger, H. W., Burkert, W., and Hartner, G. D. (2005a). The Swift X-Ray Telescope. *Space Science Reviews*, 120:165–195.

Burrows, D. N., Romano, P., Falcone, A., Kobayashi, S., Zhang, B., Moretti, A., O'Brien, P. T., Goad, M. R., Campana, S., Page, K. L., Angelini, L., Barthelmy, S., Beardmore, A. P., Capalbi, M., Chincarini, G., Cummings, J., Cusumano, G., Fox, D., Giommi, P., Hill, J. E., Kennea, J. A., Krimm, H., Mangano, V., Marshall, F., Mészáros, P., Morris, D. C., Nousek, J. A., Osborne, J. P., Pagani, C., Perri, M., Tagliaferri, G., Wells, A. A., Woosley, S., and Gehrels, N. (2005b). Bright X-ray Flares in Gamma-Ray Burst Afterglows. *Science*, 309:1833–1835.

Butler, N. R., Kocevski, D., Bloom, J. S., and Curtis, J. L. (2007). A Complete Catalog of Swift Gamma-Ray Burst Spectra and Durations: Demise of a Physical Origin for Pre-Swift High-Energy Correlations. ApJ., 671:656–677.

Cannizzo, J. K., Ukwatta, T. N., Palmer, D. M., Margutti, R., and de Pasquale, M. (2009). Swift observations of GRB 090424. *GCN Report*, 221:1–+.

Cenko, S. B., Cucchiara, A., Fox, D. B., Berger, E., and Price, P. A. (2007). GRB 071010B: Gemini spectroscopic observations. *GRB Coordinates Network*, 6888:1–+.

Cenko, S. B., Perley, D. A., Junkkarinen, V., Burbidge, M., Diego, U. S., and Miller, K. (2009). GRB 090618: Lick/KAST spectroscopy. *GRB Coordinates Network*, 9518:1–+.

Cheng, L. X., Ma, Y. Q., Cheng, K. S., Lu, T., and Zhou, Y. Y. (1995). The time delay of gamma-ray bursts in the soft energy band. A.& A., 300:746–+.

Chincarini, G., Mao, J., Margutti, R., Bernardini, M. G., Guidorzi, C., Pasotti, F., Giannios, D., Della Valle, M., Moretti, A., Romano, P., D'Avanzo, P., Cusumano, G., and Giommi, P. (2010). Unveiling the origin of X-ray flares in gamma-ray bursts. MNRAS, 406:2113–2148.

Chornock, R., Perley, D. A., Cenko, S. B., and Bloom, J. S. (2009). GRB 090424 Gemini-South redshift. *GRB Coordinates Network*, 9243:1–+.

Cline, D. B., Matthey, C., Otwinowski, S., Czerny, B., and Janiuk, A. (2007). The Search for Primordial Black Holes Using Very Short Gamma Ray Bursts. *ArXiv e-prints*.

Connaughton, V. (2009). GRB 090424: Fermi GBM observation. *GRB Coordinates Network*, 9230:1–+.

Conselice, C. J., Vreeswijk, P. M., Fruchter, A. S., Levan, A., Kouveliotou, C., Fynbo, J. P. U., Gorosabel, J., Tanvir, N. R., and Thorsett, S. E. (2005). Gamma-Ray Burst-Selected High-Redshift Galaxies: Comparison to Field Galaxy Populations to z ˜ 3. ApJ., 633:29–40.

Costa, E., Frontera, F., Heise, J., Feroci, M., in't Zand, J., Fiore, F., Cinti, M. N., Dal Fiume, D., Nicastro, L., Orlandini, M., Palazzi, E., Rapisarda#, M., Zavattini, G., Jager, R., Parmar, A., Owens, A., Molendi, S., Cusumano, G., Maccarone, M. C., Giarrusso, S., Coletta, A., Antonelli, L. A., Giommi, P., Muller, J. M., Piro, L., and Butler, R. C. (1997). Discovery of an X-ray afterglow associated with the γ-ray burst of 28 February 1997. Nature, 387:783–785.

Cucchiara, A. and Fox, D. B. (2008). GRB 080430: hobby-eberly telescope absorption redshift. *GRB Coordinates Network*, 7654:1–+.

Cucchiara, A., Fox, D. B., Cenko, S. B., and Berger, E. (2008). GRB 081222: gemini-south absorption redshift. *GRB Coordinates Network*, 8713:1–+.

D'Elia, V., Fiore, F., Perna, R., Krongold, Y., Covino, S., Fugazza, D., Lazzati, D., Nicastro, F., Antonelli, L. A., Campana, S., Chincarini, G., D'Avanzo, P., Della Valle, M., Goldoni, P., Guetta, D., Guidorzi, C., Meurs, E. J. A., Mirabel, F., Molinari, E., Norci, L., Piranomonte, S., Stella, L., Stratta, G., Tagliaferri, G., and Ward, P. (2009). The Prompt, High-Resolution Spectroscopic View of the "Naked-Eye" GRB080319B. ApJ., 694:332–338.

Djorgovski, S. G., Kulkarni, S. R., Bloom, J. S., Goodrich, R., Frail, D. A., Piro, L., and Palazzi, E. (1998). Spectroscopy of the Host Galaxy of the Gamma-Ray Burst 980703. ApJ. Lett., 508:L17–L20.

Donaghy, T. Q., Lamb, D. Q., Sakamoto, T., Norris, J. P., Nakagawa, Y., Villasenor, J., Atteia, J. ., Vanderspek, R., Graziani, C., Kawai, N., Ricker, G. R., Crew, G. B., Doty, J., Prigozhin, G., Jernigan, J. G., Shirasaki, Y., Suzuki, M., Butler, N., Hurley, K., Tamagawa, T., Yoshida, A., Matsuoka, M., Fenimore, E. E., Galassi, M., Boer, M., Dezalay, J. ., Olive, J. ., Levine, A., Martel, F., Morgan, E., Sato, R., Woosley, S. E., Braga, J., Manchanda, R., Pizzichini, G., Takagishi, K., and Yamauchi, M. (2006). HETE-2 Localizations and Observations of Four Short Gamma-Ray Bursts: GRBs 010326B, 040802, 051211 and 060121. *ArXiv Astrophysics e-prints*.

Eichler, D., Livio, M., Piran, T., and Schramm, D. N. (1989). Nucleosynthesis, neutrino bursts and gamma-rays from coalescing neutron stars. Nature, 340:126–128.

Feder, J. (1988). *Fractals*. Plenum Press, New York, 1988.

Fenimore, E. E., in 't Zand, J. J. M., Norris, J. P., Bonnell, J. T., and Nemiroff, R. J. (1995). Gamma-Ray Burst Peak Duration as a Function of Energy. ApJ. Lett., 448:L101+.

Fenimore, E. E. and Ramirez-Ruiz, E. (2000). Redshifts For 220 BATSE Gamma-Ray Bursts Determined by Variability and the Cosmological Consequences. *ArXiv Astrophysics e-prints.*

Firmani, C., Ghisellini, G., Avila-Reese, V., and Ghirlanda, G. (2006). Discovery of a tight correlation among the prompt emission properties of long gamma-ray bursts. MNRAS, 370:185–197.

Fox, D. B., Frail, D. A., Price, P. A., Kulkarni, S. R., Berger, E., Piran, T., Soderberg, A. M., Cenko, S. B., Cameron, P. B., Gal-Yam, A., Kasliwal, M. M., Moon, D., Harrison, F. A., Nakar, E., Schmidt, B. P., Penprase, B., Chevalier, R. A., Kumar, P., Roth, K., Watson, D., Lee, B. L., Shectman, S., Phillips, M. M., Roth, M., McCarthy, P. J., Rauch, M., Cowie, L., Peterson, B. A., Rich, J., Kawai, N., Aoki, K., Kosugi, G., Totani, T., Park, H., MacFadyen, A., and Hurley, K. C. (2005). The afterglow of GRB 050709 and the nature of the short-hard γ-ray bursts. Nature, 437:845–850.

Frail, D. A. and al, e. (2001). Beaming in gamma-ray bursts: Evidence for a standard energy reservoir. *Astrophys. J.*, 562:55F.

Frail, D. A., Kulkarni, S. R., Berger, E., and Wieringa, M. H. (2003). A Complete Catalog of Radio Afterglows: The First Five Years. AJ., 125:2299–2306.

Frail, D. A., Kulkarni, S. R., Nicastro, L., Feroci, M., and Taylor, G. B. (1997). The radio afterglow from the γ-ray burst of 8 May 1997. Nature, 389:261–263.

Fritz, T. and Bruch, A. (1998). Studies of the flickering in cataclysmic variables. IV. Wavelet transforms of flickering light curves. A.& A., 332:586–604.

Fruchter, A. S., Levan, A. J., Strolger, L., Vreeswijk, P. M., Thorsett, S. E., Bersier, D., Burud, I., Castro Cerón, J. M., Castro-Tirado, A. J., Conselice, C., Dahlen, T., Ferguson, H. C., Fynbo, J. P. U., Garnavich, P. M., Gibbons, R. A., Gorosabel, J., Gull, T. R., Hjorth, J., Holland, S. T., Kouveliotou, C., Levay, Z., Livio, M., Metzger, M. R., Nugent, P. E., Petro, L., Pian, E., Rhoads, J. E., Riess, A. G., Sahu, K. C., Smette, A., Tanvir, N. R., Wijers, R. A. M. J., and Woosley, S. E. (2006). Long γ-ray bursts and core-collapse supernovae have different environments. Nature, 441:463–468.

Fruchter, A. S., Thorsett, S. E., Metzger, M. R., Sahu, K. C., Petro, L., Livio, M., Ferguson, H., Pian, E., Hogg, D. W., Galama, T., Gull, T. R., Kouveliotou, C., Macchetto, D., van Paradijs, J., Pedersen, H., and Smette, A. (1999). Hubble Space Telescope and Palomar Imaging of GRB 990123: Implications for the Nature of Gamma-Ray Bursts and Their Hosts. ApJ. Lett., 519:L13–L16.

Fynbo, J. P. U., Jakobsson, P., Prochaska, J. X., Malesani, D., Ledoux, C., de Ugarte Postigo, A., Nardini, M., Vreeswijk, P. M., Hjorth, J., Sollerman, J., Chen, H. ., Thoene, C. C., Bjoernsson, G., Bloom, J. S., Castro-Tirado, A., Christensen, L., De Cia, A., Gorosabel, J. U., Jaunsen, A., Jensen, B. L., Levan, A., Maund, J., Masetti, N., Milvang-Jensen, B., Palazzi, E., Perley, D. A., Pian, E., Rol, E., Schady, P., Starling, R., Tanvir, N., Watson, D. J., Wiersema, K., Xu, D., Augusteijn, T., Grundahl, F., Telting, J., and Quirion, P. . (2009). Low-Resolution Spectroscopy of Gamma-ray Burst Optical Afterglows: Biases in the Swift Sample and Characterization of the Absorbers. *ArXiv e-prints.*

Gammel, B. M. (1998). Hurst's rescaled range statistical analysis for pseudorandom number generators used in physical simulations. Phys. Rev. E, 58:2586–2597.

Gaskell, C. M. and Peterson, B. M. (1987). The accuracy of cross-correlation estimates of quasar emission-line region sizes. ApJ. Supp., 65:1–11.

Gehrels, N., Chincarini, G., Giommi, P., Mason, K. O., Nousek, J. A., Wells, A. A., White, N. E., Barthelmy, S. D., Burrows, D. N., Cominsky, L. R., Hurley, K. C., Marshall, F. E., Mészáros, P., Roming, P. W. A., Angelini, L., Barbier, L. M., Belloni, T., Campana, S., Caraveo, P. A., Chester, M. M., Citterio, O., Cline, T. L., Cropper, M. S., Cummings, J. R., Dean, A. J., Feigelson, E. D., Fenimore, E. E., Frail, D. A., Fruchter, A. S., Garmire, G. P., Gendreau, K., Ghisellini, G., Greiner, J., Hill, J. E., Hunsberger, S. D., Krimm, H. A., Kulkarni, S. R., Kumar, P., Lebrun, F., Lloyd-Ronning, N. M., Markwardt, C. B., Mattson, B. J., Mushotzky, R. F., Norris, J. P., Osborne, J., Paczynski, B., Palmer, D. M., Park, H.-S., Parsons, A. M., Paul, J., Rees, M. J., Reynolds, C. S., Rhoads, J. E., Sasseen, T. P., Schaefer, B. E., Short, A. T., Smale, A. P., Smith, I. A., Stella, L., Tagliaferri, G., Takahashi, T., Tashiro, M., Townsley, L. K., Tueller, J., Turner, M. J. L., Vietri, M., Voges, W., Ward, M. J., Willingale, R., Zerbi, F. M., and Zhang, W. W. (2004). The Swift Gamma-Ray Burst Mission. ApJ., 611:1005–1020.

Gehrels, N., Norris, J. P., Barthelmy, S. D., Granot, J., Kaneko, Y., Kouveliotou, C., Markwardt, C. B., Mészáros, P., Nakar, E., Nousek, J. A., O'Brien, P. T., Page, M., Palmer, D. M., Parsons, A. M., Roming, P. W. A., Sakamoto, T., Sarazin, C. L., Schady, P., Stamatikos, M., and Woosley, S. E. (2006). A new γ-ray burst classification scheme from GRB060614. Nature, 444:1044–1046.

Gehrels, N., Ramirez-Ruiz, E., and Fox, D. B. (2009). Gamma-Ray Bursts in the Swift Era. ARA&A, 47:567–617.

Gehrels, N., Sarazin, C. L., O'Brien, P. T., Zhang, B., Barbier, L., Barthelmy, S. D., Blustin, A., Burrows, D. N., Cannizzo, J., Cummings, J. R., Goad, M., Holland, S. T., Hurkett, C. P., Kennea, J. A., Levan, A., Markwardt, C. B., Mason, K. O., Meszaros, P., Page, M., Palmer, D. M., Rol, E., Sakamoto, T., Willingale, R., Angelini, L., Beardmore, A., Boyd, P. T., Breeveld, A., Campana, S., Chester, M. M., Chincarini, G., Cominsky, L. R., Cusumano, G., de Pasquale, M., Fenimore, E. E., Giommi, P., Gronwall, C., Grupe, D., Hill, J. E., Hinshaw, D., Hjorth, J., Hullinger, D., Hurley, K. C., Klose, S., Kobayashi, S., Kouveliotou, C., Krimm, H. A., Mangano, V., Marshall, F. E., McGowan, K., Moretti, A., Mushotzky, R. F., Nakazawa, K., Norris, J. P., Nousek, J. A., Osborne, J. P., Page, K., Parsons, A. M., Patel, S., Perri, M., Poole, T., Romano, P., Roming, P. W. A., Rosen, S., Sato, G., Schady, P., Smale, A. P., Sollerman, J., Starling, R., Still, M., Suzuki, M., Tagliaferri, G., Takahashi, T., Tashiro, M., Tueller, J., Wells, A. A., White, N. E., and Wijers, R. A. M. J. (2005). A short γ-ray burst apparently associated with an elliptical galaxy at redshift z = 0.225. Nature, 437:851–854.

Ghirlanda, G., Ghisellini, G., and Lazzati, D. (2004). The Collimation-corrected Gamma-Ray Burst Energies Correlate with the Peak Energy of Their vFv Spectrum. ApJ., 616:331–338.

Giblin, T. W., Kouveliotou, C., and van Paradijs, J. (1998). Power spectra of BATSE GRB time profiles. In C. A. Meegan, R. D. Preece, & T. M. Koshut, editor, *Gamma-*

Ray Bursts, 4th Hunstville Symposium, volume 428 of *American Institute of Physics Conference Series*, pages 241–245.

Golenetskii, S., Aptekar, R., Frederiks, D., Mazets, E., Pal'Shin, V., Oleynik, P., Ulanov, M., Svinkin, D., and Cline, T. (2009). Konus-wind and Konus-RF observations of GRB 090715B. *GRB Coordinates Network*, 9679:1–+.

Golenetskii, S., Aptekar, R., Mazets, E., Pal'Shin, V., Frederiks, D., and Cline, T. (2005a). Konus-wind observation of GRB 050401. *GRB Coordinates Network*, 3179:1–+.

Golenetskii, S., Aptekar, R., Mazets, E., Pal'Shin, V., Frederiks, D., and Cline, T. (2005b). Konus-wind observation of GRB 050603. *GRB Coordinates Network*, 3518:1–+.

Golenetskii, S., Aptekar, R., Mazets, E., Pal'Shin, V., Frederiks, D., and Cline, T. (2006a). Konus-wind and konus-a observations of GRB 061121. *GRB Coordinates Network*, 5837:1–+.

Golenetskii, S., Aptekar, R., Mazets, E., Pal'Shin, V., Frederiks, D., and Cline, T. (2006b). Konus-wind observation of GRB 061007. *GRB Coordinates Network*, 5722:1–+.

Golenetskii, S., Aptekar, R., Mazets, E., Pal'Shin, V., Frederiks, D., and Cline, T. (2006c). Konus-wind observation of GRB 061021. *GRB Coordinates Network*, 5748:1–+.

Golenetskii, S., Aptekar, R., Mazets, E., Pal'Shin, V., Frederiks, D., and Cline, T. (2007a). Konus-wind observation of GRB 071010B. *GRB Coordinates Network*, 6879:1–+.

Golenetskii, S., Aptekar, R., Mazets, E., Pal'Shin, V., Frederiks, D., and Cline, T. (2007b). Konus-wind observation of GRB 071020. *GRB Coordinates Network*, 6960:1–+.

Golenetskii, S., Aptekar, R., Mazets, E., Pal'Shin, V., Frederiks, D., and Cline, T. (2008a). Konus-wind observation of GRB 080319B. *GRB Coordinates Network*, 7482:1–+.

Golenetskii, S., Aptekar, R., Mazets, E., Pal'Shin, V., Frederiks, D., and Cline, T. (2008b). Konus-wind observation of GRB 080319C. *GRB Coordinates Network*, 7487:1–+.

Golenetskii, S., Aptekar, R., Mazets, E., Pal'Shin, V., Frederiks, D., and Cline, T. (2008c). Konus-wind observation of GRB 080411. *GRB Coordinates Network*, 7589:1–+.

Golenetskii, S., Aptekar, R., Mazets, E., Pal'Shin, V., Frederiks, D., and Cline, T. (2008d). Konus-wind observation of GRB 080605. *GRB Coordinates Network*, 7854:1–+.

Golenetskii, S., Aptekar, R., Mazets, E., Pal'Shin, V., Frederiks, D., Oleynik, P., Ulanov, M., Svinkin, D., and Cline, T. (2008e). Konus-wind observation of GRB 080607. *GRB Coordinates Network*, 7862:1–+.

Golenetskii, S., Aptekar, R., Mazets, E., Pal'Shin, V., Frederiks, D., Oleynik, P., Ulanov, M., Svinkin, D., and Cline, T. (2008f). Konus-wind observation of GRB 080721. *GRB Coordinates Network*, 7995:1–+.

Golenetskii, S., Aptekar, R., Mazets, E., Pal'Shin, V., Frederiks, D., Ulanov, M., and Cline, T. (2006d). Konus-wond observation of GRB 060418. *GRB Coordinates Network*, 4989:1–+.

Granot, J., for the Fermi LAT Collaboration, and the GBM Collaboration (2010). Highlights from Fermi GRB observations. *ArXiv e-prints*.

Grupe, D., Breeveld, A., Landsman, W., Fenimore, E. E., Cummings, J., Chester, M. M., Palmer, D. M., Barthelmy, S. D., Burrows, D. N., Roming, P., and Gehrels, N. (2009). Swift observation of GRB 081222. *GCN Report*, 190:1–+.

Guidorzi, C. (2005). Testing the gamma-ray burst variability/peak luminosity correlation using the pseudo-redshifts of a large sample of BATSE gamma-ray bursts. MNRAS, 364:163–168.

Guidorzi, C., Frontera, F., Montanari, E., Rossi, F., Amati, L., Gomboc, A., Hurley, K., and Mundell, C. G. (2005). The gamma-ray burst variability-peak luminosity correlation: new results. MNRAS, 363:315–325.

Guidorzi, C., Frontera, F., Montanari, E., Rossi, F., Amati, L., Gomboc, A., and Mundell, C. G. (2006). The slope of the gamma-ray burst variability/peak luminosity correlation. MNRAS, 371:843–851.

Guidorzi, C., Stamatikos, M., Landsman, W., Barthelmy, S. D., Burrows, D. N., Roming, P., and Gehrels, N. (2008). Swift Observations of GRB 080430. *GCN Report*, 139:1–3.

Guiriec, S., Connaughton, V., Briggs, M. S., Burgess, M., Ryde, F., Daigne, F., Mészáros, P., Goldstein, A., McEnery, J., Omodei, N., Bhat, P. N., Bissaldi, E., Camero-Arranz, A., Chaplin, V., Diehl, R., Fishman, G., Foley, S., Gibby, M., Giles, M. M., Greiner, J., Gruber, D., von Kienlin, A., Kippen, M., Kouveliotou, C., McBreen, S., Meegan, C. A., Paciesas, W., Preece, R., Rau, A., Tierney, D., van der Horst, A. J., and Wilson-Hodge, C. (2010). Detection of a Thermal Spectral Component in the Prompt Emission of GRB 100724B. *ArXiv e-prints*.

Hakkila, J., Giblin, T. W., Norris, J. P., Fragile, P. C., and Bonnell, J. T. (2008). Correlations between Lag, Luminosity, and Duration in Gamma-Ray Burst Pulses. ApJ. Lett., 677:L81–L84.

Hakkila, J. and Nemiroff, R. J. (2009). Testing the Gamma-ray Burst Pulse Start Conjecture. ApJ., 705:372–385.

Holland, S. T., Sakamoto, T., Beardmore, A. P., Norris, J., Page, K. L., Barthelmy, S. D., Burrows, D. N., Roming, P., and Gehrels, N. (2007). Final Swift observations of GRB 071020. *GCN Report*, 94:2–+.

Hurst, H. E. (1951). Long-term storage capacity of reservoirs. Trans. Am. Sco. Civ. Eng., 116:770–808.

Ioka, K. and Nakamura, T. (2001). Peak Luminosity-Spectral Lag Relation Caused by the Viewing Angle of the Collimated Gamma-Ray Bursts. ApJ. Lett., 554:L163–L167.

Jakobsson, P., Vreeswijk, P. M., Hjorth, J., Malesani, D., Fynbo, J. P. U., and Thoene, C. C. (2007). GRB 071020: VLT spectroscopy. *GRB Coordinates Network*, 6952:1–+.

Jaunsen, A. O., Rol, E., Watson, D. J., Malesani, D., Fynbo, J. P. U., Milvang-Jensen, B., Hjorth, J., Vreeswijk, P. M., Ovaldsen, J., Wiersema, K., Tanvir, N. R., Gorosabel, J.,

Levan, A. J., Schirmer, M., and Castro-Tirado, A. J. (2008). GRB 070306: A Highly Extinguished Afterglow. ApJ., 681:453–461.

Jenkins, G. M. and Watts, D. G. (1969). *Spectral analysis and its applications.*

Kamenshchik, A., Moschella, U., and Pasquier, V. (2001). An alternative to quintessence. *Physics Letters B*, 511:265–268.

Kaneko, Y., Preece, R. D., Briggs, M. S., Paciesas, W. S., Meegan, C. A., and Band, D. L. (2006). The Complete Spectral Catalog of Bright BATSE Gamma-Ray Bursts. ApJ. Supp., 166:298–340.

Klebesadel, R. W., Strong, I. B., and Olson, R. A. (1973). Observations of Gamma-Ray Bursts of Cosmic Origin. ApJ. Lett., 182:L85+.

Kobayashi, S., Ryde, F., and MacFadyen, A. (2002). Luminosity and Variability of Collimated Gamma-Ray Bursts. ApJ., 577:302–310.

Kocevski, D. and Liang, E. (2003). The Connection between Spectral Evolution and Gamma-Ray Burst Lag. ApJ., 594:385–389.

Kouveliotou, C., Meegan, C. A., Fishman, G. J., Bhat, N. P., Briggs, M. S., Koshut, T. M., Paciesas, W. S., and Pendleton, G. N. (1993). Identification of two classes of gamma-ray bursts. ApJ. Lett., 413:L101–L104.

Krimm, H. A., Yamaoka, K., Sugita, S., Ohno, M., Sakamoto, T., Barthelmy, S. D., Gehrels, N., Hara, R., Norris, J. P., Ohmori, N., Onda, K., Sato, G., Tanaka, H., Tashiro, M., and Yamauchi, M. (2009a). Testing the $E_{peak} - E_{iso}$ Relation for GRBs Detected by Swift and Suzaku-WAM. ApJ., 704:1405–1432.

Krimm, H. A., Yamaoka, K., Sugita, S., Ohno, M., Sakamoto, T., Barthelmy, S. D., Gehrels, N., Hara, R., Norris, J. P., Ohmori, N., Onda, K., Sato, G., Tanaka, H., Tashiro, M., and Yamauchi, M. (2009b). Testing the Epeak - Eiso relation for GRBs detected by Swift and Suzaku-WAM. *ArXiv e-prints.*

Lamb, D. Q. and Reichart, D. E. (2000). Gamma-Ray Bursts as a Probe of the Very High Redshift Universe. ApJ., 536:1–18.

Lazzati, D. (2002). The role of photon scattering in shaping the light curves and spectra of γ-ray bursts. MNRAS, 337:1426–1434.

Lehnert, M. D., Nesvadba, N. P. H., Cuby, J., Swinbank, A. M., Morris, S., Clément, B., Evans, C. J., Bremer, M. N., and Basa, S. (2010). Spectroscopic confirmation of a galaxy at redshift z = 8.6. Nature, 467:940–942.

Li, L. and Paczyński, B. (2006). Improved correlation between the variability and peak luminosity of gamma-ray bursts. MNRAS, 366:219–226.

Li, T., Qu, J., Feng, H., Song, L., Ding, G., and Chen, L. (2004). Timescale Analysis of Spectral Lags. *Chinese Journal of Astronomy and Astrophysics*, 4:583–598.

Liang, E. and Zhang, B. (2005). Model-independent Multivariable Gamma-Ray Burst Luminosity Indicator and Its Possible Cosmological Implications. ApJ., 633:611–623.

Lu, R., Qin, Y., Zhang, Z., and Yi, T. (2006). Spectral lags caused by the curvature effect of fireballs. MNRAS, 367:275–289.

MacFadyen, A. I. and Woosley, S. E. (1999). Collapsars: Gamma-Ray Bursts and Explosions in "Failed Supernovae". ApJ., 524:262–289.

Madau, P., Della Valle, M., and Panagia, N. (1998). On the evolution of the cosmic supernova rates. *MNRAS*, 297:L17–122.

Mandelbrot, B. B. and Wallis, J. R. (1969). Robustness of the Rescaled Range R/S in the Measurement of Noncyclic Long Run Statistical Dependence. *Water Resources Research*, 5:967–988.

Mangano, V., Cummings, J., Barthelmy, S. D., Sbarufatti, B., Schady, P., Burrows, D. N., Roming, P., and Gehrels, N. (2008a). Swift Observations of GRB 080607. *GCN Report*, 147:1–4.

Mangano, V., Parsons, A., Sakamoto, T., La Parola, V., Kuin, N. P. M., Barthelmy, S. D., Burrows, D. N., Roming, P., and Gehrels, N. (2008b). Swift Observation of GRB 080603B. *GCN Report*, 144:1–4.

Mannheim, P. D. (2006). Alternatives to dark matter and dark energy. *Progress in Particle and Nuclear Physics*, 56:340–445.

Margutti, R., Guidorzi, C., Chincarini, G., Bernardini, M. G., Genet, F., Mao, J., and Pasotti, F. (2010). Lag-luminosity relation in γ-ray burst X-ray flares: a direct link to the prompt emission. MNRAS, 406:2149–2167.

Markwardt, C., Kennea, J., Mangano, V., Barthelmy, S. D., Burrows, D. N., Roming, P., and Gehrels, N. (2007). Swift observations of GRB 071010B. *GCN Report*, 92:1–+.

Markwardt, C. B. (2009). Non-linear Least-squares Fitting in IDL with MPFIT. In D. A. Bohlender, D. Durand, & P. Dowler, editor, *Astronomical Society of the Pacific Conference Series*, volume 411 of *Astronomical Society of the Pacific Conference Series*, pages 251–+.

Marshall, F. E., Barthelmy, S. D., Burrows, D. N., Evans, P. A., Oates, S. R., Stamatikos, M., and Gehrels, N. (2008a). Final Swift Observations of GRB 080413A. *GCN Report*, 129:1–+.

Marshall, F. E., Guidorzi, C., Ward, P. A., Barthelmy, S. D., Burrows, D. N., Roming, P., and Gehrels, N. (2008b). Swift Observations of GRB 080721. *GCN Report*, 156:1–4.

McBreen, S. (2009). GRB 090618: Fermi GBM observation. *GRB Coordinates Network*, 9535:1–+.

Melia, F. (2009). *High-Energy Astrophysics*. Princeton University Press, Princeton, NJ 08540.

Meszaros, P., Laguna, P., and Rees, M. J. (1993). Gasdynamics of relativistically expanding gamma-ray burst sources - Kinematics, energetics, magnetic fields, and efficiency. ApJ., 415:181–190.

Meszaros, P. and Rees, M. J. (1993). Relativistic fireballs and their impact on external matter - Models for cosmological gamma-ray bursts. ApJ., 405:278–284.

Meszaros, P. and Rees, M. J. (1997). Poynting Jets from Black Holes and Cosmological Gamma-Ray Bursts. ApJ. Lett., 482:L29+.

Morsony, B. J., Lazzati, D., and Begelman, M. C. (2010). The origin and propagation of variability in the outflows of long duration gamma-ray bursts. *ArXiv e-prints*.

Na, X. S., Wang, N., Yuan, J. P., Liu, Z. Y., Pan, J., and Xu, R. X. (2009). Hurst parameter analysis of radio pulsar timing noise. *ArXiv e-prints*.

Narayan, R., Paczynski, B., and Piran, T. (1992). Gamma-ray bursts as the death throes of massive binary stars. ApJ. Lett., 395:L83–L86.

Nemiroff, R. J. (2000). The Pulse Scale Conjecture and the Case of BATSE Trigger 2193. ApJ., 544:805–810.

Norris, J. P. (2002). Implications of the Lag-Luminosity Relationship for Unified Gamma-Ray Burst Paradigms. ApJ., 579:386–403.

Norris, J. P., Bonnell, J. T., Kazanas, D., Scargle, J. D., Hakkila, J., and Giblin, T. W. (2005). Long-Lag, Wide-Pulse Gamma-Ray Bursts. ApJ., 627:324–345.

Norris, J. P., Marani, G. F., and Bonnell, J. T. (2000). Connection between Energy-dependent Lags and Peak Luminosity in Gamma-Ray Bursts. ApJ., 534:248–257.

Norris, J. P., Nemiroff, R. J., Bonnell, J. T., Scargle, J. D., Kouveliotou, C., Paciesas, W. S., Meegan, C. A., and Fishman, G. J. (1996). Attributes of Pulses in Long Bright Gamma-Ray Bursts. ApJ., 459:393–+.

Palmer, D., Barbier, L., Barthelmy, S., Chester, M., Cummings, J., Fenimore, E., Gehrels, N., Hullinger, D., Krimm, H., Markwardt, C., Marshall, F., Mitani, T., Parsons, A., Sakamoto, T., Sato, G., Suzuki, M., and Tueller, J. (2006). GRB 060206: Swift-BAT refined analysis. *GRB Coordinates Network*, 4697:1–+.

Penprase, B. E., Berger, E., Fox, D. B., Kulkarni, S. R., Kadish, S., Kerber, L., Ofek, E., Kasliwal, M., Hill, G., Schaefer, B., and Reed, M. (2006). Spectroscopy of GRB 051111 at z = 1.54948: Kinematics and Elemental Abundances of the GRB Environment and Host Galaxy. ApJ., 646:358–368.

Perlmutter, S., Aldering, G., Goldhaber, G., Knop, R. A., Nugent, P., Castro, P. G., Deustua, S., Fabbro, S., Goobar, A., Groom, D. E., Hook, I. M., Kim, A. G., Kim, M. Y., Lee, J. C., Nunes, N. J., Pain, R., Pennypacker, C. R., Quimby, R., Lidman, C., Ellis, R. S., Irwin, M., McMahon, R. G., Ruiz-Lapuente, P., Walton, N., Schaefer, B., Boyle, B. J., Filippenko, A. V., Matheson, T., Fruchter, A. S., Panagia, N., Newberg, H. J. M., Couch, W. J., and The Supernova Cosmology Project (1999). Measurements of Omega and Lambda from 42 High-Redshift Supernovae. ApJ., 517:565–586.

Piran, T. (1999). Gamma-ray bursts and the fireball model. Physics Reports, 314:575–667.

Piran, T. (2005). The beaming factor and other open issues in GRB Jets. *Nuovo Cimento C Geophysics Space Physics C*, 28:373–+.

Piranomonte, S., Ward, P. A., Fiore, F., Vergani, S. D., D'Elia, V., Krongold, Y., Nicastro, F., Meurs, E. J. A., Chincarini, G., Covino, S., Della Valle, M., Fugazza, D., Norci, L., Sbordone, L., Stella, L., Tagliaferri, G., Burrows, D. N., Gehrels, N., Goldoni, P., Malesani, D., Mirabel, I. F., Pellizza, L. J., and Perna, R. (2008). Probing the complex environments of GRB host galaxies and intervening systems: high resolution spectroscopy of GRB050922C. A.& A., 492:775–785.

Preece, R. D., Briggs, M. S., Mallozzi, R. S., Pendleton, G. N., Paciesas, W. S., and Band, D. L. (2000). The BATSE Gamma-Ray Burst Spectral Catalog. I. High Time Resolution Spectroscopy of Bright Bursts Using High Energy Resolution Data. ApJ. Supp., 126:19–36.

Press, W. H. (2002). *Numerical recipes in C++ : the art of scientific computing*.

Prochaska, J. X., Chen, H., Bloom, J. S., Falco, E., and Dupree, A. K. (2006). GRB060418: further analysis of MIKE spectroscopy. *GRB Coordinates Network*, 5002:1–+.

Prochaska, J. X., Sheffer, Y., Perley, D. A., Bloom, J. S., Lopez, L. A., Dessauges-Zavadsky, M., Chen, H., Filippenko, A. V., Ganeshalingam, M., Li, W., Miller, A. A., and Starr, D. (2009). The First Positive Detection of Molecular Gas in a GRB Host Galaxy. ApJ. Lett., 691:L27–L32.

Quilligan, F., McBreen, B., Hanlon, L., McBreen, S., Hurley, K. J., and Watson, D. (2002). Temporal properties of gamma ray bursts as signatures of jets from the central engine. A.& A., 385:377–398.

Racusin, J. L., Holland, S. T., Cummings, J., Oates, S. R., and Schady, P. (2008). Swift Observation of GRB 080319B. *GCN Report*, 134:1–3.

Ramirez-Ruiz, E. and Fenimore, E. E. (2000). Pulse Width Evolution in Gamma-Ray Bursts: Evidence for Internal Shocks. ApJ., 539:712–717.

Rees, M. J. and Meszaros, P. (1992). Relativistic fireballs - Energy conversion and time-scales. MNRAS, 258:41P–43P.

Rees, M. J. and Meszaros, P. (1994). Unsteady outflow models for cosmological gamma-ray bursts. ApJ. Lett., 430:L93–L96.

Reichart, D. E., Lamb, D. Q., Fenimore, E. E., Ramirez-Ruiz, E., Cline, T. L., and Hurley, K. (2001). A Possible Cepheid-like Luminosity Estimator for the Long Gamma-Ray Bursts. ApJ., 552:57–71.

Riess, A. G., Filippenko, A. V., Challis, P., Clocchiatti, A., Diercks, A., Garnavich, P. M., Gilliland, R. L., Hogan, C. J., Jha, S., Kirshner, R. P., Leibundgut, B., Phillips, M. M., Reiss, D., Schmidt, B. P., Schommer, R. A., Smith, R. C., Spyromilio, J., Stubbs, C., Suntzeff, N. B., and Tonry, J. (1998). Observational Evidence from Supernovae for an Accelerating Universe and a Cosmological Constant. AJ., 116:1009–1038.

Riess, A. G., Strolger, L., Tonry, J., Casertano, S., Ferguson, H. C., Mobasher, B., Challis, P., Filippenko, A. V., Jha, S., Li, W., Chornock, R., Kirshner, R. P., Leibundgut, B., Dickinson, M., Livio, M., Giavalisco, M., Steidel, C. C., Benítez, T., and Tsvetanov, Z. (2004). Type Ia Supernova Discoveries at z ¿ 1 from the Hubble Space Telescope: Evidence for Past Deceleration and Constraints on Dark Energy Evolution. ApJ., 607:665–687.

Rizzuto, D., Guidorzi, C., Romano, P., Covino, S., Campana, S., Capalbi, M., Chincarini, G., Cusumano, G., Fugazza, D., Mangano, V., Moretti, A., Perri, M., and Tagliaferri, G. (2007). Testing the gamma-ray burst variability/peak luminosity correlation on a Swift homogeneous sample. MNRAS, 379:619–628.

Roming, P. W. A., Kennedy, T. E., Mason, K. O., Nousek, J. A., Ahr, L., Bingham, R. E., Broos, P. S., Carter, M. J., Hancock, B. K., Huckle, H. E., Hunsberger, S. D., Kawakami, H., Killough, R., Koch, T. S., McLelland, M. K., Smith, K., Smith, P. J., Soto, J. C., Boyd, P. T., Breeveld, A. A., Holland, S. T., Ivanushkina, M., Pryzby, M. S., Still, M. D., and Stock, J. (2005). The Swift Ultra-Violet/Optical Telescope. *Space Science Reviews*, 120:95–142.

Roming, P. W. A., Koch, T. S., Oates, S. R., Porterfield, B. L., Vanden Berk, D. E., Boyd, P. T., Holland, S. T., Hoversten, E. A., Immler, S., Marshall, F. E., Page, M. J., Racusin, J. L., Schneider, D. P., Breeveld, A. A., Brown, P. J., Chester, M. M., Cucchiara, A., DePasquale, M., Gronwall, C., Hunsberger, S. D., Kuin, N. P. M., Landsman, W. B., Schady, P., and Still, M. (2009). The First Swift Ultraviolet/Optical Telescope GRB Afterglow Catalog. ApJ., 690:163–188.

Ryde, F. (2005). Interpretations of gamma-ray burst spectroscopy. I. Analytical and numerical study of spectral lags. A.& A., 429:869–879.

Sakamoto, T., Barthelmy, S. D., Barbier, L., Cummings, J. R., Fenimore, E. E., Gehrels, N., Hullinger, D., Krimm, H. A., Markwardt, C. B., Palmer, D. M., Parsons, A. M., Sato, G., Stamatikos, M., Tueller, J., Ukwatta, T. N., and Zhang, B. (2008a). The First Swift BAT Gamma-Ray Burst Catalog. ApJ. Supp., 175:179–190.

Sakamoto, T., Hullinger, D., Sato, G., Yamazaki, R., Barbier, L., Barthelmy, S. D., Cummings, J. R., Fenimore, E. E., Gehrels, N., Krimm, H. A., Lamb, D. Q., Markwardt, C. B., Osborne, J. P., Palmer, D. M., Parsons, A. M., Stamatikos, M., and Tueller, J. (2008b). Global Properties of X-Ray Flashes and X-Ray-Rich Gamma-Ray Bursts Observed by Swift. ApJ., 679:570–586.

Sakamoto, T., Lamb, D. Q., Kawai, N., Yoshida, A., Fenimore, C., Graziani E. E., Donaghy, T. Q., Matsuoka, M., Ricker, M., Suzuki G., Atteia, J., Shirasaki, Y., Torii, T., Tamagawa K., Nakagawa, Y., Galassi, M., Doty, J., Crew, R., Vanderspek G. B., Villasenor, J., Butler, N., Barraud, J. G., Jernigan C., Bore, M., Dezalay, J., Olive, J., Woosley, K., Hurley S. E., Pizzichini, G., and Hete-2 Science Team (2005). Global characteristics of X-ray flashes and X-ray rich GRBs observed by HETE-2. *Nuovo Cimento C Geophysics Space Physics C*, 28:339–+.

Sakamoto, T., Sato, G., Barbier, L., Barthelmy, S. D., Cummings, J. R., Fenimore, E. E., Gehrels, N., Hullinger, D., Krimm, H. A., Lamb, D. Q., Markwardt, C. B., Palmer, D. M., Parsons, A. M., Stamatikos, M., Tueller, J., and Ukwatta, T. N. (2009). E_{peak} Estimator for Gamma-Ray Bursts Observed by the Swift Burst Alert Telescope. ApJ., 693:922–935.

Salmonson, J. D. (2000). On the Kinematic Origin of the Luminosity-Pulse Lag Relationship in Gamma-Ray Bursts. ApJ. Lett., 544:L115–L117.

Salvaterra, R., Della Valle, M., Campana, S., Chincarini, G., Covino, S., D'Avanzo, P., Fernández-Soto, A., Guidorzi, C., Mannucci, F., Margutti, R., Thöne, C. C., Antonelli,

L. A., Barthelmy, S. D., de Pasquale, M., D'Elia, V., Fiore, F., Fugazza, D., Hunt, L. K., Maiorano, E., Marinoni, S., Marshall, F. E., Molinari, E., Nousek, J., Pian, E., Racusin, J. L., Stella, L., Amati, L., Andreuzzi, G., Cusumano, G., Fenimore, E. E., Ferrero, P., Giommi, P., Guetta, D., Holland, S. T., Hurley, K., Israel, G. L., Mao, J., Markwardt, C. B., Masetti, N., Pagani, C., Palazzi, E., Palmer, D. M., Piranomonte, S., Tagliaferri, G., and Testa, V. (2009). GRB090423 at a redshift of z~8.1. Nature, 461:1258–1260.

Sari, R., Piran, T., and Narayan, R. (1998). Spectra and Light Curves of Gamma-Ray Burst Afterglows. ApJ. Lett., 497:L17+.

Sato, G., Barthelmy, S. D., Baumgartner, W., Cummings, J., Fenimore, E., Gehrels, N., Krimm, H., Markwardt, C., Marshall, F. E., McLean, K., Palmer, D., Sakamoto, T., Stamatikos, M., Tueller, J., and Ukwatta, T. (2008). GRB 080411, Swift-BAT refined analysis. *GRB Coordinates Network*, 7591:1–+.

Sato, G., Yamazaki, R., Ioka, K., Sakamoto, T., Takahashi, T., Nakazawa, K., Nakamura, T., Toma, K., Hullinger, D., Tashiro, M., Parsons, A. M., Krimm, H. A., Barthelmy, S. D., Gehrels, N., Burrows, D. N., O'Brien, P. T., Osborne, J. P., Chincarini, G., and Lamb, D. Q. (2007). Swift Discovery of Gamma-Ray Bursts without a Jet Break Feature in Their X-Ray Afterglows. ApJ., 657:359–366.

Sbarufatti, B., Parsons, A., Sakamoto, T., Mangano, V., La Parola, V., Kuin, P., Barthelmy, S. D., Burrows, D. N., Roming, P., and Gehrels, N. (2008). Swift Observation of GRB 080605. *GCN Report*, 142:1–4.

Schady, P., Baumgartner, W. H., and Beardmore, A. P. (2009). Swift observation of GRB 090618. *GCN Report*, 232:1–+.

Schaefer, B. E. (2004). Explaining the Gamma-Ray Burst Lag/Luminosity Relation. ApJ., 602:306–311.

Schaefer, B. E. (2007). The Hubble Diagram to Redshift >6 from 69 Gamma-Ray Bursts. ApJ., 660:16–46.

Schaefer, B. E. and Walker, K. C. (1999). A Gamma-Ray Burst with a 220 Microsecond Rise Time and a Sharp Spectral Cutoff. ApJ. Lett., 511:L89–L92.

Shen, R., Song, L., and Li, Z. (2005). Spectral lags and the energy dependence of pulse width in gamma-ray bursts: contributions from the relativistic curvature effect. MNRAS, 362:59–65.

Stamatikos, M., Barthelmy, S. D., Cummings, J., Fenimore, E., Gehrels, N., Krimm, H., Markwardt, C., McLean, K., Pagani, C., Palmer, D., Parsons, A., Sakamoto, T., Sato, G., Tueller, J., and Ukwatta, T. (2008). GRB 080319C, Swift-BAT refined analysis. *GRB Coordinates Network*, 7483:1–+.

Stamatikos, M., t. (2008). *GCN Circ.*, (7272). http://gcn.gsfc.nasa.gov/gcn3/7272.gcn3.

Tamburini, F., de Martino, D., and Bianchini, A. (2009). Analysis of the white-light flickering of the intermediate polar V709 Cassiopeiae with wavelets and Hurst analysis. A.& A., 502:1–5.

Tanvir, N. R., Fox, D. B., Levan, A. J., Berger, E., Wiersema, K., Fynbo, J. P. U., Cucchiara, A., Krühler, T., Gehrels, N., Bloom, J. S., Greiner, J., Evans, P. A., Rol, E., Olivares, F., Hjorth, J., Jakobsson, P., Farihi, J., Willingale, R., Starling, R. L. C., Cenko, S. B., Perley, D., Maund, J. R., Duke, J., Wijers, R. A. M. J., Adamson, A. J., Allan, A., Bremer, M. N., Burrows, D. N., Castro-Tirado, A. J., Cavanagh, B., de Ugarte Postigo, A., Dopita, M. A., Fatkhullin, T. A., Fruchter, A. S., Foley, R. J., Gorosabel, J., Kennea, J., Kerr, T., Klose, S., Krimm, H. A., Komarova, V. N., Kulkarni, S. R., Moskvitin, A. S., Mundell, C. G., Naylor, T., Page, K., Penprase, B. E., Perri, M., Podsiadlowski, P., Roth, K., Rutledge, R. E., Sakamoto, T., Schady, P., Schmidt, B. P., Soderberg, A. M., Sollerman, J., Stephens, A. W., Stratta, G., Ukwatta, T. N., Watson, D., Westra, E., Wold, T., and Wolf, C. (2009). A γ-ray burst at a redshift of z~8.2. Nature, 461:1254–1257.

Ukwatta, T. N., Dhuga, K. S., Parke, W. C., Sakamoto, T., Markwardt, C. B., Barthelmy, S. D., Cioffi, D. F., Eskandarian, A., Gehrels, N., Maximon, L., and Morris, D. C. (2009a). Variability in the Prompt Emission of Swift-BAT Gamma-Ray Bursts. *ArXiv e-prints*.

Ukwatta, T. N., MacGibbon, J. H., Parke, W. C., Dhuga, K. S., Eskandarian, A., Gehrels, N., Maximon, L., and Morris, D. C. (2009b). Spectral Lags of Gamma-Ray Bursts from Primordial Black Hole (PBH) Evaporations. In C. Meegan, C. Kouveliotou, & N. Gehrels, editor, *American Institute of Physics Conference Series*, volume 1133 of *American Institute of Physics Conference Series*, pages 440–442.

Ukwatta, T. N., Stamatikos, M., Dhuga, K. S., Sakamoto, T., Barthelmy, S. D., Eskandarian, A., Gehrels, N., Maximon, L. C., Norris, J. P., and Parke, W. C. (2010). Spectral Lags and the Lag-Luminosity Relation: An Investigation with Swift BAT Gamma-ray Bursts. ApJ., 711:1073–1086.

van Paradijs, J., Groot, P. J., Galama, T., Kouveliotou, C., Strom, R. G., Telting, J., Rutten, R. G. M., Fishman, G. J., Meegan, C. A., Pettini, M., Tanvir, N., Bloom, J., Pedersen, H., Nørdgaard-Nielsen, H. U., Linden-Vørnle, M., Melnick, J., van der Steene, G., Bremer, M., Naber, R., Heise, J., in't Zand, J., Costa, E., Feroci, M., Piro, L., Frontera, F., Zavattini, G., Nicastro, L., Palazzi, E., Bennet, K., Hanlon, L., and Parmar, A. (1997). Transient optical emission from the error box of the γ-ray burst of 28 February 1997. Nature, 386:686–689.

Vedrenne, G. and Atteia, J. (2010). *Gamma-Ray Bursts*.

Vetere, L., Cummings, J. R., Breeveld, A., Barthelmy, S. D., Burrows, D. N., Roming, P. W. A., and Gehrels, N. (2009). Swift observations of GRB 090715B. *GCN Report*, 236:1–+.

Wainwright, C., Berger, E., and Penprase, B. E. (2007). A Morphological Study of Gamma-Ray Burst Host Galaxies. ApJ., 657:367–377.

Walker, K. C., Schaefer, B. E., and Fenimore, E. E. (2000). Gamma-Ray Bursts Have Millisecond Variability. ApJ., 537:264–269.

Watson, D., Fynbo, J. P. U., Ledoux, C., Vreeswijk, P., Hjorth, J., Smette, A., Andersen, A. C., Aoki, K., Augusteijn, T., Beardmore, A. P., Bersier, D., Castro Cerón, J. M., D'Avanzo, P., Diaz-Fraile, D., Gorosabel, J., Hirst, P., Jakobsson, P., Jensen, B. L.,

Kawai, N., Kosugi, G., Laursen, P., Levan, A., Masegosa, J., Näränen, J., Page, K. L., Pedersen, K., Pozanenko, A., Reeves, J. N., Rumyantsev, V., Shahbaz, T., Sharapov, D., Sollerman, J., Starling, R. L. C., Tanvir, N., Torstensson, K., and Wiersema, K. (2006). A logN$_{HI}$ = 22.6 Damped Lyα Absorber in a Dark Gamma-Ray Burst: The Environment of GRB 050401. ApJ., 652:1011–1019.

Wiersema, K., Levan, A., Kamble, A., Tanvir, N., and Malesani, D. (2009). GRB090715B: WHT redshift. *GRB Coordinates Network*, 9673:1–+.

Willingale, R., O'Brien, P. T., Osborne, J. P., Godet, O., Page, K. L., Goad, M. R., Burrows, D. N., Zhang, B., Rol, E., Gehrels, N., and Chincarini, G. (2007). Testing the Standard Fireball Model of Gamma-Ray Bursts Using Late X-Ray Afterglows Measured by Swift. ApJ., 662:1093–1110.

Woosley, S. E. (1993). Gamma-ray bursts from stellar mass accretion disks around black holes. ApJ., 405:273–277.

Woosley, S. E. and Bloom, J. S. (2006). The supernova gamma-ray burst connection. *ARAA*, 44:507W.

Woosley, S. E. and Bloom, J. S. (2006). The Supernova Gamma-Ray Burst Connection. ARA&A, 44:507–556.

Woosley, S. E. and Heger, A. (2006). The Progenitor Stars of Gamma-Ray Bursts. ApJ., 637:914–921.

Wu, B. and Fenimore, E. (2000). Spectral Lags of Gamma-Ray Bursts From Ginga and BATSE. ApJ. Lett., 535:L29–L32.

Yonetoku, D., Murakami, T., Nakamura, T., Yamazaki, R., Inoue, A. K., and Ioka, K. (2004). Gamma-Ray Burst Formation Rate Inferred from the Spectral Peak Energy-Peak Luminosity Relation. ApJ., 609:935–951.

Zhang, B., Zhang, B.-B., Virgili, F. J., Liang, E.-W., Kann, D. A., Wu, X.-F., Proga, D., Lv, H.-J., Toma, K., Meszaros, P., Burrows, D. N., Roming, P. W. A., and Gehrels, N. (2009). Discerning the physical origins of cosmological Gamma-ray bursts based on multiple observational criteria: the cases of z=6.7 GRB 080913, z=8.3 GRB 090423, and some short/hard GRBs. *ArXiv e-prints*.

Ziaeepour, H., Oates, S., Sakamoto, T., Baumgartner, W., Starling, R. L. C., and Holland, S. T. (2008). Further Revised Swift Observation of GRB 080916A. *GCN Report*, 167:3–+.

Appendix A

GRB Luminosity Relations

A.0.1 Amati Relation

The Amati relation is the relationship between the peak energy of the $\nu F \nu$ spectrum in the rest frame, $E_{\rm p}^{\rm src}$ and the isotropic equivalent energy, $E_{\rm iso}$ (Amati et al., 2002).

$$E_{\rm p}^{\rm src} \propto E_{\rm iso}^{0.52 \pm 0.06} \tag{A.1}$$

A.0.2 Ghirlanda Relation

The Ghirlanda relation connects the collimation-corrected prompt isotropic equivalent energy, E_γ, with the time-averaged $E_{\rm p}^{\rm src}$ at the GRB rest-frame (Ghirlanda et al., 2004).

$$E_{\rm p}^{\rm src} = 267.0 \left(\frac{E_\gamma}{4.3 \times 10^{50} {\rm ergs}} \right)^{0.706 \pm 0.047} {\rm keV} \tag{A.2}$$

A.0.3 Yonetoku Relation

The Yonetoku relation is the relationship between the isotropic peak luminosity and the time-averaged $E_{\rm p}^{\rm src}$ energy at the GRB rest-frame (Yonetoku et al., 2004).

$$\frac{L}{10^{52} \, {\rm ergs \, s^{-1}}} = (2.34^{+2.29}_{-1.76}) \times 10^{-5} \left[\frac{E_{\rm p}^{\rm src}}{1 \, {\rm keV}} \right]^{2.0 \mp 0.2} \tag{A.3}$$

A.0.4 Liang-Zhang Relation

The Liang-Zhang Relation is a multi-variable relation which consists of isotropic gamma-ray energy, $E_{\rm iso}$, the peak energy in the rest-frame, $E_{\rm p}^{\rm src}$, and the rest-frame break time of the optical afterglow light curves, $t_b^{\rm src}$ (Liang and Zhang, 2005).

$$\frac{E_{\rm iso}}{10^{52} {\rm ergs}} = (0.85 \pm 0.21) \left(\frac{E_{\rm p}^{\rm src}}{100 \, {\rm keV}} \right)^{1.94 \pm 0.17} \left(\frac{t_{\rm b}^{\rm src}}{1 \, {\rm day}} \right)^{-1.24 \pm 0.23} \tag{A.4}$$

A.0.5 Firmani Relation

Firmani et al. (2006) proposed a relation between three prompt emission properties of GRBs: The isotropic peak luminosity, $E_{\rm p}^{\rm src}$ and $T_{0.45}^{\rm src}$ which is the source-frame cumulative

time period where the GRB count rate is about 45% of its maximum rate.

$$L_{\text{iso}} \propto (E_{\text{p}}^{\text{src}})^{1.62}(T_{0.45}^{\text{src}})^{-0.49} \tag{A.5}$$

A.0.6 Lag-Luminosity Relation

Lag-Luminosity Relation is the relationship between peak luminosity (L) and spectral lag (τ) (Norris et al., 2000).

$$\frac{L}{10^{53}\,\text{ergs}} \sim 1.3 \times \left(\frac{\tau}{0.01\,\text{s}}\right)^{-1.15} \tag{A.6}$$

A.0.7 Variability-Luminosity Relation

Variability-Luminosity Relation is the relationship between peak luminosity (L) and time variability (V) (Fenimore and Ramirez-Ruiz, 2000).

$$\frac{L}{\text{d}\Omega} = 3.1 \times 10^{56}\,V^{3.35}\,\text{erg s}^{-1} \tag{A.7}$$

More recent studies of this variability-luminosity relation yields the following relation (Guidorzi et al., 2005, 2006; Rizzuto et al., 2007).

$$L_{\text{iso}} \propto V^{1.7\pm0.4} \tag{A.8}$$

Appendix B

Isotropic Peak Luminosity

To compare observations with different instruments we need to calculate flux over some fixed energy band. In order to do this we need to know the best–fit spectral function to the observed spectrum and its spectral parameters. Often, GRB spectra can be well fitted with the Band function (Band et al., 1993), an empirical spectral model defined as follows:

$$
N = \begin{cases} A(\frac{E}{100\,\text{kev}})^{\alpha}\, e^{-(2+\alpha)E/E_\text{p}}, & E \leq \left(\frac{\alpha-\beta}{2+\alpha}\right)E_\text{p} \\ A(\frac{E}{100\,\text{kev}})^{\beta}\, \left[\frac{(\alpha-\beta)E_\text{p}}{(2+\alpha)100\,\text{keV}}\right]^{\alpha-\beta} e^{(\beta-\alpha)}, & \text{otherwise.} \end{cases}
$$

There are four model parameters in the Band function; the amplitude (A), the low-energy spectral index (α), the high-energy spectral index (β) and the peak of νF_ν spectrum (E_p).

If the GRB spectrum is well described by the Band function, then the values of α, β, E_p and the observed peak flux, f_obs, in a given energy band (E_min and E_max) are often reported. We can calculate the normalization A with

$$
A = \frac{f_\text{obs}}{\int_{E_\text{min}}^{E_\text{max}} N'(E)\, dE} \tag{B.1}
$$

where f_obs is given in photons $\text{cm}^{-2}\,\text{s}^{-1}$ and $N' = N/A$.

The observed peak flux for the source-frame energy range $E_1 = 1.0\,\text{keV}$ to $E_2 = 10{,}000\,\text{keV}$ is

$$
f_\text{obs}^\text{new} = \int_{E_1/(1+z)}^{E_2/(1+z)} N(E)E\, dE. \tag{B.2}
$$

The isotropic peak luminosity is

$$
L_\text{iso} = 4\pi d_L^2\, f_\text{obs}^\text{new} \tag{B.3}
$$

where d_L is the luminosity distance given by,

$$
d_L = \frac{(1+z)c}{H_0} \int_0^z \frac{dz'}{\sqrt{\Omega_M(1+z')^3 + \Omega_L}} \tag{B.4}
$$

For the current universe we have assumed, $\Omega_M = 0.27$, $\Omega_L = 0.73$ and the Hubble constant H_0 is $70\,(\text{kms}^{-1})/\text{Mpc} = 2.268 \times 10^{-18}\,\text{s}^{-1}$.

To determine the uncertainty in L_iso, we employ a Monte Carlo simulation. We simulate spectral parameters α, β, E_p and flux assuming their reported value as sample mean and reported uncertainty as sample standard deviation, then calculate L_iso, for 1,000 variations

in these parameters. If a parameter has uneven uncertainty values then each side around the parameter is simulated with different uncertainty values as standard deviation. Then we take the 16th and the 84th ranked values (1σ uncertainty) as the lower limit and the upper limit of L_{iso} respectively.

Appendix C

CCF Dependance of the Waveform

How does the CCF depends on the waveform or the profile of the light curve?

In order to investigate the effect of the profile of the light curve on the CCF we generated various light curves with different profiles. Figures C.1 through C.11 show the effect of the light curve profile on the two CCF definitions. In each figure there are two sets of four panels. The left set of four panels shows the CCF analysis for two noise-free synthetic light curves with 10 second artificially introduced lag. In the right set of four panels we added 10% noise to the light curve to see how that effects the CCF for various light curves. The top right panel of the two sets shows the CCF vs time delay plot for CCF_{Band} definition (equation 5.2) and the lower right plot shows the same plot for CCF_{Std} definition (equation 5.1). In these plots the "Lag1" corresponds to the lag value obtained by the maximum of the CCF without fitting a curve and "Lag2(Fit)" corresponds to the lag obtained from a Gaussian fit.

Based on this analysis we can make the following conclusions.

- CCF_{Band} definition managed to recover the introduced lag for all the tested waveforms while CCF_{Std} definition fails for some waveforms (see Fig C.5, C.7 and C.9 for some extreme cases).

- A reasonable way to recover the lag is to fit a Gaussian curve to the CCF. Especially for light curves with some noise, picking the time delay corresponding to the maximum of the CCF value will result in incorrect lag.

- For most of the waveforms that we tested, the CCF profile can be adequately fit by a Gaussian curve provided a suitable fitting range is selected.
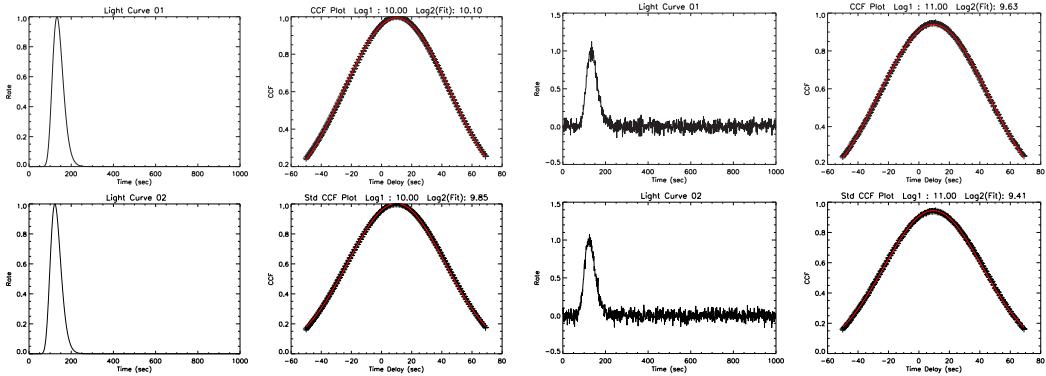
Figure C.1 Single peak FRED like light curve.
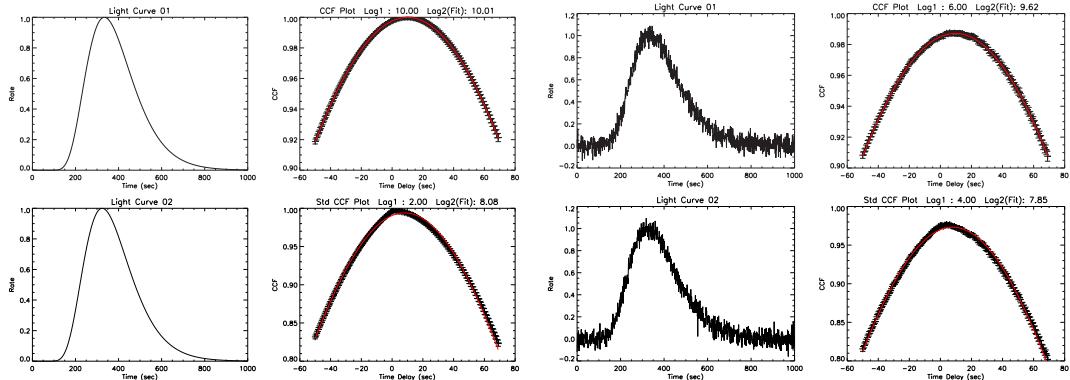
Figure C.2 Single peak FRED like light curve with a broad tail.
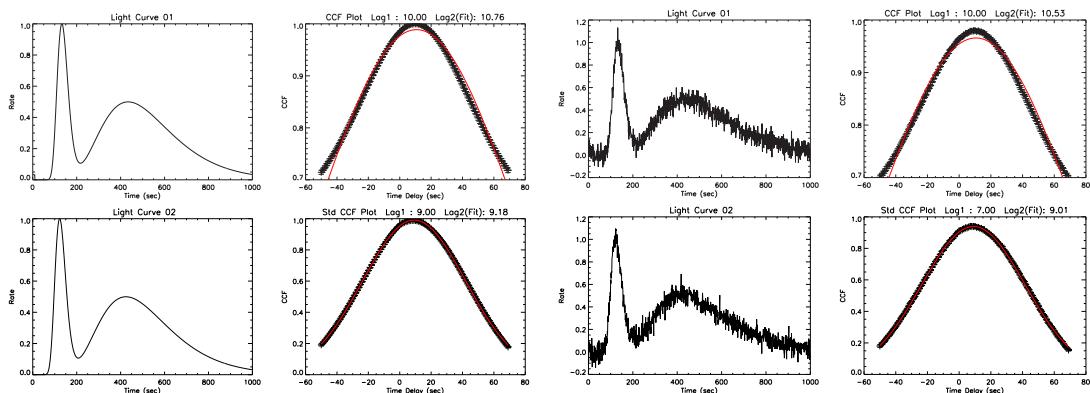
Figure C.3 Two FRED like peaks with one narrow and the other one with a broad tail.
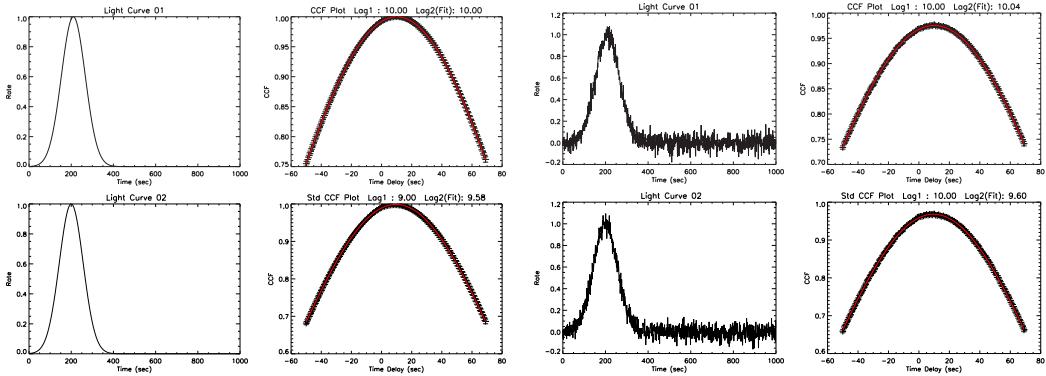
Figure C.4 Narrow Gauss like light curve.
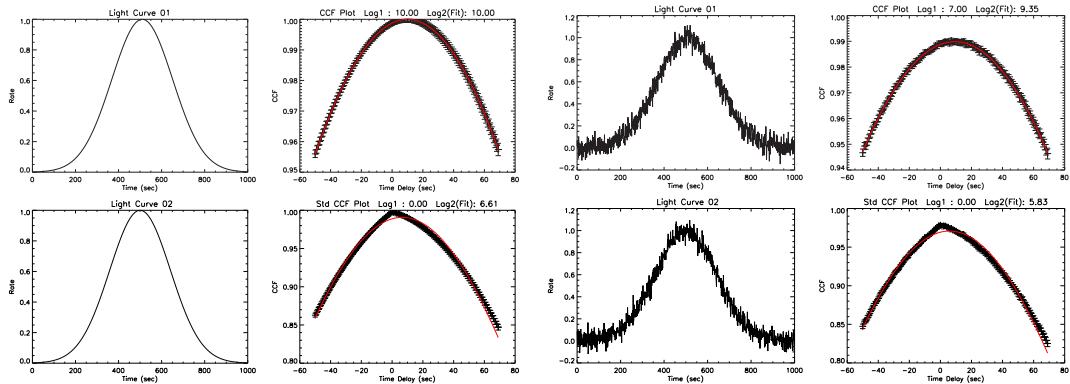
Figure C.5 Broad Gauss like light curve.
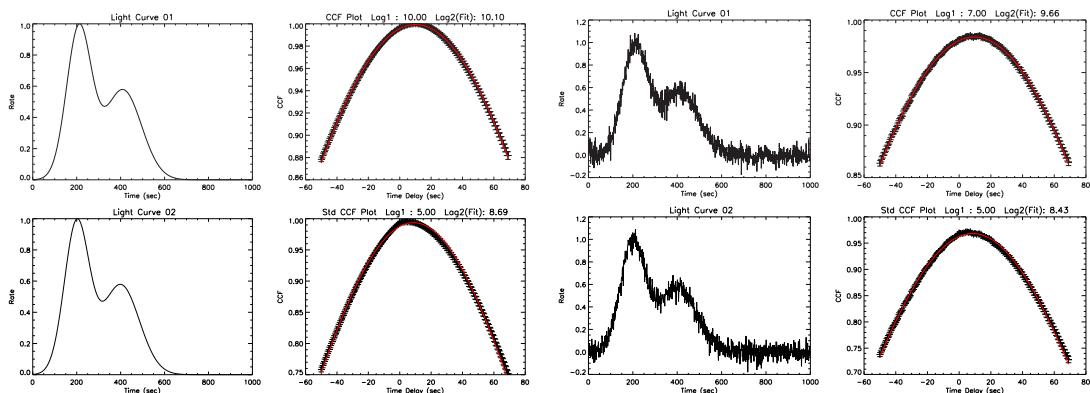
Figure C.6 Two overlapping Gauss like peaks.
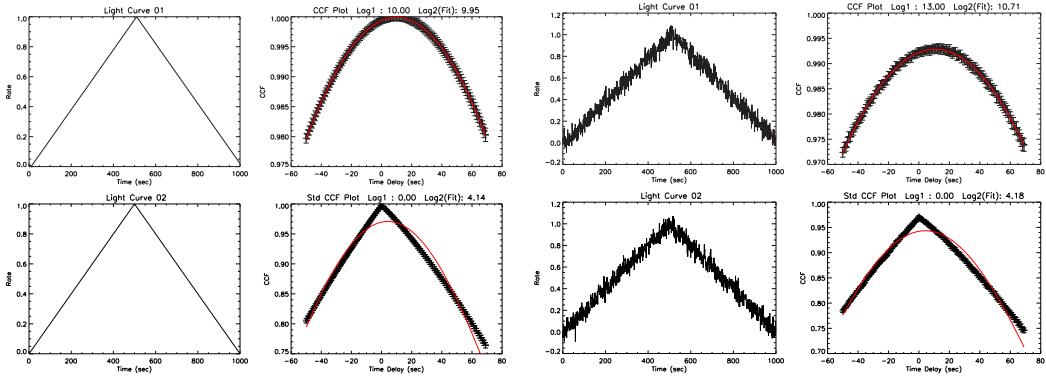
Figure C.7 Triangle shaped light curve.
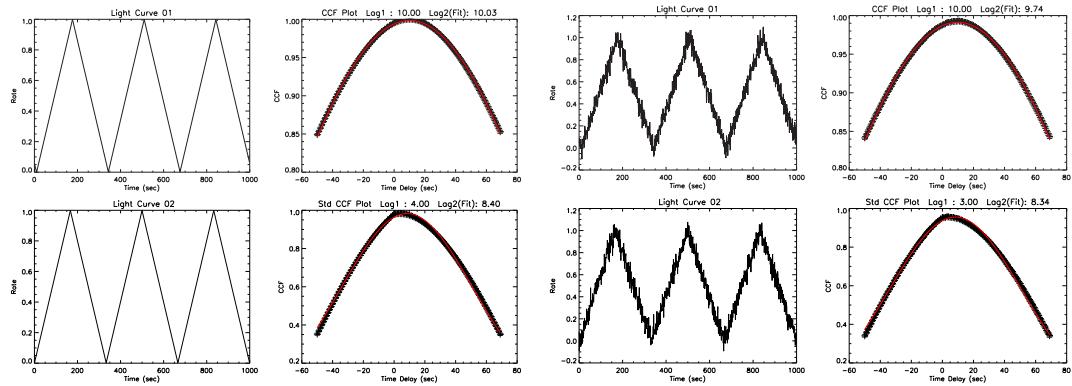
Figure C.8 Triangle shaped light curve with three peaks.
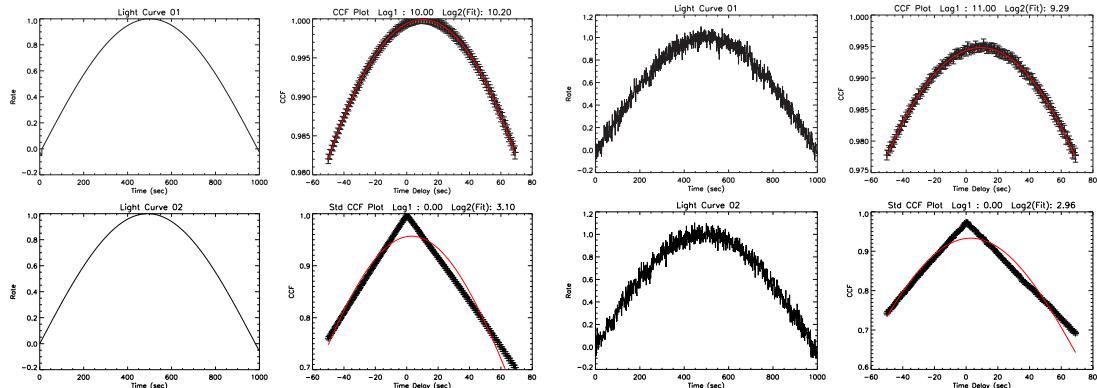

Figure C.9 Sine shaped light curve with one peak.
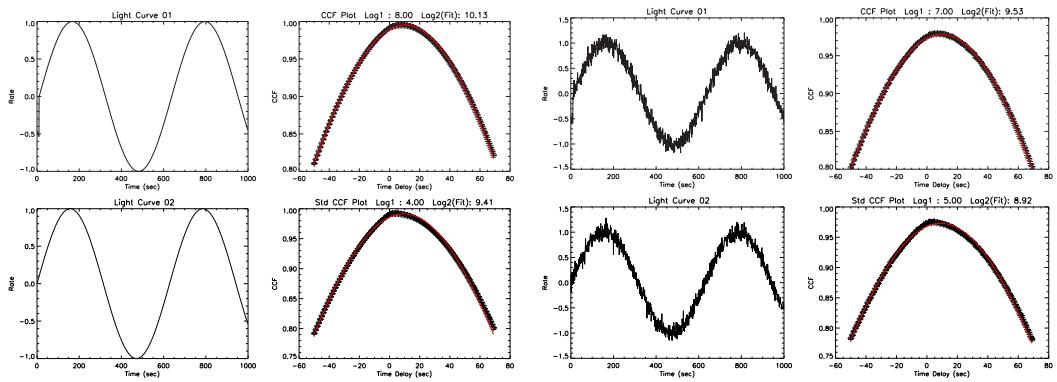
Figure C.10 Sine shaped light curve.
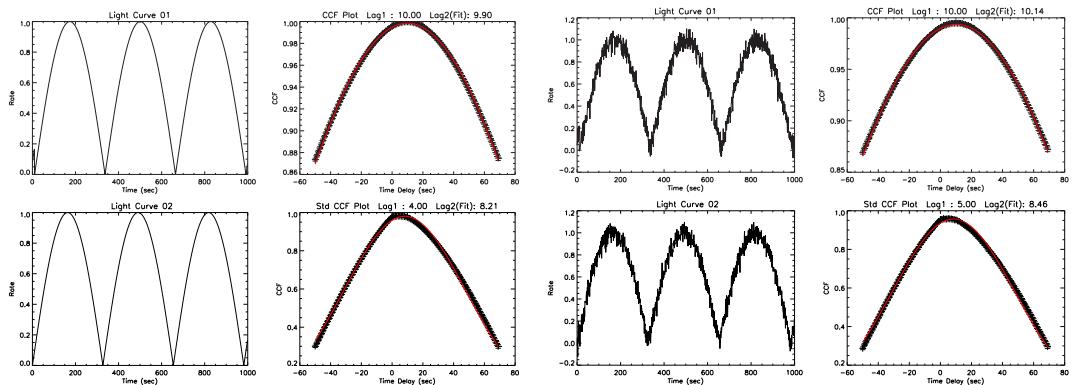
Figure C.11 Sine shaped light curve with three peaks.

Appendix D

Hurst R/S Analysis: Effects of Spikes

How do the sharp spikes in the light curve affect R/S plot in the Hurst rescaled range analysis?

During our investigation of Hurst analysis, we noticed that R/S plots that correspond to GRBs with spikes show peculiar shapes. In order to investigate the effect of spikes on the Hurst analysis we performed the following set of tests: We used three synthetic light curves with $H \sim 0.5$ (Figure D.1– D.3), $H \sim 0.1$ (Figure D.4– D.6), and $H \sim 0.9$ (Figure D.7– D.9). We then introduced large spikes at various locations in the light curve and calculated R/S plots. Before the introduction of spikes, R/S plots showed H values close to the expected H values (see left panels of Figures D.1, D.4 and D.7). However, the introduction of spikes drastically modified the shapes of R/S plots. In the case of $H \sim 0.5$ (Figure D.1– D.3), the introduction of spikes at various locations smoothed the R/S plot starting exactly at the time corresponding to the spike time. The slope of the curve after this time is 0.5. Similar behavior is observed in the cases of $H \sim 0.1$ (Figure D.4– D.6), and $H \sim 0.9$ (Figure D.7– D.9).

Based on this analysis we can make the following conclusions.

- Light curves with sharp spikes create artificially smoothed R/S plots with a slope of 0.5.

- The starting time of the smooth segment of the R/S plot is same as the spike time.

- Light curves with sharp spikes are not suitable for Hurst analysis.
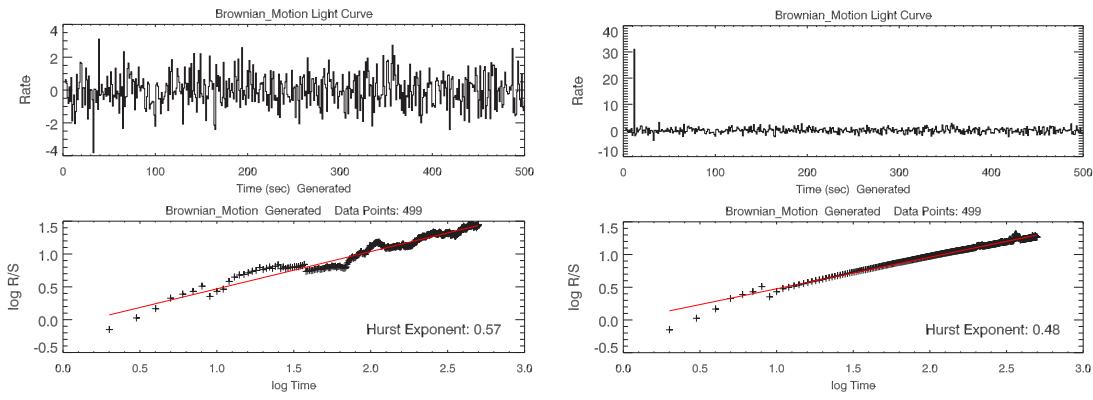
Figure D.1 Light curve with $H \sim 0.5$: No spike (left panel) and small spike at 10 sec (right panel).
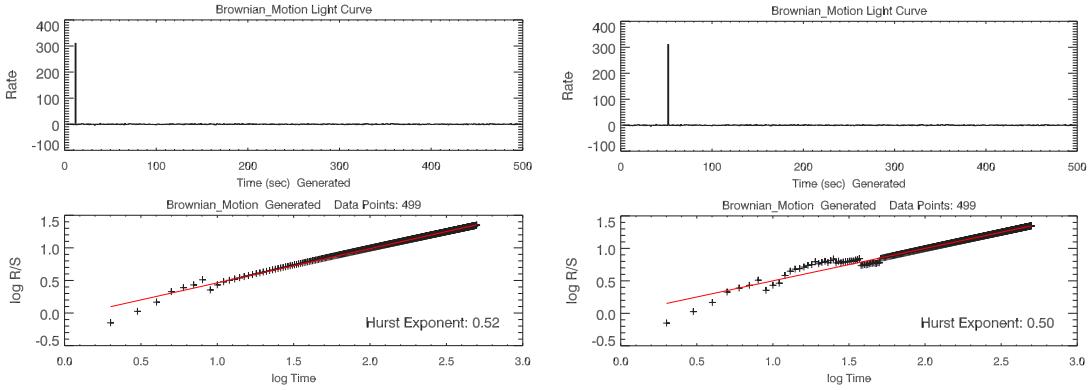
Figure D.2 Light curve with $H \sim 0.5$: spike at 10 sec (left panel) and spike at 50 sec (right panel).
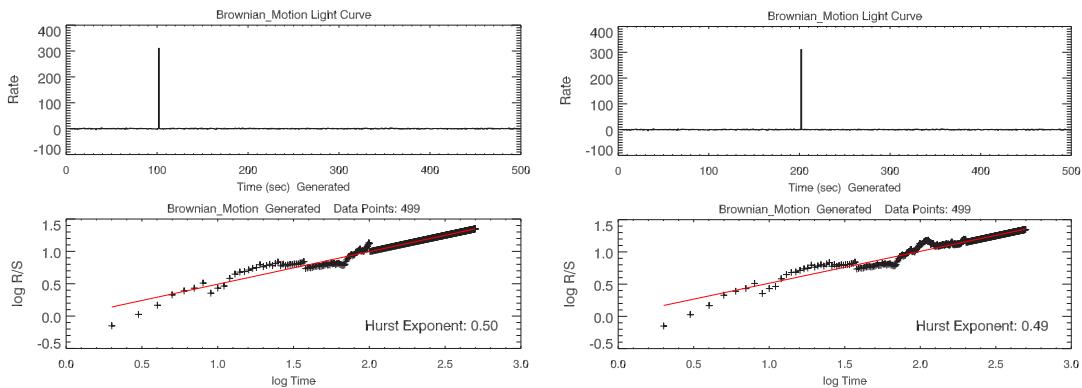
Figure D.3 Light curve with $H \sim 0.5$: spike at 100 sec (left panel) and spike at 200 sec (right panel).
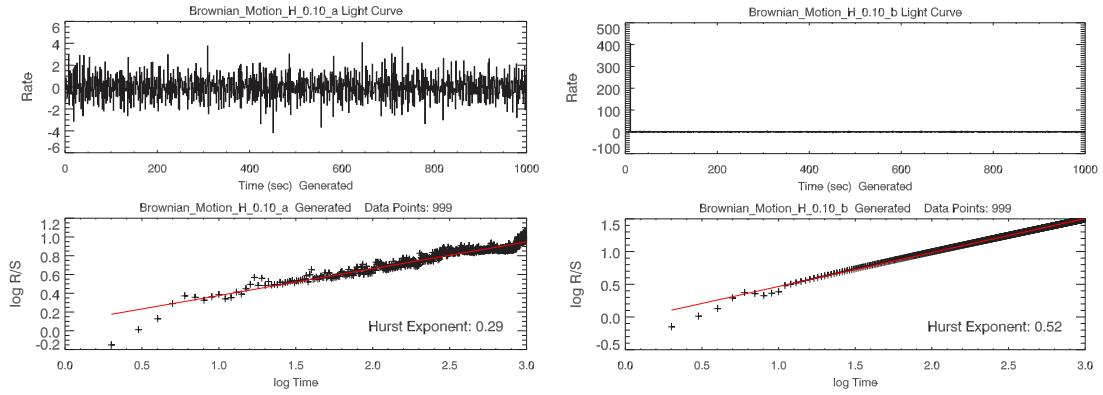
Figure D.4 Light curve with $H \sim 0.1$: No spike (left panel) and spike at 10 sec (right panel).
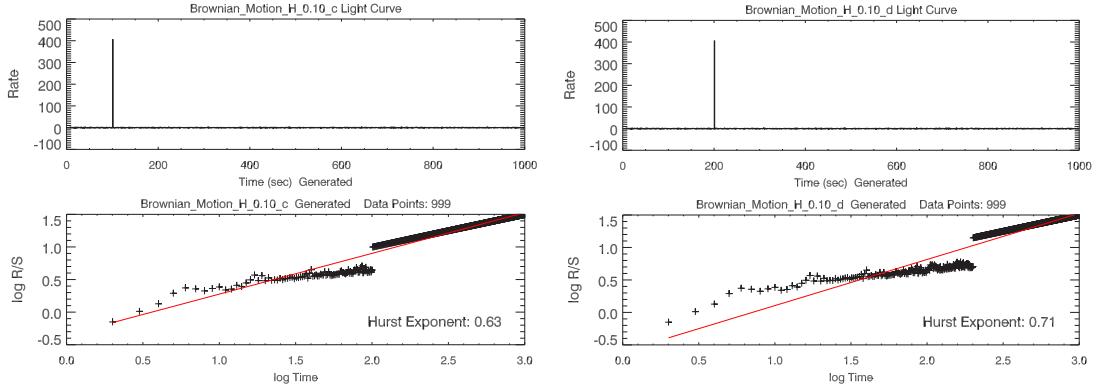
Figure D.5 Light curve with $H \sim 0.1$: spike at 100 sec (left panel) and spike at 200 sec (right panel).
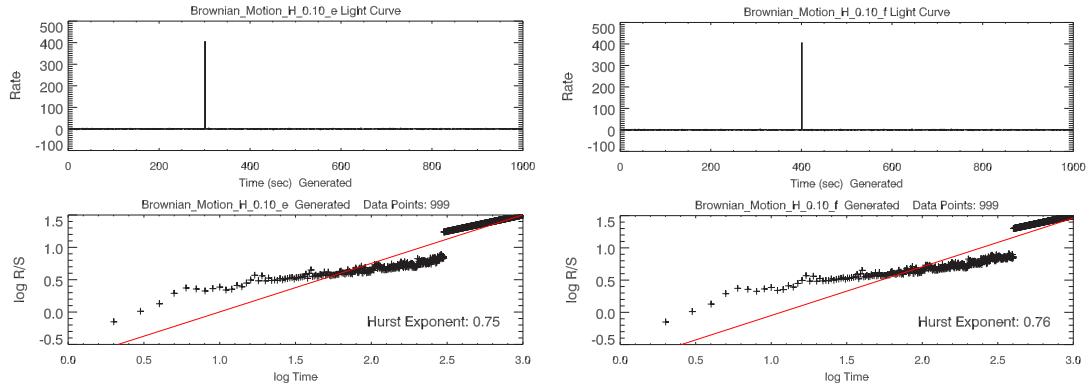
Figure D.6 Light curve with $H \sim 0.1$: spike at 300 sec (left panel) and spike at 400 sec (right panel).
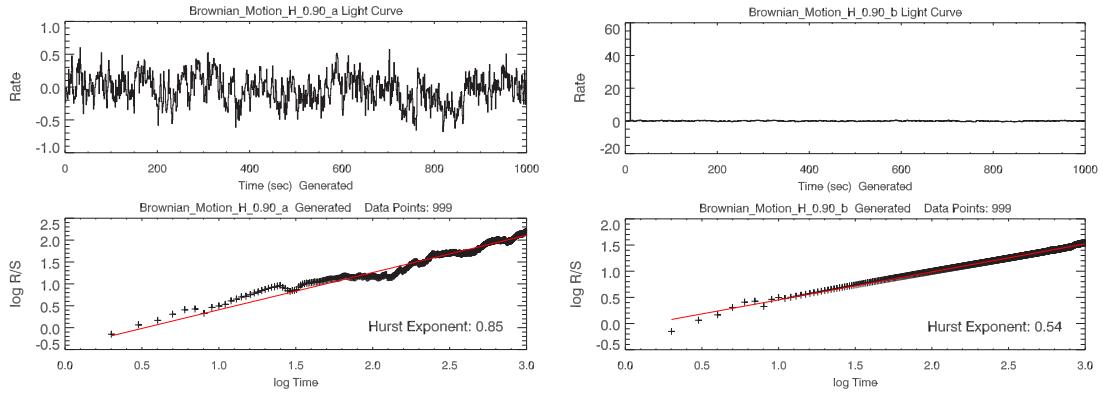
Figure D.7 Light curve with $H \sim 0.9$: No spike (left panel) and spike at 10 sec (right panel).
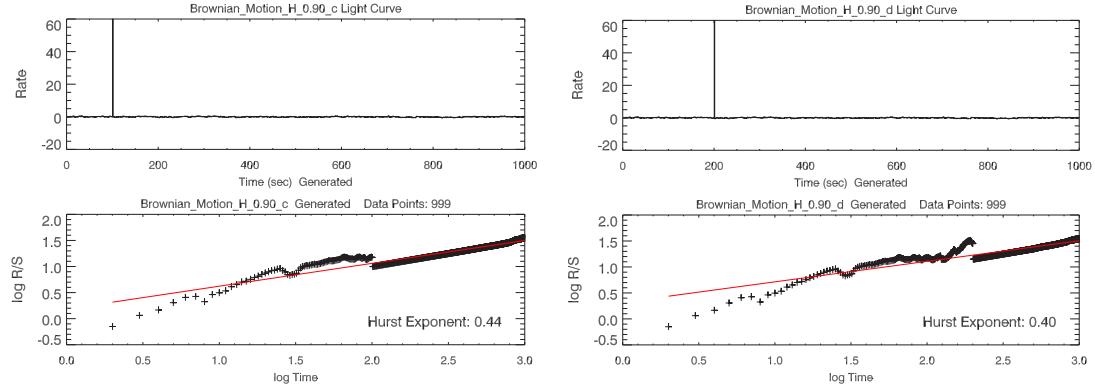
Figure D.8 Light curve with $H \sim 0.9$: spike at 100 sec (left panel) and spike at 200 sec (right panel).
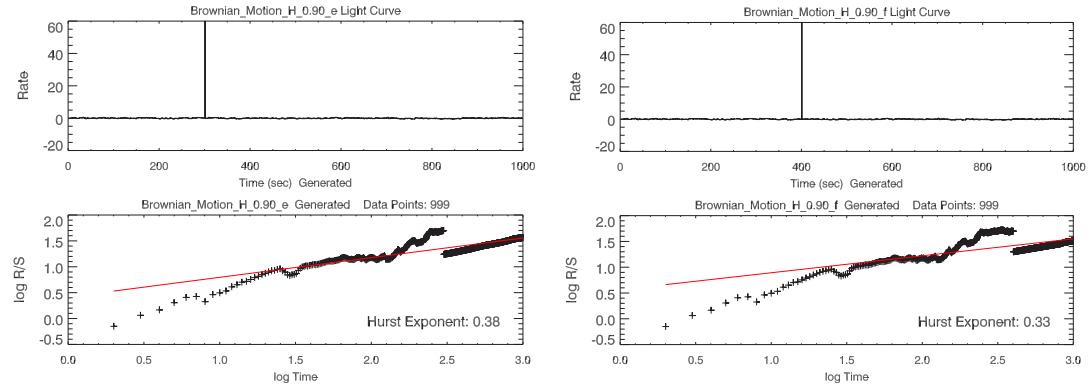
Figure D.9 Light curve with $H \sim 0.9$: spike at 300 sec (left panel) and spike at 400 sec (right panel).

154